Submitted to Reviews of Modern Physics

LBL-2352
Preprint c.2

CORIOLIS EFFECTS AND ROTATION ALIGNMENT IN NUCLEI

F. S. Stephens

January 1974

Prepared for the U. S. Atomic Energy Commission
under Contract W-7405-ENG-48

DISCLAIMER

CORIOLIS EFFECTS AND ROTATION ALIGNMENT IN NUCLEI*

F. S. Stephens

Lawrence Berkeley Laboratory
University of California
Berkeley, California 94720

January 1974

1. Introduction

Coriolis effects are not very common in our normal experience. Perhaps the most familiar object where these effects are large is the gyroscope or the "top", as the toy version is usually called. The sidewise precession of a leaning top under the influence of the downward pull of gravity is indeed a striking behavior, and one whose mystery testifies to our unfamiliarity with Coriolis effects. A less common example, but one much more analogous to the nuclear effects of interest here, is a ship's gyrocompass. In this case the tendency of a spinning gyroscope (whose axis is kept in the plane of the earth's surface) to align its axis with that of the rotating earth, is used as a navigational aid. A particle in an orbit of a rotating nucleus has a similar tendency. In the case of rotational nuclei, Coriolis effects are much more apparent than in our everyday experience, and it is the purpose of these lectures to examine what is known about such effects.

It is easy to estimate the maximum Coriolis energy of a particular particle in a rotating nucleus. For a particle orbit having angular momentum, j, in a nucleus with spin, I, and moment of inertia, $\mathcal{I}$, this energy is given by:

*Work performed under the auspices of the U. S. Atomic Energy Commission. Based on lectures given at Rudziska, Poland, August 1972, and Munich, Germany, August 1973.

$$E_{Cor}\ (max) \approx 2\,\frac{\hbar^2}{2\mathcal{J}}\,I\,j \quad . \qquad (1)$$

In rare-earth nuclei there exist orbitals with j as large as 13/2, and $\hbar^2/2\mathcal{J}$ is around 0.01 MeV. Thus when I is only 7/2, the maximum Coriolis energy is almost 0.5 MeV, or quite comparable with the energy separations between particle states in such a nucleus. This indicates that for these favorable cases the Coriolis effects can be expected to affect the nuclear structure significantly even for such low spins. Equation (1) also shows that these effects become larger with increasing spin and also with decreasing moment of inertia.

In the present paper, Coriolis effects in nuclei will be reviewed beginning with cases where they are relatively small, that is, good rotational nuclei (small $\hbar^2/2\mathcal{J}$), low-j orbitals, and relatively low spin values. An example of this type is the famous case of ^{183}W. Then some intermediate cases will be discussed; where j is large, I is moderately large, but $\hbar^2/2\mathcal{J}$ remains small (rotational nuclei). These cases are ^{235}U and the odd-mass Er nuclei. With these as background, two situations will be considered where it appears that the Coriolis effects have changed the nuclear structure in a major way. The first of these is the case where j is large, I is moderately large, and $\hbar^2/2\mathcal{J}$ becomes large; that is, in the more "vibrational" nuclei. Under the proper conditions, odd-mass nuclei of this type seem to correspond surprisingly well to a new coupling scheme characteristic of the Coriolis interaction. The other situation is that of a very large I (~20) in rotational nuclei, where these effects can be shown to provide one possible explanation for the peculiar behavior called backbending. Throughout these discussions the physical effects occurring

will be emphasized rather than the mathematical detail, although some of the latter will be essential.

It is important to keep in mind that in all cases just one physical system is treated, a particle (or two) coupled to a core that is deformed (with axial symmetry) and can rotate. In the first cases, the deformation of the core is large and the particle is strongly coupled to it; so that as the core rotates, the particle follows. The Coriolis effects are then a perturbation on the rotational spectra. In the last cases, the coupling to the deformed shape is weak and/or the rotational frequencies are large, so that the particle cannot follow the core rotation, resulting in Coriolis effects that can completely obscure the familiar type of rotational bands. It is certainly true that at some point, as the coupling decreases (β gets smaller), this rotational model will cease to apply to nuclei, but in order to find that point, the model must be understood clear down to the limit of zero coupling. Furthermore, there seems to be experimental evidence accumulating that suggests the model applies rather well at surprisingly weak couplings for at least some special states.

2. Coriolis Effects as Perturbations in Rotational Spectra

2.1. Two-band mixing in ^{183}W

A. Bohr[1] discussed Coriolis effects in his original paper on nuclear rotation in 1952, but it was some four years later before A. K. Kerman[2] applied these ideas to a specific case, namely ^{183}W. This case will be briefly reviewed, both because of its historical interest, and because it illustrates the effects in a simple case where only two bands are involved. The basic equations necessary to understand nuclear Coriolis effects are very simple. Provided a rigid, axially-symmetric deformed core is assumed, the Hamiltonian of the system can be written:

$$H = H_p + H_{rot} = H_p + \frac{\hbar^2}{2\mathcal{J}} \vec{R}^2 = H_p + \frac{\hbar^2}{2\mathcal{J}} (R_x^2 + R_y^2) \quad , \qquad (2)$$

where H_p is the Hamiltonian of the particle in the absence of rotation (a Nilsson[3] Hamiltonian for example), $\mathcal{J}$ is the moment of inertia of the core, and $\vec{R}$ is the rotational angular momentum of the core (rotation is not allowed around the symmetry axis). A coupling between the particle and the rotation comes about through the sharing of the total angular momentum between the particle and the core. This can be expressed by:

$$\vec{R} = \vec{I} - \vec{j} \quad . \qquad (3)$$

One should clearly distinguish between the particle-rotation coupling which is considered here, and the particle-core coupling which is contained in H_p. (The major part of the particle-core coupling is spherically symmetric and of no interest here; however, if the core is deformed, then there is also a coupling to the deformation, which was discussed at the end of the previous

section.) Putting Eq. (3) into Eq. (2) gives the usual expression for a rotational nucleus:

$$H = H_p + \frac{\hbar^2}{2\mathcal{J}} [I(I+1) - K^2] + H_c + \frac{\hbar^2}{2\mathcal{J}} [\langle \vec{j}^2 \rangle - \Omega^2] \quad , \tag{4}$$

where $\Omega = j_z$ and $K = I_z$ (the two are equal for an axially-symmetric core), and

$$H_c = -2 \frac{\hbar^2}{2\mathcal{J}} [I_x j_x + I_y j_y] = - \frac{\hbar^2}{2\mathcal{J}} [I_+ j_- + I_- j_+] \quad . \tag{5}$$

This term, H_c, is conventionally called the Coriolis coupling term, though it contains parts of both the Coriolis and centrifugal energies.

These are the general equations which will be used repeatedly later on, but for the present case of good roational nuclei they can be simplified. For such cases, Ω is nearly a constant for a given band, as is $\langle \vec{j}^2 \rangle$. These terms may therefore be included in H_p, giving:

$$H = H_p' + \frac{\hbar^2}{2\mathcal{J}} [I(I+1)] + H_c \quad . \tag{6}$$

The matrix elements of H_c can be written:

$$\langle I, \Omega \pm 1 | H_c | I, \Omega \rangle = - \frac{\hbar^2}{2\mathcal{J}} \sqrt{(I \mp K)(I \pm K + 1)} \langle \Omega \pm 1 | j_\pm | \Omega \rangle \quad , \tag{7}$$

where the matrix element, $\langle \Omega \pm 1 | j_\pm | \Omega \rangle$, must, in general, be calculated from the detailed (e.g. Nilsson) wave functions. For the special case where j is a good quantum number, these can be written:

$$\langle j, \Omega \pm 1 | j_\pm | j, \Omega \rangle = \sqrt{(j \mp \Omega)(j \pm \Omega + 1)} \quad . \tag{8}$$

Generally, H_c is non-diagonal, connecting bands that differ in Ω by one unit. However, as is well known, there is a diagonal contribution to bands with $\Omega = 1/2$. These rather simple basic equations will be used to treat all the cases of Coriolis coupling mentioned.

The ^{183}W case treated by Kerman involved only two bands with $\Omega = 3/2$ and $\Omega = 1/2$, and is shown in Fig. 1. The initial bandhead energies, H'_p, Kerman took as parameters, as he also did the initial $\hbar^2/2\mathcal{I}$ value for each band. In addition he took the $\Omega = 1/2$ band decoupling parameter to be adjustable. For a given value of these five parameters he could calculate the initial energies of the levels in each band. For the parameters of his final fit, these are shown in Fig. 1. Taking as a sixth parameter the value of $< \Omega = 3/2 | j_+ | \Omega = 1/2 >$, Kerman diagonalized the 2×2 matrix for each spin, giving the shifts shown in Fig. 1. As is usual, the levels repel each other; levels of a given spin moving equal distances up and down. The experimental energies are listed at the edges of Fig. 1, and it can be seen that the fit is indeed excellent. Kerman also considered some 20 M1 and E2 transition probabilities, achieving reasonable success at the expense of five additional parameters.

Subsequent work[4,5] on ^{183}W has tended to confirm the basic principles of Kerman's analysis, though some problems have arisen. Rowe[4] showed that various rotation-vibration ($\Delta K = \pm 2$) admixtures of the type found in even-even nuclei in the region of ^{183}W permitted one to obtain fits as good as Kerman's over a rather broad range of the parameters (though he obtained better fits for two particular sets of parameters). Brockmeier et al.[5] later showed that including other Nilsson states could also significantly affect the fit. To

summarize these analyses, it seems clear that there is a significant Coriolis mixing of these bands; however, the details of this mixing are probably not very well determined due to the many parameters involved, and the possibility of contributions from a number of additional effects.

There are many other cases of moderate Coriolis mixing of two or even three close-lying bands. The single-particle transfer reactions have proved to be a powerful method for such studies since they give more direct evidence on the wave functions of the observed bands. However, such detailed analyses will not be pursued further here. The purpose of discussing this case was to display the analysis of Coriolis effects in a simple case and to show that even for low $\hbar^2/2\mathcal{I}$, j and I, appreciable Coriolis effects occur. Other examples will now be considered where the effects are larger and, at the same time, the calculations are much less ambiguous.

2.2. Multiband mixing in ^{235}U

The unique-parity high-j orbitals within each major shell provide much the best cases to observe and understand large Coriolis effects in nuclei. It is essential to appreciate the reasons for this. The most obvious factor is that the Coriolis matrix elements increase approximately proportional to j for low values of Ω, as shown by Eqs. (7) and (8). For the $j_{15/2}$ orbital, which is involved in ^{235}U, this implies matrix elements around five times larger than that found by Kerman for ^{183}W. This situation is typical for all the high-j orbitals, and leads immediately to the conclusion that any study of the largest Coriolis effects will involve these orbitals. The second reason for choosing high-j orbitals is that their properties can be reliably calculated. These orbitals are well separated from any others of

the same parity, so that, to a very good approximation, j is pure. This can be verified from the Nilsson wave functions of: i) the $h_{11/2}$ orbital in the 50-82 shell, ii) the $i_{13/2}$ orbital in the 82-126 shell, and iii) the $j_{15/2}$ orbital in the shell beyond 126. This means that pure-j estimates for most of the properties of these states are nearly correct, and since the properties of these states are not much affected by the small admixtures of other j-values, they are not sensitive to the exact size of these admixtures. Yet another favorable aspect for Coriolis calculations in the component states of a high-j orbital is that these states do not Coriolis mix very much with states from other orbitals. This is both because of the pure j-value and because these other orbitals are at least one major shell removed in energy. The properties of the high-j components can be summarized as: 1) they comprise a closed set of states whose Coriolis interactions among themselves are the largest possible; 2) they have very weak Coriolis interactions with states from other j-shells; and 3) their properties can be calculated with the highest reliability of any states in deformed nuclei.

One aspect of the point about the reliability of calculated properties is illustrated in Fig. 2. Here the components of an $h_{11/2}$ orbital are shown as a function of deformation.[3] These components would be one of the closed sets of levels mentioned above. Since they all belong predominantly to the same orbital ($h_{11/2}$), their relative energies are nearly independent of the shell model parameters in the calculation, and depend only on the energy splitting of this orbital with deformation. This gives much more reliable relative energies than would otherwise be the case. The energies of the components in a particular case are read off at the appropriate deformation.

As an example, a line has been drawn on Fig. 2 at $\beta = 0.275$ to show these energies. In addition to β, the location of the Fermi surface, λ and the pairing gap, 2Δ, are needed in order to calculate these energies as they might be expected to occur in a particular nucleus. The appropriate equation for the observed energy $E(\Omega)$ in terms of the eigenvalues from Fig. 2, ε_Ω, is:

$$E(\Omega) = \sqrt{(\varepsilon_\Omega - \lambda)^2 + \Delta^2} - \Delta \quad . \tag{9}$$

There is also a UV-factor[6] to be included on the Coriolis matrix elements due to the pairing, but that is a small correction.

If a Fermi surface is chosen near the $\Omega = 7/2$ level and Eq. (9) is applied to the Nilsson eigenvalues of the $j_{15/2}$ orbitals at $\beta = 0.275$, the bandhead energies shown in Fig. 3 result. Rotational bands are then constructed on all these bandheads according to Eq. 6, where H'_p has generated the bandhead energies, $E(\Omega)$. The first few rotational levels are shown for each band in Fig. 3. The matrix elements, $< \Omega \pm 1 | j_\pm | \Omega >$, as calculated from the Nilsson wave functions are also shown on Fig. 3; and, by comparison with Eq. (8), they can all be seen to be within 10% of the pure-j values. The procedure then is to pick out from each band the state of a particular spin, I, and diagonalize the resulting matrix. For the $j_{15/2}$ shell this will be an 8×8 matrix if $I \geq 15/2$, and smaller if $I < 15/2$.

Three things should be especially noted on Fig. 3. First, a pattern much like this results from any high-j orbital. An $h_{11/2}$ orbital, for example, would have two fewer bands ($\Omega = 13/2$ and $15/2$ would be missing) and ~30% lower matrix elements, but otherwise would be very similar. The second thing to note is that Coriolis effects are much bigger for the low-Ω bands. Not only are the energy

separations of the bands smaller here, but also the matrix elements are largest. Thus, the very largest Coriolis effects will occur in low-Ω bands of high-j orbitals. Finally, the $\Omega = 1/2$ band has very anomalous spacings. Large decoupling factors always occur in these high-j orbitals, so this is a general feature. These anomalous energy spacings are transmitted to the $\Omega = 3/2$ band in the mixing process, and then on to the $\Omega = 5/2$ band in a higher order process, etc. The resulting anomalous spacings in the higher-Ω bands are a very characteristic and important feature of the mixing described here.

There are three favorable circumstances that make ^{235}U a very good case for studying such Coriolis calculations. The level scheme worked out from Coulomb excitation studies[7] several years ago is shown in Fig. 4. The first favorable feature is that many levels are observed in the $j_{15/2}$ component bands. Three band, $\Omega = 5/2$, 7/2, 9/2, are seen and there are a total of 15 rotational spacings in these bands (bandhead energies are not included in the analysis in this case). A second advantage is that anomalous spacings coming from the mixing with the $\Omega = 1/2$ band are observed in both the $\Omega = 5/2$ and 7/2 bands. This information alone tells some rather specific things about the Coriolis matrix elements. Finally, the B(E2) values between the $\Omega = 7/2$ ground band and both the $\Omega = 5/2$ and $\Omega = 9/2$ bands were determined. If one assumes that these B(E2) values result only from collective E2 transitions introduced by the mixing, then they give immediately the admixed amplitudes, and hence the Coriolis matrix elements involved. The assumption that the non-collective B(E2) values can be neglected is very likely to be essentially correct, but effects of 20% or so in the deduced mixing amplitudes cannot be excluded. Consideration of these features, and the observed E2

and M1 relative intensities, makes the ^{235}U case a good test for calculations of Coriolis effects.

The details of the calculations for ^{235}U will not be given here, but rather an indication of the kind of results obtained. Figure 5 shows the results for the rotational energies in the case where only one adjustable parameter was used. This plot is designed so that it give a straight line for a rotational band if the band follows the equation,

$$E = E_0 + A\ I(I+1) + B\ I^2(I+1)^2 \quad , \tag{10}$$

where the value of the ordinate at I = 0 would be A and the slope would be B. This plot is used because it can show the rotational energies on a sufficiently sensitive scale to see easily the anomalies in the $\Omega = 5/2$ and 7/2 bands. In the calculation all bandhead energies and matrix elements were taken from the Nilsson wave functions except the matrix elements, $< 5/2|j_-|7/2 >$ and $< 7/2|j_-|9/2 >$, which were determined from the B(E2) values as described above. The one parameter was $\hbar^2/2\mathcal{J}$, which comes into all the rotational energies (Eq. (6)) and matrix elements (Eq. (7)) except the above two. The results clearly show the correct anomaly coming from the $\Omega = 1/2$ band into the $\Omega = 5/2$ and 7/2 bands. However, the final effective $\hbar^2/2\mathcal{J}$ values for the $\Omega = 5/2$ and 9/2 bands are not correctly given.

The results of a three parameter fit are shown in Fig. 6. Here the matrix elements, $< 5/2|j_-|7/2 >$ and $< 7/2|j_-|9/2 >$, were allowed to vary from the values indicated by the B(E2) values but their ratio was held constant, and the matrix element, $< 3/2|j_-|5/2 >$, could vary. The former of these went up by 20%, and the latter went down by 20%. The fit here is excellent (note the expansion of the ordinate scale). Also the known relative M1

and E2 transition probabilities were adequately given by these wave functions. This agreement is a very strong indication that this kind of calculation is rather well understood. One puzzle emerges, whose solution is not at present understood. The matrix elements, $< 5/2|j_-|7/2 >$ and $< 7/2|j_-|9/2 >$, have values only about half as large as expected. This result comes from the measured B(E2) values almost completely unambiguously. This kind of effect on the Coriolis matrix elements near the Fermi surface is observed in essentially all other similar cases, and has been the outstanding mystery in such calculations. Resently Ring et al.[8] have shown that this discrepency does not occur if the self-consistent cranking model is used instead of the particle-plus-rotor model. The exact cause of the problem in the latter model is not yet fully understood, however.

The ^{235}U case has been discussed in some detail to show rather carefully how one treats a unique-parity j-shell, and also to illustrate that one does know how to make these calculations. In the next section cases will be considered where the effects are larger, but the data more meager.

2.3. The Odd-mass Er Isotopes

The calculated and experimental levels in three odd-mass Er isotopes[9] are shown in Fig. 7. These data are for the lowest positive-parity band in these Er nuclei, and this band is clearly composed of heavily admixed components of the $i_{13/2}$ neutron orbital. There is a reasonably normal $\Omega = 5/2$ band in ^{165}Er; a band with rather large anomalies in ^{163}Er; and, in ^{161}Er, a band with such large anomalies that some level-orders are inverted. The calculations shown in Fig. 7 were similar to those described for ^{235}U, except that no data were available on higher bands. Nevertheless, the three parameter fits shown are impressive, and leave no doubt that the spectra are basically correctly

interpreted. Figure 8 shows the rotational-energy plots like the ones discussed for ^{235}U. The plot for ^{165}Er looks much like that of ^{235}U until one appreciates the ordinate scale. These effects are much larger than those in ^{235}U, and become still larger in ^{163}Er and ^{161}Er. In the last case, the inverted levels show up as negative points on such a plot. It is not difficult to understand why these effects are large and get larger with decreasing mass number in these Er nuclei. The rotational constant, $\hbar^2/2\mathcal{I}$, which comes into the Coriolis matrix elements (Eq. (7)), is about twice as big here as in ^{235}U and is increasing with decreasing mass number.

In these Er nuclei, the Coriolis effects are producing large distortions in the rotational bands. These effects can be calculated, as has been shown, but it now seems more useful to broaden the perspective on this problem, rather than to study such fits in detail. There is no difficulty in solving Eq. (4) for any deformation (except exactly zero) and it seems essential to understand, in a general way, the nature of these solutions. If they contain some new regularities, then it is necessary to know just what these are so that they can be recognized if they occur in the Er (or other) level schemes. Along the same line, it would be interesting to understand the physical process occurring in these distorted bands. These questions will be taken up in the next section, and in Sec. 3.2, these Er nuclei will be examined again from a somewhat different viewpoint.

3. Coriolis Effects in Nuclei with Small Deformation

Whether the Coriolis effects will be large or not in a particular case depends on the relationship of the Coriolis energy, given approximately by Eq. (1), and the energy separation between interacting states, that is, the splitting between components of the j-shell of interest. This relationship can be easily estimated, provided some simple approximations are made. The first objective of the present section will be to extend the mathematical framework in order to show explicitly this relationship and some of its consequences.

3.1. Calculations in Nuclei with Small Deformation

In cases where the Coriolis effects are large, Eq. (4) must be used rather than the simplified Eq. (6). There is some problem here, as the so called "recoil term", $\hbar^2/2\mathcal{J}\ [<\vec{j}^2> - \Omega^2]$, may already be partly contained in the empirical evaluations of H_p. However, the simple limiting solutions are not reached if the recoil term is not taken explicitly into account, so that in this section, at least, the full Eq. (4) will be used. If j is a good quantum number, $< \vec{j}^2 >$ is just $j(j+1)$, and only shifts all levels by the same energy. This assumption is reasonably good for the high-j orbitals, so that the effects of including this term come mainly from the Ω^2 part (in the odd-mass case considered here).

The quantity H_p can be expressed by giving the energy of the system as a function of Ω; that is, as a function of the orientation of j to the symmetry axis of the core. Under the conditions that j is a good quantum number and that the single-particle Hamiltonian is associated with a quadrupole field oriented along the symmetry axis (the usual Nilsson[3] potential), H_p can be written:

$$H_p = e'_j + k\beta\left[\frac{3\Omega^2 - j(j+1)}{4j(j+1)}\right] = e_j + C\Omega^2 \quad , \tag{11}$$

where e_j and e'_j do not depend on Ω. The coefficient, C, determines how widely the Ω-components of the j-shell are split apart on the Nilsson diagram, and its relationship to the rotational constant, $A = \hbar^2/2\mathcal{I}$, determines much of what happens at the lower spin values. This relationship is essentially the one mentioned at the beginning of Sec. 3, and an expression for its numerical value will be given later. It can be shown (see Fig. 2) that Eq. (11) is in good agreement with the exact Nilsson solutions for the unique-parity orbitals when $|\beta| \lesssim 0.3$.

Substitution of Eq. (11) into Eq. (4) gives:

$$H = e_j + A[I(I+1) + j(j+1)] + (C-2A)\Omega^2 + H_c \quad . \tag{12}$$

For a given situation (I, j and β) the first two terms of Eq. (12) are diagonal and the solution of the particle-plus-rotor model consists of diagonalizing the last two terms. When β is large, C is large and A is small, so that H_c is small. If H_c is negligible, then the solutions are eigenfunctions of the Ω^2 term, which are clearly states with sharp Ω values, and the deformation-aligned (strong) coupling scheme is applicable. This coupling scheme is sketched in the upper part of Fig. 9, and the usual deformed wave function is also indicated. However, C and A are not functions of I, whereas H_c increases with I; so that, eventually the opposite situation must occur. That is, at sufficiently large I, the Ω^2 term will be negligible compared with H_c, and the solutions will be eigenfunctions of H_c. It has

been shown[10] that these eigenfunctions correspond to a new coupling scheme (rotation-aligned) where α, the projection of j in the direction of I (the total angular momentum of the system), is a good quantum number. The rotation-aligned wave functions, the approximate eigenfunctions of H_c, are given in the lower part of Fig. 9 and this coupling scheme is also sketched. For large I values, this rotation-aligned coupling scheme should be generally valid. When β is very small, Eq. (11) shows that H_p is nearly constant. It can be seen directly from Eq. (2) that when H_p is nearly constant (diagonal), the weak coupling scheme[11] with sharp R values will apply. The present case would correspond to a quadrupole-quadrupole particle-core interaction and core states with the rotor energies. These general regions of applicability of the three coupling schemes are clear.

However, the rotation-aligned region is extended even to low-spin states when (C - 2A), the coefficient of Ω^2, approaches zero due to the cancellation of the two terms. Since A is always positive, this occurs when C is positive; that is, for prolate deformations in the one-particle H_p given in Eq. (11). For a one-hole H_p, the sign of k in Eq. (11) is reversed and cancellation occurs for oblate deformations. Both of these conditions amount to requiring that the Fermi surface be near the low-Ω orbitals of the j-shell. If reasonable numerical estimates are made for C and A around mass 130 with j = 11/2, then the region where C = 2A occurs for $\beta \approx 0.18$. However, for a considerable region ($\Delta\beta \sim \pm 0.05$) on either side of this value, (C -2A) is small and the rotation-aligned scheme is approximately applicable. Many "vibrational" nuclei lie in this region, and much of the interest in this coupling scheme stems from the fact that some regularities in the observed levels of nuclei in this region of β correspond to those expected from the rotation-aligned scheme.

Exact solutions to Eq. (12) can be obtained by diagonalization and these will be discussed later in this section. However, simple approximate solutions can also be found for the rotation-aligned region in the case of one particle (or hole) in the j-shell, and it seems useful to discuss these first in order to have available a convenient expression for the levels , and also to give some physical insight into the process occurring.

Consider first the normal strong-coupling (adiabatic) wave function with the single-particle space limited to one j subshell, which is a satisfactory approximation for the unique-parity case considered here,

$$\psi^{Ij}_{M\Omega} = \chi^{j}_{\Omega} D^{I}_{M\Omega} \quad . \tag{13}$$

The diagonal energies of H (Eq. (12)) in this representation are:[1]

$$E(Ij\Omega) = e_j + A[I(I+1) + j(j+1) + \delta_{\Omega,1/2}(-)^{I+j}(I+\tfrac{1}{2})(j+\tfrac{1}{2})] + (C-2A)\Omega^2 \quad . \tag{14}$$

The rotation-aligned case occurs when $C \approx 2A$, so that the Ω^2 term in Eq. 12 vanishes, and the eigenfunctions of H are just those of H_c (since j is taken to be diagonal). It has been pointed out above that the approximate eigenfunctions of H_c for $I \bar{>} j$ are:

$$\psi^{Ij}_{M\alpha} = \sum_{\Omega} d^{j}_{\alpha\Omega}(\tfrac{\pi}{2})\ \chi^{j}_{\Omega} D^{I}_{M\Omega} \quad , \tag{15}$$

where the d function is the usual rotation matrix and α is the projection of j on I. The approximate eigenvalues of H_c were shown in Ref.10 to be $-2AI\alpha$,

but this can be improved by using I+1/2 rather than just I as the value of $\sqrt{I(I+1)}$. The diagonal energies of H in this representation are then approximately:

$$E_o(Ij\alpha) = e_j + A[I(I+1) + j(j+1) - 2\alpha(I+\tfrac{1}{2})] = e_j + A\,[(I-\alpha)(I-\alpha+1) + j(j+1) - \alpha^2]. \quad (16)$$

This equation should only be used when $I \geq j$, and α is restricted by the symmetry conditions so that $I - \alpha$ must be even. The general features of the spectrum can be seen from the right side of Eq. (16). For each α value, a band occurs containing every other spin value ($I-\alpha$ even) and having the core energy spacings. The highest-α bands lie lowest in energy (but α cannot exceed j), and, furthermore, the same I values are separated by higher core spacings in lower-α bands. The lowest-lying band has α=j, spins I=j, j+2, j+4, ..., and the core energy spacings; this band has been called the decoupled band. When $I \leq j$, a better approximation can be derived involving K instead of α, where K is the projection of I on j. Since H_c is symmetric in I and j, the expression for $I \leq j$ is obtained from Eq. (16) by interchanging I and j and replacing α with K. Only half the K values are allowed, since $j-K$ must be even, but every I value is allowed in a K band, and these have relative energy spacings given by AI(I+1).

It is not difficult to improve this approximation significantly. In the rotation-aligned scheme there is symmetry about the rotation axis (take this to be the x axis), so that $\langle j_y^2 \rangle \equiv \langle j_z^2 \rangle = \langle \Omega^2 \rangle$. This leads to the relation:

$$\langle \Omega^2 \rangle = \tfrac{1}{2}[j(j+1) - \alpha^2] \quad . \quad (17)$$

This value can be used in the Ω^2 term of Eq. (12) to take account of small deviations from the point of exact cancellation. Also a better approximation to the eigenvalues of H_c is:

$$H_c \psi^{Ij}_{M\alpha} \approx -2A\alpha[I(I+1) - \bar{\Omega}(\bar{\Omega}+1)]^{\frac{1}{2}} \psi^{Ij}_{M\alpha}$$

$$\approx -2A\alpha[(I+\tfrac{1}{2}) - \frac{\bar{\Omega}^2}{2(I+1/2)}] \psi^{Ij}_{M\alpha} \quad , \tag{18}$$

where $\bar{\Omega}$ is some average value of Ω for each α value. Again, the $\bar{\Omega}^2$ in Eq. (18) can be estimated using Eq. (17). Putting Eqs. (17) and (18) into Eq. (12), and rearranging terms gives:

$$E(Ij\alpha) = e_j + A\left\{(I-\alpha)(I-\alpha+1) + [\frac{C}{2A} + \frac{\alpha}{2I+1}][j(j+1)-\alpha^2]\right\} \quad . \tag{19}$$

Again, Eq. (19) applies when $I \geq j$, and $I - \alpha$ must be even. Compared with Eq. (16), the only change is that the coefficient of the $[j(j+1)-\alpha^2]$ term is no longer just the rotational constant, A. This affects mainly just the separation of the α bands When $I \leq j$, one can again interchange I and j in Eq. (19), and replace α by κ, where $j - \kappa$ is even.

For convenient evaluation, A can be related to β using the empirical connection between $B(E2;2\rightarrow0)$ and E_{2+} pointed out by Grodzins;[12]

$$E_{2+} = 6A = \frac{1225}{\mathcal{A}^{7/3}\beta^2} \text{ MeV} \quad , \tag{20}$$

where $\mathcal{A}$ is the mass number of the nucleus. This leads to the expression:

$$\frac{C}{2A} = \frac{0.379\mathcal{A}^2\beta^3}{j(j+1)} \tag{21}$$

which gives $180\beta^3$ for C/2A when $\mathcal{A} = 130$ and j = 11/2. Equation (19) is rather accurate under some circumstances, as will be shown below; however, it is not very suitable for comparison with experimental data, due to restrictions in the model. The relaxation of one of these (restriction to axial symmetry) has been studied by Meyer ter Vehn[13] who has shown that axial asymmetry reduces both the higher-spin energies in a band and the separation between bands given in Eq. (19), in accord with the the known data.[14-16] It has not yet been possible to incorporate these effects into a simple expression for the level energies.

The quality of the approximations in Eqs. (16) and (19) can be seen in Fig. 10. The solid lines there are a few of the exact solutions of Eq. (12), plotted relative to the lowest I = 11/2 solution in units of the adjacent even-even 2+ energy. Equation (16) should be valid when C = 2A, which occurs for $\beta = 0.18$ when $\mathcal{A} = 130$ and j = 11/2. The dots on Fig. 10 show the energies given by Eq. (16), plotted at the appropriate β value. The $\alpha = 11/2$ (decoupled) band is given quite accurately, but the lower α (or κ) values are not so good. The dashed lines show the diagonal energies of H (Eq. (12)) for the wave functions given by Eq. (15), and the low-spin analog,

$$\psi^{Ij}_{M\kappa} = \sum_{\Omega} d^{I}_{\kappa\Omega}(\pi/2)\ \chi^{j}_{\Omega}\ \mathcal{D}^{I}_{M\Omega} \quad . \tag{22}$$

These were evaluated numerically; however, Eq. (19) gives results within a line width or two for all the states shown, and the dependence on β given by Eq. (19) is exactly that for the dashed lines for Fig. 10. It can be seen that Eq. (19) is extremely good for $0.15 \lesssim \beta \lesssim 0.2$ and is reasonably good for $\Delta\beta = \pm 0.05$ as measured from the point where C = 2A. Neither Eq. (16) nor (19) would be very good for the lower α or κ values; however, such high-energy bands are not likely to be observed.

The region of validity of the three coupling schemes mentioned earlier can be seen in Fig. 11. Here the energy (in units of E_{2+}) of the

lowest 11/2 state in each scheme is plotted against the deformation, β, for a core with one particle in the $h_{11/2}$ j-shell. For the weak coupling scheme, H_{rot} is zero for R = 0, and it is also easy to show that H_p for this state is just e_j', which we also take to be zero. The energies for the 11/2 state in the Ω = 1/2 and 11/2 bands of the strong coupling scheme (shown as the lighter solid lines) can be obtained from Eq. (14) where e_j is given by:

$$e_j = e_j' - C\,\frac{j(j+1)}{3} = e_j' - \frac{51.5\beta}{\mathcal{A}^{1/3}} \quad . \tag{23}$$

Again e_j' is taken to be zero. Similarly the 11/2 state in the α = 1/2 and 11/2 bands are plotted as dashed lines. These were evaluated from the wave functions (Eq. (15)), but the α = 11/2 value obtained from Eqs. (19) and (23) would be indistinguishable on Fig. 11. The α = 1/2 value is not adequately given by these equations. It can be seen that for $|\beta| \lesssim 0.1$, the weak-coupled R = 0 configuration lies lowest. On the oblate side the Ω = 11/2 and α = 1/2 states cross below the R = 0 state, but Ω = 11/2 always lies well below α = 1/2, resulting in nearly normal rotational bands for $\beta < -0.1$. On the prolate side Ω = 1/2 and α = 11/2 cross below R = 0, and α = 11/2 is lowest for $0.1 \leqslant \beta \lesssim 0.3$, and thereafter Ω = 1/2 becomes lowest. The exact energies of H are shown as dots in this figure. The close correspondence of these dots with the lowest lines in Fig. 2 indicates the adequacy with which the three coupling schemes represent the exact solution of H in Eq. (4). The rotation-aligned coupling scheme is seen to have a rather broad region of applicability connecting the weak-coupling region with that of the deformation-aligned coupling scheme on the side where low-Ω orbitals occur near the Fermi surface.

The exact solutions of the particle-plus-rotor model can be obtained by diagonalizing Eq. (4) and are shown in Fig. 12 for the yrast states up to spin 23/2 coming from the $h_{11/2}$ orbital. At each β value the lowest $I = j$ state is taken to have $E = 0$, and all energies are in units of the corresponding even-even first-excited state energy (E_{2+}). In this calculation the Fermi surface was always well below the entire $h_{11/2}$ orbital, so this is a true one-particle case. Pairing was included in the BCS approximation, and Eq. (20) was used to relate A to β. The calculation in Fig. 12 is again for the mass 130 region.

The three coupling-scheme regions discussed above can be readily identified. The nearly degenerate multiplets near $\beta = 0$ are clearly those of the weak-coupling scheme, where one expects such multiplets centered on the core energies. The range where they can be identified is approximately $-0.1 \leqslant \beta \leqslant 0.1$; however, this corresponds roughly to $E_{2+} \geqslant 1$ MeV, and in such cases it is doubtful that any collective model should apply. Thus, in the present context, it is not clear that this weak-coupling scheme will be valid anywhere. The strong-coupling scheme is valid for large β values and is characterized by normal rotational bands. On the oblate side of Fig. 12, the $\Omega = 11/2$ rotational band is recognizable when β is only ~ -0.1, and is rather well developed by $\beta = -0.15$. On the prolate side the anomalous $\Omega = 1/2$ band develops quite slowly, and is not yet very pure even at $\beta = 0.3$. It has been shown above that the rotation-aligned scheme gives energies very close to the exact solutions for $0.15 \leqslant \beta \leqslant 0.2$, and is a reasonable approximation for $0.13 \leqslant \beta \leqslant 0.23$. An outstanding regularity of this coupling scheme is the occurrence of the decoupled band

(defined following Eq. (16)). The darkened lines in Fig. 12 are these states, and this band is seen to persist across the whole prolate side with very nearly the core energy spacings (identifiable at $\beta = 0$). The weak-coupling scheme gives the same energies for this band, but requires in addition that other states, $|R - j| \leq I \leq R + j$, coincide with them. Note that Fig. 12 is correct for one (or a few) particles in the $h_{11/2}$ orbital; whereas, for one (or a few) holes the particle-plus-rotor model would give exactly the same results except that the sign of β would be reversed.

The levels that would be populated following a (HI,xnγ) reaction can be predicted rather unambiguously from Fig. 12. These would be the lowest-lying high-spin states. On the prolate side this is the decoupled band, and one expects to see stretched E2 transitions and even-even core spacings. The unfavored high-spin states ($j + 1$, $j + 3$, ...) lie considerably higher in energy and will be more weakly populated, if at all. For oblate deformation a normal rotational band (j, $j + 1$, $j + 2$, ...) develops at quite low deformations, and a series of M1 + E2 cascade transitions with E2 cross-overs should be seen. At very low deformations ($\beta \sim 0.1$) the favored and unfavored yrast states lie close together, but the order of favored lowest on the prolate side and unfavored lowest on the oblate side is always preserved. For hole states (nearly full j-shell), all these predictions should occur for the opposite sign of β.

It is now of interest to look at some odd-mass nuclei in order to see if the features described above occur. Many studies have now been made of levels in odd-mass nuclei located in the "vibrational" regions ($0.1 \leq |\beta| \leq 0.25$).

Rather unambiguous decoupled bands have been seen in the Au region,[14-16] the light Gd-Yb region[17] (Sec 3.2), the La region[18,19] (Sec 3.3), and the Ru-Pd region.[20,21] The alternative rotational-bandlike levels have been seen in light Tℓ nuclei[13,22] and in the light Ce-Nd nuclei.[23] There is already some evidence that both types of band occur in lighter nuclei,[24,25] but more data are needed in these regions. It seems that a rather large amount of evidence has already been accumulated showing that the expectations outlined above do seem to occur rather often in nuclei. Some examples of these data will now be considered, beginning with the Er nuclei described in Sec. 2.3

3.2 The Light Odd-Mass Er Nuclei

There are two reasons for discussing the light odd-mass Er nuclei here. The first is that they show very clearly the transition from a strong-coupling region to a rotation-aligned region. The second is that they are involved in some of the arguments about even-even nuclei which will be made in the next section.

In Fig. 13 the energy-level spacings, in units of $\frac{\hbar^2}{2\mathcal{J}}$, are shown for a decoupled band and for a strongly-coupled rotational band based on the $i_{13/2}$ orbital. The rotational spacings shown on the left are independent of Ω except for 1/2); and also, the existence of possible lower band members is irrelevant to the present arguments. It is apparent that the decoupled band is very heavily compressed (by the Coriolis interactions), and this compression could serve as a measure of the extent of decoupling. If an average E_{2+} ($6\,\frac{\hbar^2}{2\mathcal{J}}$) is determined from the adjacent even-even nuclei, then the 17/2 - 13/2 spacing divided by this E_{2+} would be 1.0 for a decoupled band, and 5.3 for a rotational band. Comparing the 21/2 - 17/2 spacing with the

even-even 4 - 2 separation would give 1.0 and 2.9 for the two types of band. Thus an estimate can be made at any spin value of the extent of decoupling in an observed band.

A plot of this odd-A-to-average-even-even transition energy ratio is shown in Fig. 14 for the lowest band based on the $i_{13/2}$ orbital in the odd-mass Er isotopes. The decoupled-band limit for this ratio is always 1.0; whereas, the rotational band limit varies from about 5 to 2. For the 17/2 - 13/2 energy spacing, the observed rato drops monotonically from 3.6 for ^{167}Er ($\beta \sim 0.33$) to 1.0 for ^{157}Er ($\beta \sim 0.2$). This is just the trend expected; and it is caused both by the decrease in β and by a decrease in the Fermi level with mass number toward the $\Omega = 1/2$ state (the one-particle situation). The other important trend is with spin, I, and it is clear that the extent of decoupling increases with increasing I, as expected. It can be seen, however, that the higher-spin states at the lower mass numbers approach 1.1 or 1.2 rather than 1.0. The reason for this is not entirely clear, but could indicate a lower moment of inertia for the core in the odd-mass nucleus due to the blocked $i_{13/2}$ level. The $i_{13/2}$ bands in these Er nuclei show very clearly a transition to the rotation-aligned coupling scheme. Note that ^{157}Er and ^{159}Er have essentially pure decoupled bands even for the lowest-spin members (I= 13/2).

3.3. The La-Ce Region

Only one "vibrational" region will be discussed, and the La-Ce region was somewhat arbitrarily chosen. A portion of the Nilsson diagram for protons is shown in Fig. 15, where some of the orbitals have been fully drawn, and others have not. For the La nuclei, with 7 protons beyond the closed shell

at 50 (at $\beta = 0$, this closed shell is at the bottom of Fig. 3) and deformations 0.15 - 0.25 (for mass numbers 137 - 125), the $h_{11/2}$ orbital is essentially empty in all cases. Thus, the simple one-particle calculations of Fig. 12 should apply, and for prolate shapes (anticipating the results), decoupled bands should occur for all these La nuclei. Now consider the situation for the 77th and 75th neutron in ^{135}Ce, ^{137}Nd and ^{133}Ce, ^{135}Nd, respectively, where $\beta \sim 0.15$-0.20. Figure 15 can also give an estimate for neutrons in this region; the 82 closed shell comes between the $h_{9/2}$ and $s_{1/2}$ orbitals. If the nuclei are prolate, the N = 77 cases (with 5 holes in the 82 closed shell) will have one hole in the $h_{11/2}$ orbital, so that Fig. 12 should be applicable, except with the sign of β reversed. Thus, normal rotational-bandlike levels are expected, with a tendency for the levels, after the first one ($I = j$), to be paired: $j + 1$ and $j + 2$; $j + 3$ and $j + 4$; ... . For the N = 75 nuclei (7 holes in the 82 shell), the Fermi level has dropped to around the 9/2 component of the $h_{11/2}$ orbital. This gives three holes in the $h_{11/2}$ orbital and Fig. 12 does not apply. Appropriate calculations show that one expects a perturbed $\Omega = 9/2$ rotational band, where the j, $j + 2$, $j + 4$, ... levels again lie anomalously low. Thus for prolate deformation, a unique set of predictions can be made, and an equally unique and opposite set would apply - for the oblate case.

The negative-parity La levels[18,19] are shown in Fig. 16, where they are compared with the levels in the even-even Ba isotope with one fewer proton. The correspondence in energy of the odd-mass and even-even levels is remarkable, and comprises the first, and still perhaps the best, example of decoupled bands. Other features of these bands support this interpretation. The lack of population of other negative parity states argues against the weak-coupling scheme, which could otherwise explain these energies. The

spectroscopic factors for population of the $11/2^-$ state in the (α,t) and $(^3He,d)$ reactions vary from about 1.0 in ^{139}La to 0.4 in ^{131}La, in good accord with calculations[19] like those of Fig. 12. Also the dramatic drop in energy, as the mass number decreases, of the $11/2^-$ state relative to the positive parity states ($d_{5/2}$,$g_{7/2}$) in the La isotopes can be understood in this interpretation. All the known characteristics of these La levels support their assignment as decoupled $h_{11/2}$ bands.

In Fig. 17 the levels recently determined[23] for ^{135}Ce and ^{137}Nd are shown. The normal rotational-band order of the negative-parity levels is seen, but the perturbations favoring the j, j + 2, ..., levels are quite strong. This is qualitatively what is expected for a prolate shape; however, quantitatively the observed spacings are somewhat less regular than calculated. This is in the direction that might be expected if there were some shape (γ) asymmetry,[13] or softness toward such asymmetry, and the low-lying second 2+ state in the adjacent even-even nuclei show that this is very likely to be the case. Additional evidence that these nuclei are prolate comes from the large negative A_2 coefficients ($\sim$ -1.0) in the angular distributions of the M1 + E2 gamma rays in the $11/2^-$ band. This implies a negative sign for δ, the mixing ratio, and therefore a positive Q_0 (prolate), since g_K-g_R will be negative for the $h_{11/2}$ neutron and the sign of δ (and also of A_2 for an I→I-1 transition) is determined by the sign of $(g_K - g_R)/Q_0$. This rule has been discussed recently by Nakai.[26] A similar, very useful, rule can be formulated for the rotation-aligned scheme, which applies to either I→I-1 or I→I+1 transitions between the unfavored (α = j-1) and favored (α = j) bands. In this case the sign of A_2 in the mixed M1+E2 transitions should be opposite to that of the ratio, g_j-g_R/ Q_0. Such transitions have not yet been

observed in the La nuclei, but have been seen in Ir, Au, and Hg nuclei,[14-16] with angular anisotropies in accordance with this rule. The level schemes for ^{133}Ce and ^{135}Nd are shown in Fig. 18. They are also rotational-bandlike, have $9/2^-$ for the lowest spin rather than $11/2^-$, show more regular energy spacings than the previous set, and also have the large negative A_2 coefficients for the M1 + E2 transitions. All of these are in accord with expectations for a prolate shape, and show that these odd-neutron nuclei are behaving much as the particle-plus-rotor model would predict.

A question arises as to why a simple axially-symmetric particle-plus-rotor model should work so well in this La-Ce (or any other similar) region. It seems likely that many other features are involved in the core states; vibrational motion, asymmetric shapes, shape changes, sizeable individual 2-particle amplitudes, etc. Greiner[27] has pointed out that part of the answer to this question may be that so far, due to the experimental circumstances, only the yrast states (mainly just the decoupled bands) have been studied. These states are the most likely to show simple rotational features, and the lower-spin states, Greiner suggests, may be much more complex. It is therefore, of considerable interest to study other states based on the same j-shell in nuclei where decoupled bands occur. Members of the unfavored (α =j-1) band have been seen in Au, Ir, and Hg nuclei,[14-16] and also a few other lower-spin states were identified in the Au nuclei.[14] These states seem to be in general agreement with the model, but also suggest that it is important to include effects due to the asymmetric shapes in this region.[13] More data are needed on levels of this type. It would also be of interest to study the states from lower-j orbitals where additional features (especially large j-mixing) may occur.

4. Coriolis Effects in Even-Even Nuclei

There are some indications that the Coriolis effects in high-j orbitals also play an important role in the high-spin states of even-even nuclei. It is not difficult to see that this might be the case. If one considers the question of which two-quasiparticle (2qp) states of an even-even nucleus are likely to lie lowest in energy at spin 20, then the maximum Coriolis energy given by Eq. (1) becomes an important factor. If both particles are in a high-j orbital, then Eq. (1) applies, approximately, for each particle, and gives a total energy lowering of 5 MeV for $i_{13/2}$ particles. Such an energy is very significant when compared with the amounts that might be gained from other processes (pairing, shape distortion, etc.) at this spin value. While it is clear that the yrast states in even-even nuclei around spin 20 are not yet fully understood, this rough estimate, supported by detailed calculations, suggests that they could well be strongly influenced by Coriolis effects. The present section will begin with a summary of the experimental data bearing on high-spin states in even-even nuclei, and then continue with a discussion of two-particle Coriolis calculations and their application to these data.

4.1. Experimental Data from Even-Even Nuclei

Of the two types of data bearing on the question of very high-spin states in even-even nuclei, the older one has to do with the de-excitation cascade in product nuclei following heavy-ion compound-nucleus (HI,xn) reactions. This information has recently been summarized and some of its implications about the nature of such high-spin states discussed.[28] The

gamma-ray spectra from these product nuclei almost invariably consist of a set of discrete lines on a continuous background. In rotational and vibrational nuclei, the lines correspond to the transitions in the ground-state collective band (gsb),† and represent the last steps of the de-excitation. Thus the gamma-ray transitions between the highest-spin states are in the continuous background. Up to now very few direct studies of this continuum have been made, so that the information about the highest-spin states is based on observations of the transitions between lower-spin states i.e., the discrete lines. The following points, made in Ref. 28, are relevant to the present discussion: a) the maximum spin observed in the gsb ranges from around 20 for rotors to around 10 for vibrators and this maximum is characteristic of the particular nucleus (not of the reaction); b) however, when heavy ions are used to produce the compound nucleus (bringing in high angular momentum) then the gsb is fed mostly at or near the highest observed level, whereas with light projectiles, the feeding pattern is related to the distribution of angular momentum brought in by the projectile; c) the mean time interval between the reaction and population of the gsb in rotational nuclei is very short, $\lesssim$ 10 psec; and d) very high-spin isomers--I $\gtrsim$ 20 $\hbar$--have never been observed. It should be emphasized that these are features observed in (especially) rotational and vibrational nuclei, and would not apply, without modification or qualification, to closed-shell or near-closed-shell nuclei.

---

†The gsb refers to the collective band based on the ground-state configuration of a particular nucleus. For the even-even nuclei considered here, this is a completely paired configuration-- no quasiparticles--, and the levels of this band are the yrast levels at low spin values.

To understand these four points, the de-excitation was described in Ref. 28 as consisting of three cascades, whose existence had been previously proposed by Grover[29] based on numerical studies of the process. These are schematically indicated in Fig. 19. Since the initial energy (20 MeV) and level density are high, a statistical cascade (I) consisting mainly of high-energy dipole transitions is expected to occur first. This carries off around half the excitation energy but very little angular momentum and is terminated by coming into a region where the level density is no longer high. This region is located just above the yrast levels and would be $\approx$10 MeV at $I \approx 35$ for the example in Fig. 19. At this point the cascade is forced to begin carrying off angular momentum and follows, more or less closely, the yrast levels down in spin. This is called the yrast cascade (II). At some spin, the yrast levels become those of the gsb and an energy gap develops between these levels and others of the same spin. At this point the population shifts rather suddenly into the gsb through which it cascades (III) to the ground state. For lighter projectiles, where less angular momentum

is brought in, the length of the yrast cascade shortens, until it is essentially absent in reactions induced by ^{4}He.

Two interesting conclusions were drawn about this de-excitation. First, the very short feeding times and absence of isomeric states with high spin indicate that energies in the high-spin yrast region must be very smooth and the transitions between these levels must be enhanced over the single-particle value if they are E2. (Other choices for the predominant multipolarity turn out to be much more difficult to explain.) Furthermore, to avoid the generation of discrete lines in this region, the population

must be spread over several ($\gtrsim$ 5) levels. It was suggested[28] that the presence of rotational bands admixed by the strong Coriolis force present at these high spins might produce such features. Mottelson[30] has pointed out that the spectrum of an asymmetric rotor is a particularly simple one fulfilling these requirements of the yrast cascade, and models for the de-excitation based on this suggestion have recently been given.[31,32] The second conclusion was that the feeding point of the gsb was near its intersection with other levels. No other way could be found to explain the population patterns. This intersection implies a major change in the nature of the yrast levels above this spin value.

An interesting effect has recently been observed around I $\sim$ 16 in the ground-state rotational band (yrast states) of some even-even rare-earth nuclei.[33] It is called "backbending", and an illustration of what this name represents is given in Fig. 20. The main plot shows the yrast states of ^{162}Er on an energy vs. I plot, and although this looks rather ordinary, the slope has some distinct changes around I = 16. The insert shows the currently popular way to plot these data: as (essentially) the moment of inertia, $\mathcal{I}$, (defined from the transition energy) vs. the square of the rotational frequency, ω. The rotational frequency is proportional to the slope of the main curve, and it is approximated as one-half the transition energy in Fig. 20. The slope changes appear clearly on this plot, and the origin of the name, backbending, is obvious. The effect is not a very dramatic one on the main plot but, on the other hand, $\hbar\omega$ (the transition energy) is directly measured, so that the backbend is unmistakeable and quite likely indicative of some interesting phenomenon.

Many backbending nuclei are now known in the rare-earth region, and a few outside it. Several recent review articles on this subject are available.[34] In order to give an impression of the data in the rare-earth region, the known yrast levels of even-even nuclei are shown in Fig. 21 in standard $\mathcal{J}$ vs. ω^2 plots. The backbending is quite pronounced in the light Er region, and also in some of the Os nuclei. It appears to be less pronounced, if not absent, in the middle and lower-right portions of Fig. 21, .
but more data are needed to be sure of this point. This neutron-rich region is not accessible to the HI,xnγ reactions, and hence data on high-spin states are sparse.

The above discussion shows that there is good evidence for a major change in the nature of the yrast levels below I = 20 in at least some of the rare-earth nuclei; and furthermore, that at higher spin values a new very regular structure develops. Three types of explanations have been proposed for these (or parts of these) experimental results. The essential features of these explanations are 1) pairing collapse,[35] 2) rotation alignment,[36] and 3) centrifugal stretching.[37-39] It is not the purpose of the present discussion to compare these various proposals. Rather, the applicability of rotation alignment to this problem will be described; first, in terms of a general band crossing; then, more specifically for a particular rotation-aligned band; and finally, as to the expected trends in the behavior of even-even (and odd-mass) nuclei.

4.2. General Features of Band Intersection

The main features of the population patterns and level spacings described in the previous section can be explained in terms of the ground band crossing another band, with very little detail necessary as to the nature of the other band. It is useful to examine first these general properties of band intersection.

In the case where the ground band intersects another band, many features of the rotational-level spacings can be characterized in general terms.[36] Figure 22 shows the simplified situation of two bands with constant--but different--moments of inertia around their intersection point at I_c (16 in this case). The yrast states are those of the lowest band, and if there is no interaction between the bands, they simply change suddenly from one to the other at I_c. When plotted as $\mathcal{J}$ vs. ω^2, this makes a discontinuity as shown by the dashed line in Fig. 23. This discontinuity causes lower values of ω^2 above I_c if $\mathcal{J}_2/\mathcal{J}_1 > (I_c + 2)/I_c$. This might generally be the case around $I = 20$ since $(I_c + 2)I_c$ is then only ~ 1.1. As an interaction is introduced between the bands, the discontinuity is rounded, first into an S-shaped curve like A in Fig. 23, and then with increasing interaction, like B and finally C. This range covers the observed behaviors, those in the light Er (and Os) region being of the S-shaped variety (A or B in Fig. 23); whereas, the lower-Z neutron-rich rare-earth nuclei appear to be more like C. For intersecting bands, the occurrence of S-shaped curves depends on two factors: (1) the difference between the effective moments of inertia of the two bands at their intersection point, which determines the transition to be made, and (2) the strength of the interaction between the bands which determines how sharply this transition is made.

The population patterns following the (HI,xnγ) reactions in deformed nuclei can also be shown to come from rather general band intersection arguments. Consider the case where there are many quasiparticle states, each of which has a rotational band built on it. If a perturbing interaction (Coriolis force, for example) is introduced among these bands, then a matrix would have to be set up and diagonalized for each spin value, I. In Fig. 24 the lowest few solutions from this diagonalization have been indicated and labeled m = 1, 2, etc., according to the final energy. The same is done for spin I + 2, with n as the labeling index. If the perturbing interaction varies slowly with I, then the main difference between the matrices for I and I + 2 is that the initial energy of each state differs by the increased rotational energy. Thus, the main difference in the solutions will be this difference of a rotational energy, which is quite smooth with I. To higher order, if the interaction is increasing with I (the Coriolis interaction increases approximately linearly with I) then in the energy region of interest, the I + 2 states will be lowered with respect to the I states, and the mixed band will be compressed in energy over the input bands. Since the difference between the I and I + 2 matrices is small, the lowest solution with spin I will have a wave function similar to that of the lowest solution with spin I + 2, etc.

Now consider the B(E2) values between the states indicated in Fig. 24. The wave functions for a given solution, $|IM,m>$, can be written:

$$|IM,m> = \sum_K a_K^m(I)\ \phi_K\ \mathcal{D}^I_{MK} \quad , \tag{24}$$

where the $a_K^m(I)$ are the calculated amplitudes, ϕ_K signifies a particular input configuration and the $\mathcal{B}_{MK}^I$ is the usual rotational wave function. The B(E2) value between two such states can be written:

$$B(E2;I+2,n \to I,m) = \sum_{\mu M'} |< IM',m|M(E2,\mu)|I+2\ M,n>|^2 \qquad (25)$$

where $M(E2,\mu)$ is the usual E2 operator. In evaluating Eq. (25) the B(E2) values between components ϕ_K and $\phi_{K'}$ are of single particle strength or smaller unless $K = K'$, in which case they are the enhanced rotational values, $\sim \frac{5}{16\pi} Q_0^2$. Keeping only the enhanced terms gives:

$$B(E2;I+2,n \to I,m) = \frac{5}{16\pi} Q_0^2 \left[\sum_K <I+2\ K\ 20|I+2\ 2\ I\ K > a_K^m(I)\ a_K^n(I+2)\right]^2 . \qquad (26)$$

For large I the above Clebsch-Gordon coefficients are virtually independent of K, and approach the limit, $\sqrt{3/8}$. Equation (26) can then be written:

$$B(E2;\ I+2,n \to I,m> \approx \frac{3\cdot 5}{8\cdot 16\pi} Q_0^2 \left[\sum_K a_K^m(I)\ a_K^n(I+2)\right]^2 . \qquad (27)$$

The remaining summation in Eq. (27) looks like the one occurring in an orthogonality integral, which would be written:

$$\sum_K a_K^m(I)\ a_K^{m'}(I) = \delta_{m,m'} . \qquad (28)$$

Since it has been argued above that the states n look much like the states m for $n = m$, it follows from Eqs. (27) and (28) that

$$B(E2;\ I+2,n \to I,m) \approx \frac{15}{128\pi} Q_0^2\ \delta_{m,n} , \qquad (29)$$

that is, the transitions having solid lines in Fig. 24 have the full rotational strength, and those with dashed lines vanish. It is easy to see that transitions of the type $I+2,n \rightarrow I+2,n'$ also vanish, since in this approximation the Clebsch-Gordan coefficient again factors out and the sum in Eq. (19) now really is the orthogonality integral. These are precisely the selection rules needed in Sec. 4.1. to bring the population down in spin very quickly, while keeping it spread over several bands. The population then feeds rather sharply into the ground band at a critical spin value. The reason for this is that the ground band intersects the 2qp bands rather sharply near this spin value and the assumption that the matrices look nearly the same for adjacent spin values is then not valid, particularly relative to the ground band. Thus, at the point where the ground band intersects other bands, not only does the developing energy gap (with decreasing I) favor population of the ground band, but the B(E2) values for this population also peak in just this region. This seems to provide a very general explanation for rapid population of the ground band near this point, in accordance with the observations.

From the preceeding discussion it seems that the presently known features of the high-spin states of the gsb can be accounted for rather naturally in a band-intersection picture. In fact, in ^{154}Gd and ^{156}Dy, there is direct experimental evidence[40,41] that the ground band does cross another band around I = 18, producing a backbend in the yrast states. However, the fact that the upper band is populated sufficiently to be seen in these cases makes them atypical, and one cannot, therefore, be sure that this is the process occurring in the heavier backbending nuclei.

If band intersection is the general explanation of these high-spin phenomena, the intersting physics involved is in what kind of band is crossing the ground band. Within the rotation-alignment model, the answer for the light Er region is clear - a 2qp band based on $i_{13/2}$ neutrons. In the Os region this is not so clear, since other orbitals could be more important. It may be that the pairing collapse and centrifugal stretching models can also be expressed in band-intersection terms; however, that is not clear at present. The next section will take up in some detail the 2qp rotation-alignment calculations for the Er region.

4.3. Rotation Alignment in 2-quasiparticle States

The small extension of the mathematics used in the even-even case will first be discussed to give a more specific idea of what is involved. In Fig. 25 the coupling scheme is indicated, where two particles with angular momentum, j, couple to a total J, which then couples with R to give I. The projections of the two j values on the symmetry axis are labeled Ω_1 and Ω_2. Figure 26 shows the lowest few $i_{13/2}$ component levels, in a situation where λ is between the 3/2 and 5/2 components. The left side shows the main configuration of the even-even ground state, and the right side shows a 2qp state of the type under discussion. This state has K = 1, and is connected to the ground state by a large Coriolis matrix element of the type considered for the odd-mass nuclei in Secs. 2 and 3. From the lowest three levels in Fig. 26, Ω = 1/2, 3/2, and 5/2, all the 2qp states possible have been generated, giving the spectrum shown in Fig. 27. The Fermi surface was assumed to be between the Ω = 3/2 and 5/2 states in this figure. All the non-zero Coriolis matrix elements have been shown as lines between the connected states. One sees that with

only these three Ω values, a complicated pattern develops. However, this system can be diagonalized in just the previous way; and, in fact, the full $i_{13/2}$ orbital has been studied,[36] including all possible (49) 2qp states. Also, the lowest four Ω-levels have been used to construct all possible 2qp and 4qp states, and this system was also studied; so that, a reasonable idea exists of what to expect from the calculations in these even-even cases. It should perhaps be noted that Eq. (4) applies to such a system if $\vec{J}$ is substituted for $\vec{j}$, and one needs only the additional relationship:

$$\vec{J} = \vec{j}(1) + \vec{j}(2) \quad . \tag{30}$$

The reliability of these 2qp calculations is not expected to be much worse than that of the one-particle case (Secs. 2 and 3).

A general view of the energies resulting from these 2qp calculations is shown in Fig. 28 where the lowest two solutions (with the Fermi surface located as in Fig. 26) are plotted for three different β values: $\beta = 0.3$, solid line; $\beta = 0.2$, dashed lines; and $\beta = 0.1$, dotted lines. The $\beta = 0.1$ case should not be taken too seriously, since the model is not so likely to apply here, but it was included to show the trends. In all three cases, the 2qp state begins at $I = 0$ as a normal band with $K = 0$ and $E \sim 2.5$ MeV; however, it initially gains Coriolis energy so fast from mixing, that its total energy remains rather flat out to $I \approx 12$, and then (now a rotation-aligned band) goes up with about the ground-band $\hbar^2/2\mathcal{J}$ value. In all cases it crosses the ground band; however, for the $\beta = 0.3$ case, the crossing is very smooth, and not so apparent since the levels repel each other and do not get closer together than about 1 MeV. Nevertheless, plotted on an $\mathcal{J}$ vs. ω^2 plot, the ground-band line in Fig. 28 does have a typical "kink" in it (not

quite an S-shape). The earlier intersections in the $\beta = 0.2$ and 0.1 cases are caused mainly by the wider ground-band spacings which are due to the larger $\hbar^2/2\mathcal{J}$ value. (Note that in the 2qp band, the wider spacings are compensated up to $I \approx 12$ by the increased Coriolis effects.) One sees that the kink, which was not visible for $\beta = 0.3$, becomes large for $\beta = 0.2$, and even produces an $I = 12$ isomer for $\beta = 0.1$ (though this is not at all reliable). The numbers on Fig. 28 are the calculated total populations passing through each yrast state. These are obtained from the (collective) B(E2) values and energies obtained from the calculations, where equal initial population was assumed in all (50) levels at $I = 30$. The calculated populations look very much like the experimental ones, in general. The feeding in all cases comes in around the intersection point, as discussed in Sec. 4.1.

Figure 28 shows that an intersection of the gsb with a rotational-aligned 2qp state based on $i_{13/2}$ particles can, in general, explain the observed features in the light Er region. To compare in more detail with specific nuclei is not so easy, since there are potentially many parameters entering such calculations. At this point it is useful to remember that most of the parameters entering into the 2-quasiparticle calculation for even nuclei also enter in much the same way into the 1-quasiparticle calculation of the lowest $i_{13/2}$ band in an odd nucleus. Such bands are observed throughout the rare earth region and it seems clear that backbending in the even nuclei should be related to the characteristics of these bands in the adjacent odd nuclei if the rotation-alignment model is correct. A one-to-one relationship, however, should not be expected since other factors, particularly the ground-band energy spacings and the pairing gap, also influence the backbending.

A comparison of odd-mass and even-even Coriolis effects is shown in Fig. 29, where fits to the lowest $i_{13/2}$ band in ^{161}Er and ^{171}Hf were made, and then the identical parameters were used in calculations[42] for the adjacent ^{162}Er and ^{172}Hf. There were no adjustable parameters for these even-even calculations, though some quantities that are not relevant for the odd-mass nuclei do enter. The agreement in Fig. 29 seems excellent, and suggests that calculations of this type might be able to account for some of the details of the backbending in even-even nuclei. More general calculations,[43,44] including these rotation-alignment effects as well as pairing and deformation changes have recently been made, and seem to bear out this rotation-alignment explanation of backbending in the Er region.

4.4. Backbending in Odd-mass Nuclei

It has been pointed out that decoupled bands have energy spacings identical to those in the adjacent even-even nuclei, and that the bands based on $i_{13/2}$ states in the odd-mass nuclei of the light Er region tend to be decoupled. It would seem to follow that these bands in the odd-mass nuclei should backbend like their even-even neighbors. However, the situation is more complicated if the decoupled odd particle is also one that is involved in the 2qp rotation-aligned state in the even-even nucleus. The recent studies of such effects seem to shed considerable light on the cause of the backbending, and a brief account of this work[45] will be given.

An explanation for the backbending in even-even nuclei is illustrated by the solid lines in Fig. 30. The ground-state band, labeled as the paired vacuum state $|\tilde{0}>$, is shown to be crossed by another band. The band indicated here is the 2qp rotation-aligned one, where the first quasiparticle has the maximum angular-momentum projection on the rotation axis, $\alpha = j = 13/2$, and the second quasiparticle has the maximum remaining projection on that axis, $\alpha = j - 1$. This is written in the usual second-quantization notation as $\alpha^{\dagger}_{13/2}\alpha^{\dagger}_{11/2}|\tilde{0}>$, where $\alpha^{\dagger}$ is a creation operator for quasiparticles and the subscript refers to the rotation-aligned quantum number called (somewhat unfortunately in this context) α. Adding an odd particle to each of these states (dashed lines) raises both of them by the energy, Δ, due to pairing effects; but this can be ignored since only the relative energy (crossing point) is of interest. The one-quasiparticle state then coincides in energy with the paired vacuum state as shown in Fig. 30. However, the same rotation-aligned two-quasiparticle state involved in the even-even case cannot be made in the odd-mass case due to the Pauli

principle. The odd neutron is already occupying the $\alpha = 13/2$ state. The most favorable states available to the broken pair are then $\alpha = 11/2$ and $\alpha = 9/2$; so that, the three-quasiparticle state becomes: $\alpha^{\dagger}_{13/2}\alpha^{\dagger}_{11/2}\alpha^{\dagger}_{9/2}|\tilde{0}>$. The energy difference between the one- and three-quasiparticle state is larger than that between the zero- and two-quasiparticle states because (1) the $\alpha = 9/2$ state is less favorable energetically than is the $\alpha = 13/2$ state, and (2) the additional angular momentum gained by breaking the pair is only 10 $\hbar$ rather than 12 $\hbar$, so that 2 $\hbar$ more of core rotational angular momentum is required. The sum of these two effects can be estimated to be about 1 MeV, so that the intersection should come at <u>higher</u> spin and rotational frequency as shown in Fig. 30. Thus, backbending in such a nucleus would only occur at higher spin values, if at all. Note that if the decoupled odd particle in this example were an $h_{11/2}$ proton instead of an $i_{13/2}$ neutron, the above interference would not occur, and the decoupled $h_{11/2}$ band would be expected to backbend like its even-even neighbors.

The above situation is of particular interest since it seems likely that the odd-mass nuclei would behave differently according to other backbending models. The prediction of the pairing-collapse model about backbending in a decoupled $i_{13/2}$ band can be stated very simply. An odd particle reduces the pairing correlations due to blocking effects, and thus the pairing might be expected to collapse at a lower rotational frequency. This statement can be illustrated in Fig. 31. The solid lines again show the even-even situation based on this model: the paired vacuum state intersecting the unpaired vacuum state. The dashed lines show the odd-mass situation. For the unpaired case, the one particle state, $\alpha^{\dagger}_{13/2}|0>$, and the even-even vacuum state, $|0>$, coincide as shown, provided:

1) the vacuum is assumed to be the average of the two nuclei adjacent to the odd-mass nucleus; 2) the decoupled $i_{13/2}$ state lies exactly at the Fermi surface, and 3) the level density is reasonably large. However, in the paired case, the one-quasiparticle state always occurs higher in energy than the vacuum state by the odd-even mass difference, Δ. The dashed line in Fig. 31 for the odd-mass band with pairing is, therefore, raised in energy by this amount - taken to be 0.8 MeV. As a result, the intersection with the unpaired band is seen to occur at lower spin and also at lower rotational frequency (earlier). Note that the size of the backbend could be smaller in this case, due to the reduced pairing; but, nevertheless, the moment of inertia should reach its upper limit (unpaired value) earlier.

The experimental evidence on backbending in the odd-mass nuclei in the light Er region is rather clear. In the odd-neutron nuclei, the decoupled $i_{13/2}$ bands do not backbend like their even-even neighbors; whereas, the odd-proton $h_{11/2}$ bands do. The evidence[45] on ^{157,159}Er compared with ^{156,158,160}Er is shown in Figs. 32 and 33, where the spacings in the odd-mass decoupled band are treated exactly like those in the even-even gsb. It is apparent that the odd-mass bands neither backbend nor approach the $2\mathcal{J}/\hbar^2$ value of the even-even nuclei after their backbend. On the other hand, ^{157,159,161}Ho are shown in Fig. 34 to backbend much like their even-even neighbors. At low spin values, the Ho points are below the even-even ones because these $h_{11/2}$ bands are not completely decoupled (The lowest point or two for ^{159}Er also shows this.). This means that the $\mathcal{J}$ values obtained do not represent core values, but it cannot change the conclusion about backbending, which comes directly from the

transition energies. These data on odd-mass nuclei support the rotation-alignment interpretation of backbending in the light Er region, and also suggest a general means to determine where this model is applicable, and which particles are involved. This could be useful in the Os region, for example, where it is not clear if rotation alignment is involved, and if so, whether $i_{13/2}$ neutrons or $h_{9/2}$ protons are mainly responsible for the backbending.

5. Conclusion

Coriolis effects in nuclei have been traced from the point where they are small perturbations in good rotational spectra, to the point where they apparently dominate the low-energy spectrum. The situation for a particular case depends on the relationship of the rotational energy to the energy coupling the particle to the non-spherical part of the potential. If the latter energy is much larger, good rotational spectra exist, whereas if it vanishes, the system is spherically symmetric leading to a spectrum with no energy splitting of the multiplets formed by coupling a particle to a core state. With the assumptions and simplifications made in Secs. 2 and 3, it is easy to make calculations anywhere between these limits. Adjacent to each limit, one finds regions where a perturbation treatment could apply. This would be a particle-core weak coupling model near the spherical limit, and a Coriolis perturbation approach near the good rotational region. If the Fermi surface is near high-Ω levels, these two perturbation regions merge into each other, and one changes rather suddenly from a spherical region into one of reasonably good rotors. But if the Fermi surface is near low-Ω states, then there is a broad region where neither of these schemes is very good. Due to a cancellation of terms in this region, the solutions are approximately eigenfunctions of the Coriolis operator and these correspond to a third coupling scheme where the particle angular momentum has sharp values, α, along the rotation axis. Such a rotation-aligned coupling scheme has been discussed and seems to describe rather well the yrast states in many odd-mass nuclei. This coupling scheme might also apply to non-yrast states, and it is at present a challenge to see how far the model can be extended in this direction.

In the even-even nuclei, the rotation-aligned scheme may also play an important role. It has been suggested that backbending in the light rare-earth region may be just the intersection of the ground band with such a rotation-aligned two-quasiparticle state composed of $i_{13/2}$ neutrons. The observed backbending in odd-mass nuclei, suggests that this explanation is correct in the light Er region. Whether this will prove to be the case in other regions is not yet clear.

ACKNOWLEDGEMENT

I am indebted to many people for discussions on the various topics covered in this paper. In particular, I would like to thank Dr. R. M. Diamond for his contributions to essentially all aspects of it. I apologize to the people in this field whose work has not been adequately covered. This paper has evolved from lectures reflecting my own interests and knowledge of the subject, and is not an attempt at the more difficult task of presenting a reasonably complete and unbiased review of the subject.

REFERENCES

1. A. Bohr, Dan. Mat. Fys. Medd. 26, no. 14 (1952).

2. A. K. Kerman, Dan. Mat. Fys. Medd. 30, no. 15 (1956).

3. S. G. Nilsson, Dan. Mat. Fys. Medd. 29, no. 16 (1955).

4. D. J. Rowe, Nucl. Phys. 61, 1 (1965).

5. R. T. Brockmeier, S. Wahlborn, E. J. Seppi, and F. Boehm, Nucl. Phys. 63, 102 (1965).

6. A. Bohr and B. R. Mottelson, Nuclear Structure, Benjamin, New York, New York, Vol. 1 (1969), Vols. 2 and 3, to be published.

7. F. S. Stephens, M. D. Holtz, R. M. Diamond, and J. O. Newton, Nucl. Phys. A115, 129 (1968).

8. P. Ring, H. J. Mang, and B. Banerjee, preprint 1974.

9. S. A. Hjorth, H. Ryde, K. A. Hagemann, G. Løvhøiden, and J. C. Waddington, Nucl. Phys. A144, 513 (1970).

10. F. S. Stephens, R. M. Diamond, and S. G. Nilsson, Phys. Letters 44B, 429 (1973).

11. A. de-Shalit, Phys. Rev. 122, 1530 (1961).

12. L. Grodzins, Phys. Letters 2, 88 (1962).

13. J. Meyer ter Vehn, private communication (1973).

14. F. S. Stephens, R. M. Diamond, D. Benson, Jr., and M. R. Maier, Phys. Rev. C7, 2163 (1973); P. O. Tjøm, M. R. Maier, D. Benson, Jr., R. M. Diamond, and F. S. Stephens, to be published.

15. S. Andre, J. Boutet, J. Jastrzebski, J. Lukasiak, J. Rivier, C. Sebille-Schuck, Z. Sujkowski, J. Treherne, Proceedings of the International Conference on Nuclear Physics, Munich, 1973, Ed. J. de Boer and H. J. Mang, Vol. I, p. 196.

16. D. Proetel, D. Benson, Jr., M. R. Maier, R. M. Diamond, and F. S. Stephens, to be published.

17. P. Kleinheinz, R. Sheline, M. R. Maier, R. M. Diamond, and F. S. Stephens, Phys. Rev. Letters 32, 68 (1974).

18. F. S. Stephens, R. M. Diamond, J. R. Leigh, T. Kammuri, and K. Nakai, Phys. Rev. Letters 29, 438 (1972).

19. P. Kleinheinz, S. M. Harris, G. Løvhøiden, and K. Nakai, BAPS 17, 898 (1972); K. Nakai, P. Kleinheinz, J. R. Leigh, K. H. Maier, F. S. Stephens, and R. M. Diamond, Phys. Letters 44B, 443 (1973).

20. C. M. Lederer, J. M. Jaklevic, and J. M. Hollander, Nucl. Phys. A169, 489 (1971).

21. P. C. Simms, F. A. Rickey, and J. R. Tesmer, Phys. Rev. Letters 30, 710 (1973).

22. J. O. Newton, S. D. Cirilov, F. S. Stephens, and R. M. Diamond, Nucl. Phys. A148, 593 (1970).

23. J. Gizon, A. Gizon, M. R. Maier, R. M. Diamond, and F. S. Stephens, submitted to Nucl. Phys. (1973).

24. P. G. Bizzeti, A. M. Bizzeti-Sona, M. Bucciolini, R. Huber, W. Kutchera, H. Morinaga, R. A. Ricci, and C. Signorini, Proceedings of the International Conference on Nuclear Physics, Munich (1973) ed. J. de Boer and H. J. Mang, Vol. I, p. 173.

25. C. Protop, K.-O. Zell, H.-G. Friederichs, B. Heits, and P. V. Brentano, ibid., p. 216.

26. K. Nakai, Phys. Letters, 34B, 269 (1971).

27. W. Greiner, private communication (1972).

28. J. O. Newton, F. S. Stephens, R. M. Diamond, W. H. Kelley, and D. Ward, Nucl. Phys. A141, 361 (1970).

29. J. R. Grover, Phys. Rev. 157, 832 (1967); J. R. Grover and J. Gilat, Phys. Rev. 157, 862 (1967); ibid., 814; ibid., 823.

30. B. R. Mottelson, The Nuclear Structure Symposium of the Thousand Lakes, Joutsa, Finland, August 1970; Fifth Nordic-Dutch Accelerator Symposium, Ebeltoft, Denmark, May 1971.

31. K. Sugawara-Tanabe and K. Tanabe, Nucl. Phys. A208, 317 (1973).

32. J. Meyer ter Vehn, preprint, 1974.

33. A. Johnson, H. Ryde, and J. Sztarkier, Phys. Letters 34B, 605 (1971).

34. A. Johnson and Z. Szymanski, Physics Reports 7C, 181 (1973); R. A. Sorensen, Rev. Mod. Phys. 45, 353 (1973); K. Kumar, Physica Scripta 6, 270 (1970).

35. B. R. Mottelson and J. G. Valatin, Phys. Rev. Letters 5, 511 (1960).

36. F. S. Stephens and R. S. Simon A183, 257 (1972).

37. P. Thieburger, preprint (1972); Phys. Letters 45B, 417 (1973).

38. Y. P. Varshni and S. Bose, Phys. Rev. C 6, 1770 (1972).

39. C. K. Ross and Y. Nogami, Nucl. Phys. A211, 145 (1973).

40. T. L. Khoo, F. M. Bernthal, J. S. Boyno, and R. A. Warner, Phys. Rev. Letters 31, 1146 (1973).

41. H. R. Andrews, D. Ward, R. L. Graham, and J. S. Geiger, preprint (1973).

42. F. S. Stephens, P. Kleinheinz, R. K. Sheline, and R. S. Simon, submitted to Nucl. Phys. (1973).

43. J. Krumlinde and Z. Szymanski, Phys. Letters 36B, 157 (1971); Proceedings of the International Conference on Nuclear Physics, Munich (1973), ed. J. de Boer and H. J. Mang, p. 200.

44. B. Banerjee, H. R. Dalafi, P. Ring, and H. J. Mang, Proceedings of the International Conference on Nuclear Physics, Munich (1973), ed. J. de Boer and H. J. Mang, p. 198; B. Banerjee, H. J. Mang, and P. Ring, Nucl. Phys. A215, 366 (1973).

45. E. Grosse, F. S. Stephens, and R. M. Diamond, Phys. Rev. Letters 31, 840 (1973); 32, 74 (1974).

FIGURE CAPTIONS

Fig. 1. The ^{183}W rotational bands as treated by Kerman.

Fig. 2. The solid lines are the Nilsson solutions for the $h_{11/2}$ orbital as a function of deformation. The dashed lines are the energies given by Eq. (11). The vertical line marks $\beta = +0.275$, and its intersections with the Nilsson lines represent the relative energies of the various component levels at that deformation.

Fig. 3. The $j_{15/2}$ bands in ^{235}U (as calculated from Eqs. (6) and (9)) prior to the Coriolis diagonalization. The matrix elements of the operator $j_{\pm}$ as calculated from the Nilsson wave functions are also shown. Only a few rotational levels of each band are indicated.

Fig. 4. Levels Coulomb excited in ^{235}U.

Fig. 5. Rotational spacings of bands in ^{235}U. The points are the experimental data, with the height of a point covering the error limits, and the lines correspond to the spacings obtained from the one-parameter Coriolis calculation.

Fig. 6. This plot is like Fig. 5, except (1) the lines correspond to the three-parameter Coriolis calculation, and (2) the ordinate scale has been doubled.

Fig. 7. The experimental and calculated positive-parity levels in $^{161,163,165}Er$ according to Ref. 9.

Fig. 8. Rotational spacings of the positive-parity band in the three Er nuclei. Some other bands in these nuclei have been plotted on this figure, which is also taken from Ref. 9.

Fig. 9. Schematic vector diagrams illustrating the strong-coupling scheme (above) and the rotation-aligned coupling scheme (below). The $\hat{3}$ axis is the nuclear symmetry axis, and the vertical axis is taken to be the rotation axis, located in the $\hat{1}$, $\hat{2}$ plane

Fig. 10. The exact solutions to Eq. (12) (solid lines) are compared with the diagonal energies for the wave functions given by Eqs. (15) and (22) (dashed lines). Equation (19) gives results essentially identical to the dashed lines. The ordinate is the difference in energy between the state having spin I and the lowest I = 11/2 state for the respective type of solution, in units of the even-even $I = 2^+$ energy. The exact solutions shown are for a one-particle case (the Fermi surface is always below the entire j-shell), pure j = 11/2 wave functions, and no pairing correlations; however, the results are not very sensitive to any of these conditions. The dots show the energies as given by Eq. (16) at the appropriate β value.

Fig. 11. The energy of the lowest I = 11/2 state (in units of the even-even $I = 2^+$ energy) is shown for three different coupling schemes (lines) and for the exact diagonalization of Eq. (12) (dots). The conditions are the same as those for Fig. 10. The inserts show schematically vector model schemes for the lowest-lying configurations, where the $\hat{I}$-axis is taken to be the rotation axis, and the multiple-pronged arrows indicate mixtures of states.

Fig. 12. The results of diagonalizing Eq. (12) for the $h_{11/2}$ orbital at various β values showing all the yrast states up to I = 23/2 (the second-lowest I = 11/2 state is also shown). The ordinate is the difference between the eigenvalue and that of the lowest I = 11/2 state, in units of E_{2+}. The Fermi surface, λ, is below the entire $h_{11/2}$ orbital for all the β values shown.

Fig. 13. Level spacings, in units of $\hbar^2/2\mathcal{J}$, for an $i_{13/2}$ particle in a normal rotational band (left) and in a decoupled band (right).

Fig. 14. The ratio of $\Delta E(I + 2 \rightarrow I)$ in an odd-mass nucleus divided by the average of the corresponding transition energies in the adjacent even-even nuclei $\Delta E(I + 2 - j \rightarrow I - j)$, is plotted against mass number for the light Er nuclei. The rotational-band and decoupled-band limits are shown, together with the data for the first four such transitions in the lowest-energy $i_{13/2}$ band.

Fig. 15. A portion of the Nilsson diagram for protons, where only the high-j orbitals have been fully drawn. At $\beta = 0$, the 50 closed shell is at the bottom of the figure, and the 82 shell comes between the $s_{1/2}$ and $h_{9/2}$ orbitals.

Fig. 16. A comparison of the negative parity bands in the odd-mass La isotopes with the ground band in the neighboring Ba nuclei. In most cases (energy zero in parentheses) the La $11/2^-$ level is not the ground state and its energy has been subtracted from all levels shown for that isotope.

Fig. 17. Energy levels in ^{135}Ce and ^{137}Nd. The transitions in the $11/2^-$ bands are shown as solid; whereas, the others are open. The width of the arrows indicates the amount of population following the (HI,xnγ) reaction.

Fig. 18. Energy levels in ^{133}Ce and ^{135}Nd. The transitions in the $9/2^-$ bands are shown as solid; whereas, the others are open.

Fig. 19. Excitation energy is plotted against angular momentum in a nucleus (with mass around 160) that is the product of an (^{40}Ar,4n) reaction. The populated energy and angular momentum range is shown, together with the proposed cascade pathway to the ground state.

Fig. 20. A plot of energy vs. I for the ground-band rotational levels in ^{162}Er. The insert shows the same data in the type of plot generally used to show backbending behavior.

Fig. 21. Ground-band level energies in even-even rare-earth nuclei. The plots give the moment-of-inertia $\mathcal{J}$ versus the square of the rotational frequency ω^2, both quantities derived from the transition energy. In a few cases where more than one possible choice exists, the lowest-energy transition is always used. Tentatively assigned band members are indicated by an omitted dot. The compression factors C and the contour line for C = 0.45 are

derived from the $17/2^+ \rightarrow 13/2^+$ level spacings in the lowest $i_{13/2}$ band observed in the odd-N nuclei, and from mean value $\bar{E}(2\rightarrow 0)$ of the 2+ energies in the adjacent even nuclei. The value of C varies from 1.0 to 0.18 as the band changes from rotational to decoupled. This plot is taken from Ref. 42.

Fig. 22. The solid lines show the energies of two rotational bands as a function of I. The bands have different moments of inertia ($\hbar^2/2\,\mathcal{J}_1$ = 15 keV, $\hbar^2/2\,\mathcal{J}_2$ = 10 keV) and are arranged to intersect at I = 16. The dotted and dashed lines show the energies of the mixed bands resulting from cases B and C, respectively, in Fig. 23.

Fig. 23. The ratio $\mathcal{J}/\mathcal{J}_2$ is plotted vs. ω^2 for the two bands in Fig. 22. The horizontal lines connected by a dashed line correspond to no mixing between the bands, C corresponds to interband matrix elements comparable to the maximum gsb-2qp ones used in the Coriolis calculations of Ref. 36, B to matrix elements three times smaller, and A to ones ten times smaller.

Fig. 24. A schematic illustration of the lowest three solutions for spins I and I + 2, with some of the interconnecting E2 transitions indicated.

Fig. 25. The coupling scheme discussed in the text. It should not be inferred from this sketch that all these quantities have sharp values simultaneously.

Fig. 26. Placement of particles in the states based on the $i_{13/2}$ orbital in an even-even nucleus with a Fermi surface, λ. The left side of the figure represents the most probable situation for the ground state, whereas the right side shows a low-lying 2-quasiparticle state. Many levels from other orbitals would be intermixed with these, but for simplicity are not shown.

Fig. 27. The ten states possible considering only 2qp states in the Ω = 1/2, 3/2, and 5/2 components of the $i_{13/2}$ orbital plus the ground state (0qp). The interconnecting lines show the locations of non-zero Coriolis matrix elements.

Fig. 28. The lowest two solutions of the even-even case for β = 0.3 (solid lines), β = 0.2 (dashed lines), and β = 0.1 (dotted lines). The numbers represent the total population passing through each level.

Fig. 29. A comparison of experimental (dots) and calculated (lines) properties of levels in the pairs of nuclei ^{161,162}Er and ^{171,172}Hf. The left side of the figure shows the fits obtained for the lowest $i_{13/2}$ band in the odd nucleus of each pair, and the right side shows the results for the even-even nucleus calculated using the same parameters.

Fig. 30. This plot shows the intersection points, based on the rotation-alignment model, of the ground band with the broken-pair excited band in: 1) an even-even nucleus (solid lines) and 2) an odd-mass nucleus with a decoupled $i_{13/2}$ odd particle (dashed lines). The subscripts on the quasi-particle creation operators ($\alpha^\dagger$) refer to the rotation-alignment quantum number, α.

Fig. 31. This plot shows the intersection points, based on the pairing-collapse model, of the ground band with the unpaired excited band in: 1) an even-even nucleus (solid lines) and 2) an odd-mass nucleus with a decoupled $i_{13/2}$ odd particle (dashed lines). Note that the subscript on the creation operators ($\alpha^\dagger$ or $a^\dagger$) refers to the rotation-alignment quantum number, α.

Fig. 32. Conventional backbending plots for ^{156,158}Er, and for the decoupled band in ^{157}Er. The following expressions have been used: $2\mathcal{J}/\hbar^2 = (4I'-2)/(E_I-E_{I-2})$ and $\hbar\omega = (E_I-E_{I-2})/2$, where I' = I for the even-even nuclei and I' = I - j for the decoupled band in the odd-mass nucleus.

Fig. 33. Conventional backbending plots for ^{158,160}Er and for the decoupled band in ^{159}Er. See caption to Fig. 32.

Fig. 34. A comparison of backbending in ^{157,159,161}Ho with their even-even neighbors. The even-even curves are the usual ones of this type, and the odd-A bands are treated as described in Fig. 32.

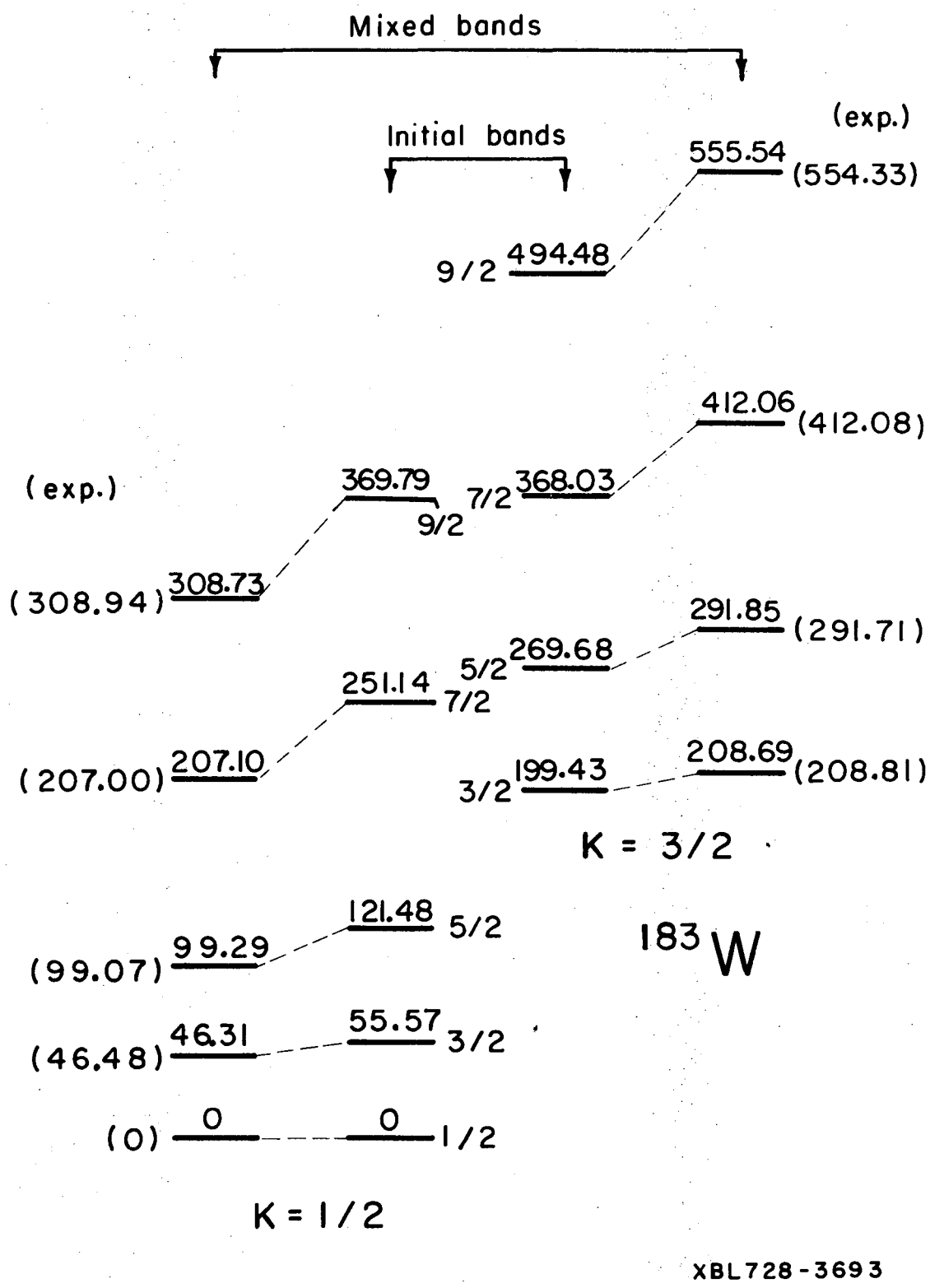
Mixed bands
Initial bands
(exp.)
555.54
(554.33)
9/2
494.48
412.06
(412.08)
(exp.)
369.79
9/2
7/2
368.03
(308.94)
308.73
291.85
(291.71)
269.68
5/2
251.14
7/2
(207.00)
207.10
3/2
199.43
208.69
(208.81)
K = 3/2
121.48
5/2
183 W
(99.07)
99.29
(46.48)
46.31
55.57
3/2
(0)
0
0
1/2
K = 1/2
XBL728-3693

Fig. 1

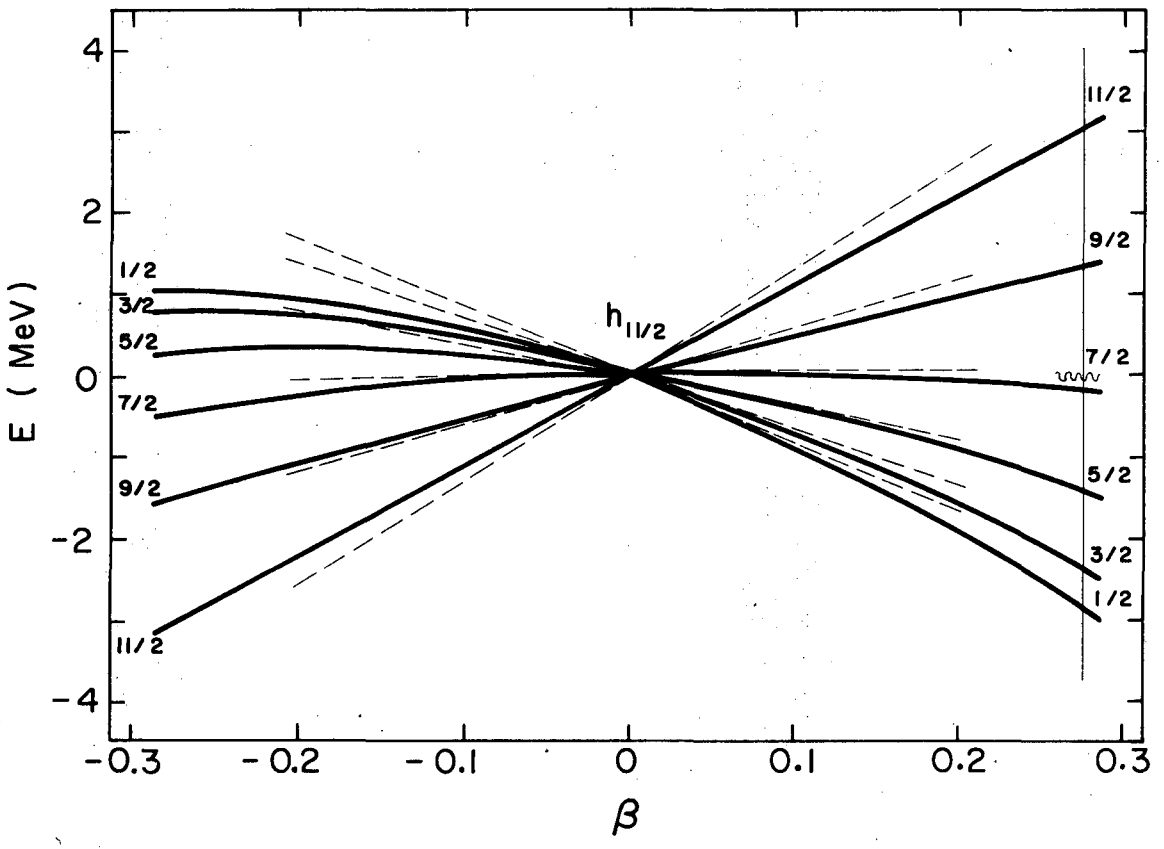
4
2
0
-2
-4
E (MeV)
-0.3
-0.2
-0.1
0
0.1
0.2
0.3
β
h11/2
1/2
3/2
5/2
7/2
9/2
11/2
11/2
9/2
7/2
5/2
3/2
1/2
XBL728-3692

Fig. 2

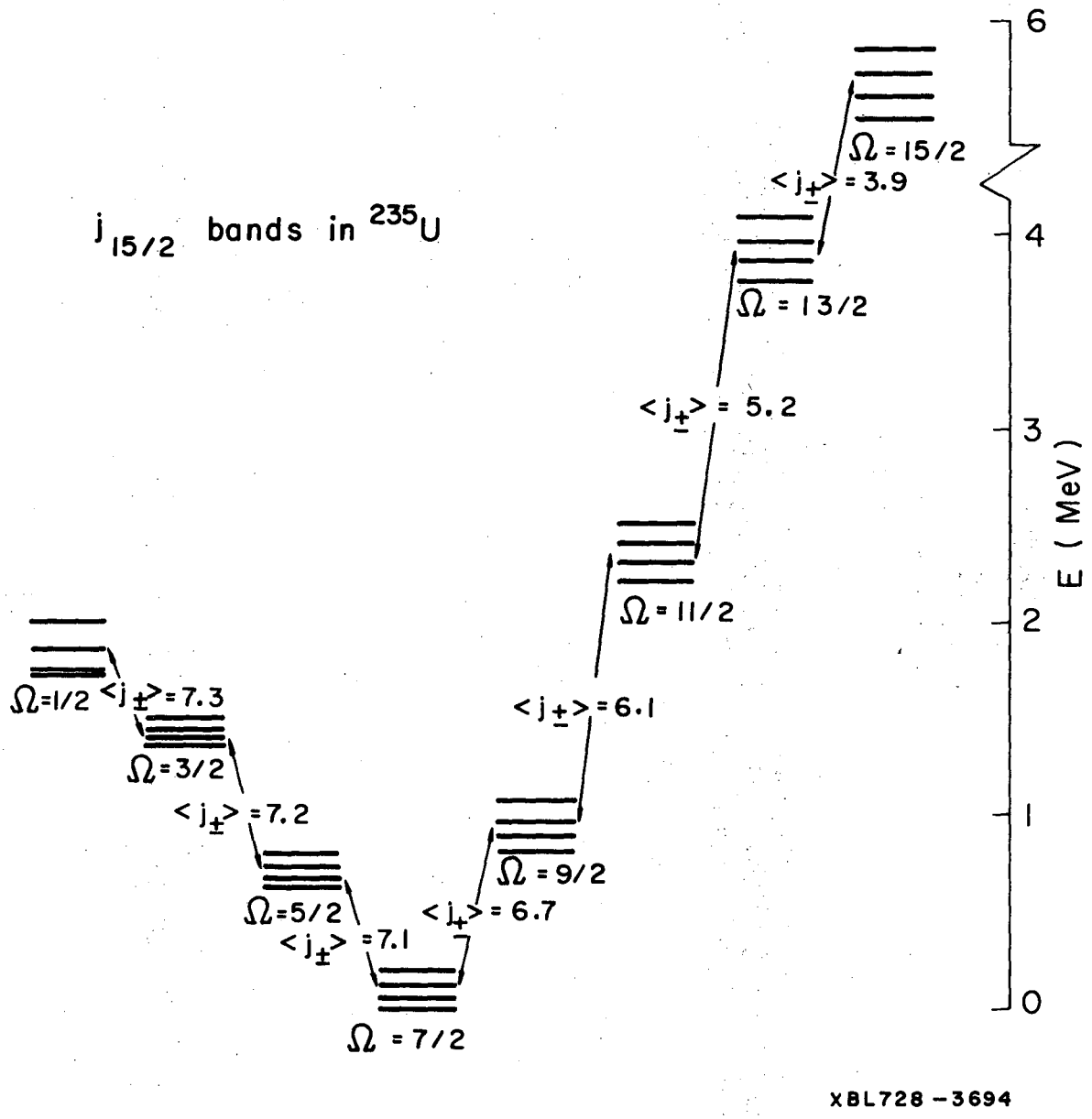
$j_{15/2}$ bands in ^{235}U
Ω=1/2
<j±>=7.3
Ω=3/2
<j±>=7.2
Ω=5/2
<j±>=7.1
Ω=7/2
<j±>=6.7
Ω=9/2
<j±>=6.1
Ω=11/2
<j±>=5.2
Ω=13/2
<j±>=3.9
Ω=15/2
E (MeV)
0
1
2
3
4
6
XBL728-3694

Fig. 3

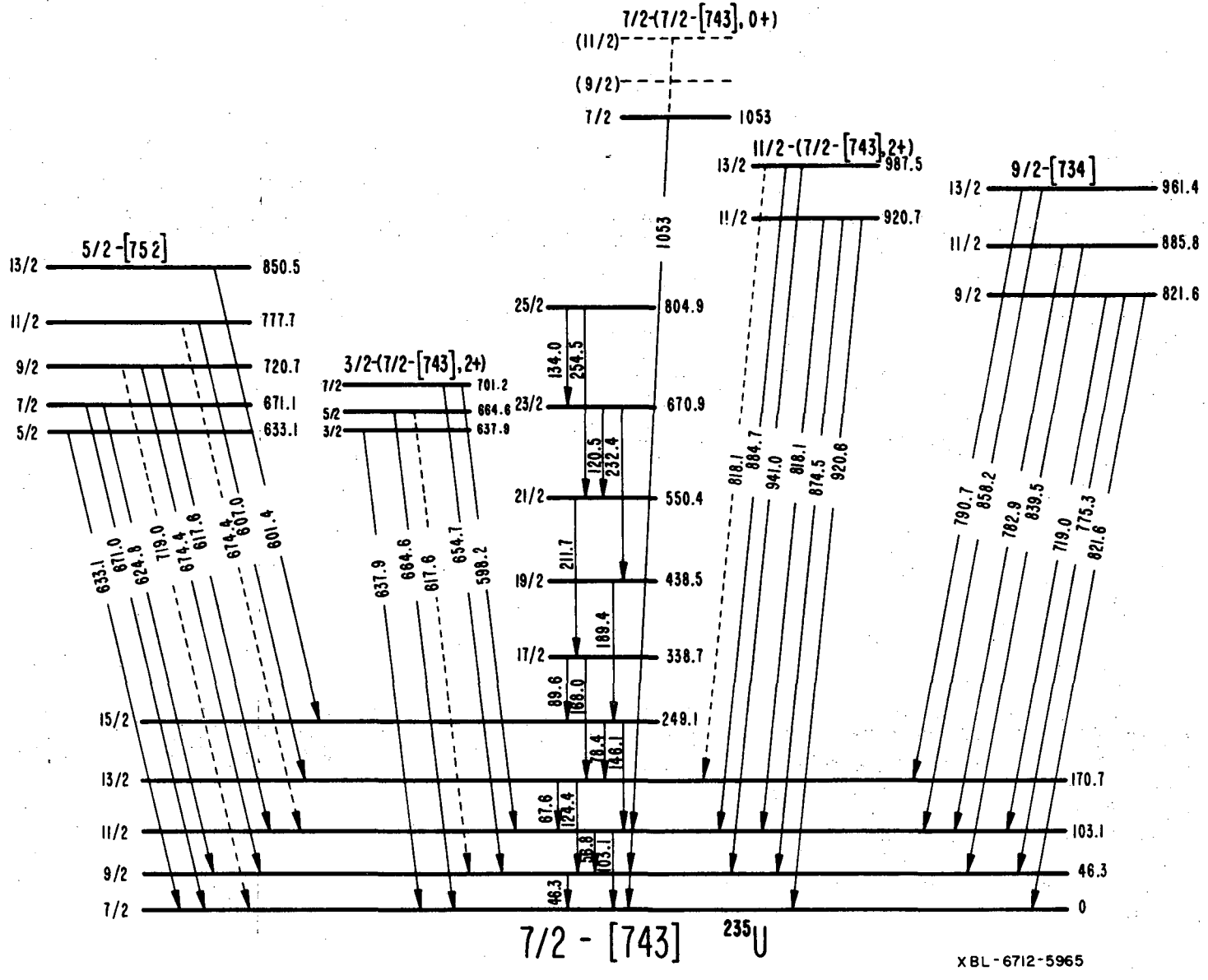
7/2-(7/2-[743], 0+)
(11/2)
(9/2)
7/2
1053
11/2-(7/2-[743], 2+)
13/2
987.5
11/2
920.7
9/2-[734]
13/2
961.4
11/2
885.8
9/2
821.6
5/2-[752]
13/2
850.5
11/2
777.7
9/2
720.7
7/2
671.1
5/2
633.1
3/2-(7/2-[743], 2+)
7/2
701.2
5/2
664.6
3/2
637.9
1053
25/2
804.9
23/2
670.9
21/2
550.4
19/2
438.5
17/2
338.7
15/2
249.1
13/2
170.7
11/2
103.1
9/2
46.3
7/2
0
134.0
254.5
120.5
232.4
211.7
189.4
89.6
168.0
78.4
146.1
67.6
124.4
36.8
103.1
46.3
633.1
671.0
624.8
719.0
674.4
617.6
674.4
601.0
601.4
637.9
684.6
617.6
654.1
598.2
818.1
884.7
941.0
818.1
874.5
920.6
790.7
858.2
782.9
839.5
719.0
775.3
821.6
7/2 - [743] 235U
XBL-6712-5965

Fig. 4

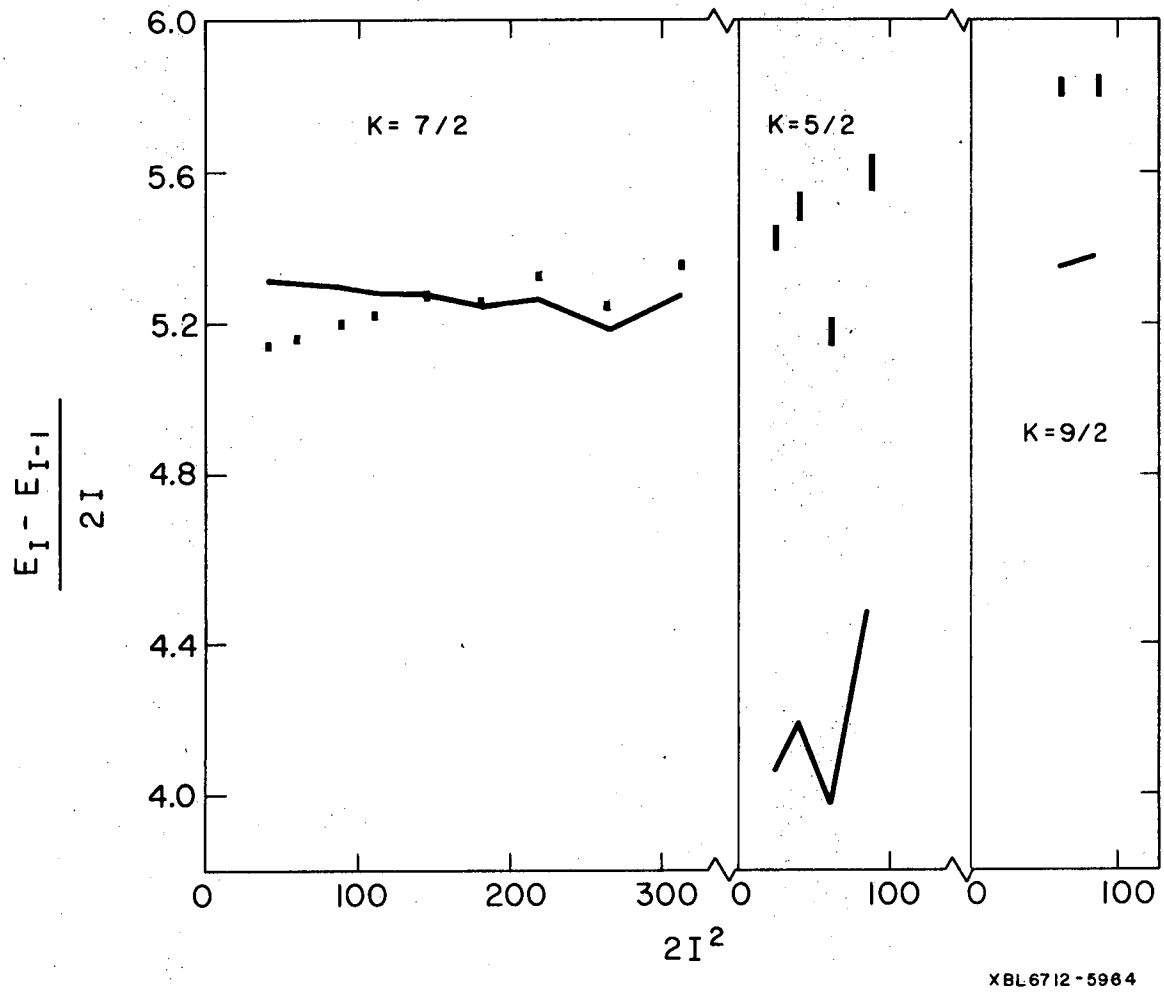
6.0
5.6
5.2
4.8
4.4
4.0
K= 7/2
K=5/2
K=9/2
0
100
200
300
0
100
0
100
$2I^2$
$\frac{E_I - E_{I-1}}{2I}$
XBL6712-5964

Fig. 5

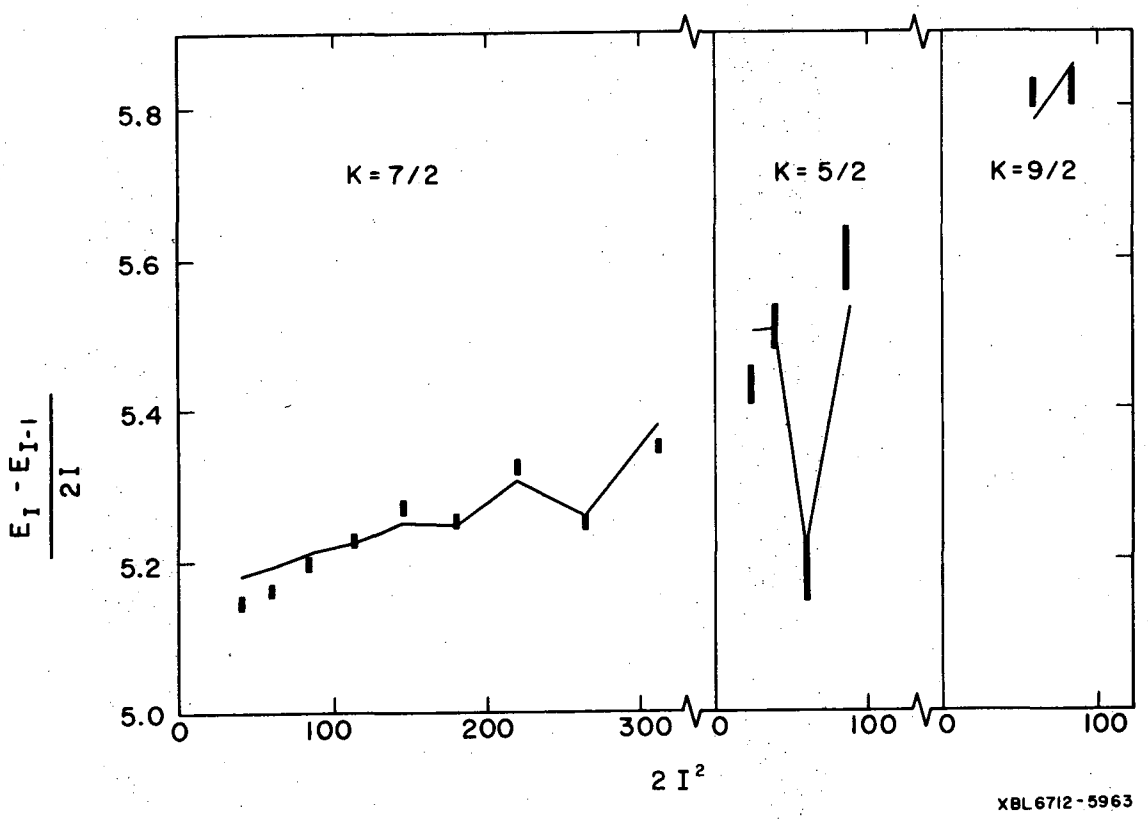
K = 7/2
K = 5/2
K = 9/2
5.8
5.6
5.4
5.2
5.0
0
100
200
300
0
100
0
100
$\frac{E_I - E_{I-1}}{2I}$
$2I^2$
XBL6712-5963

Fig. 6

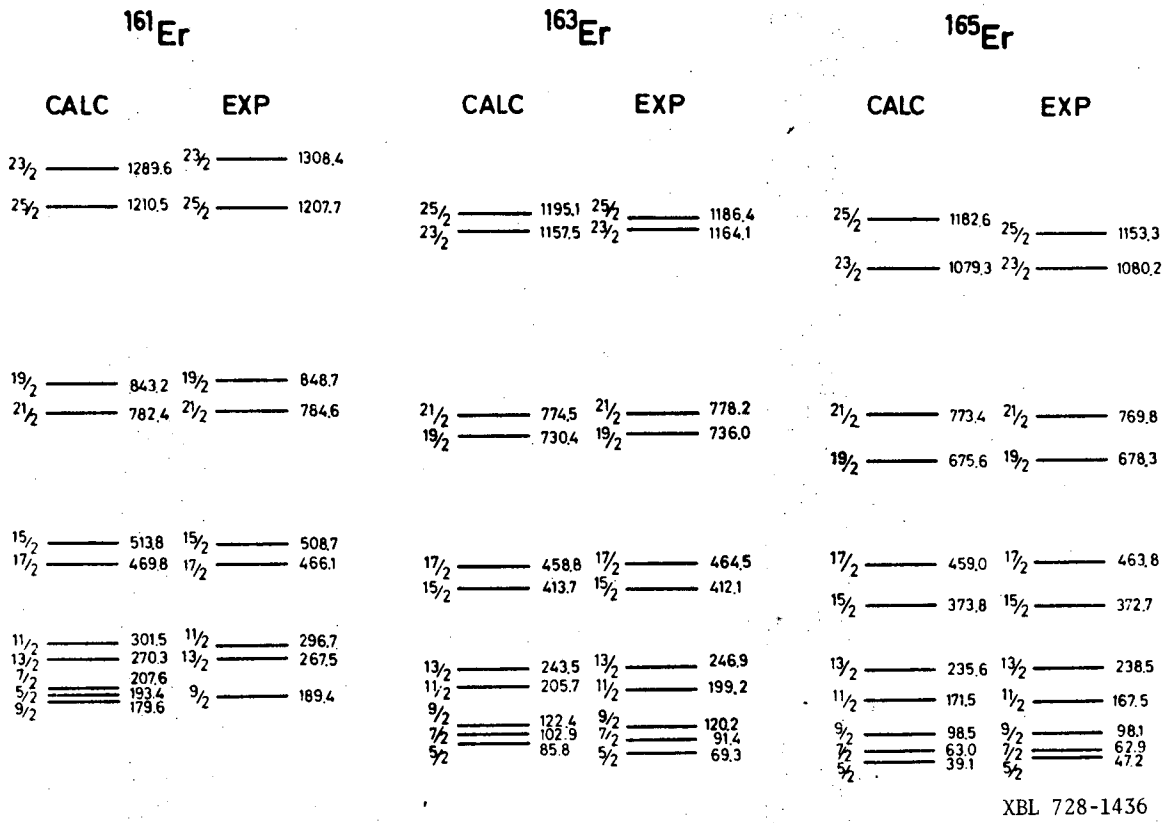

XBL 728-1436

Fig. 7

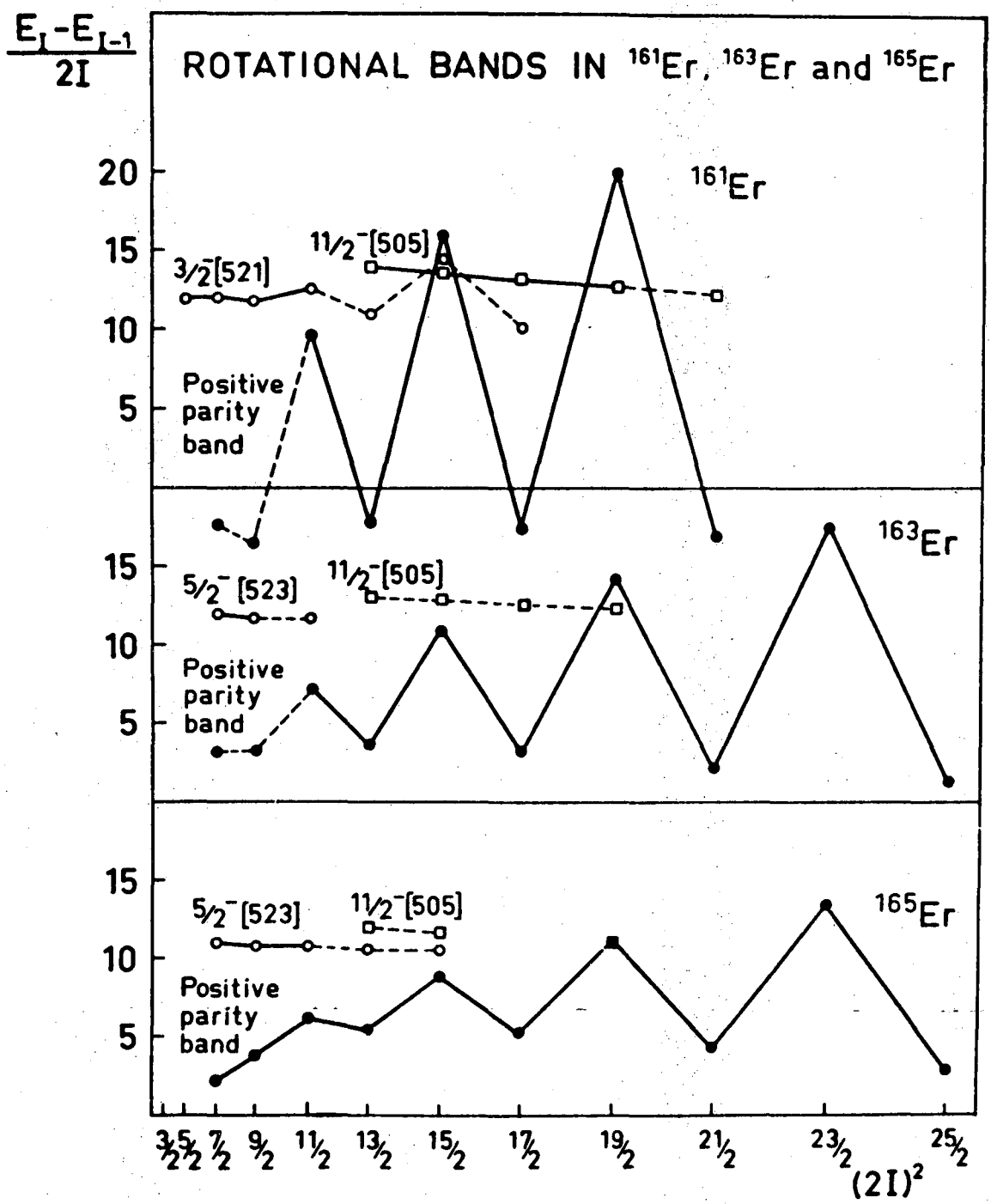

XBL 728-1437

Fig. 8

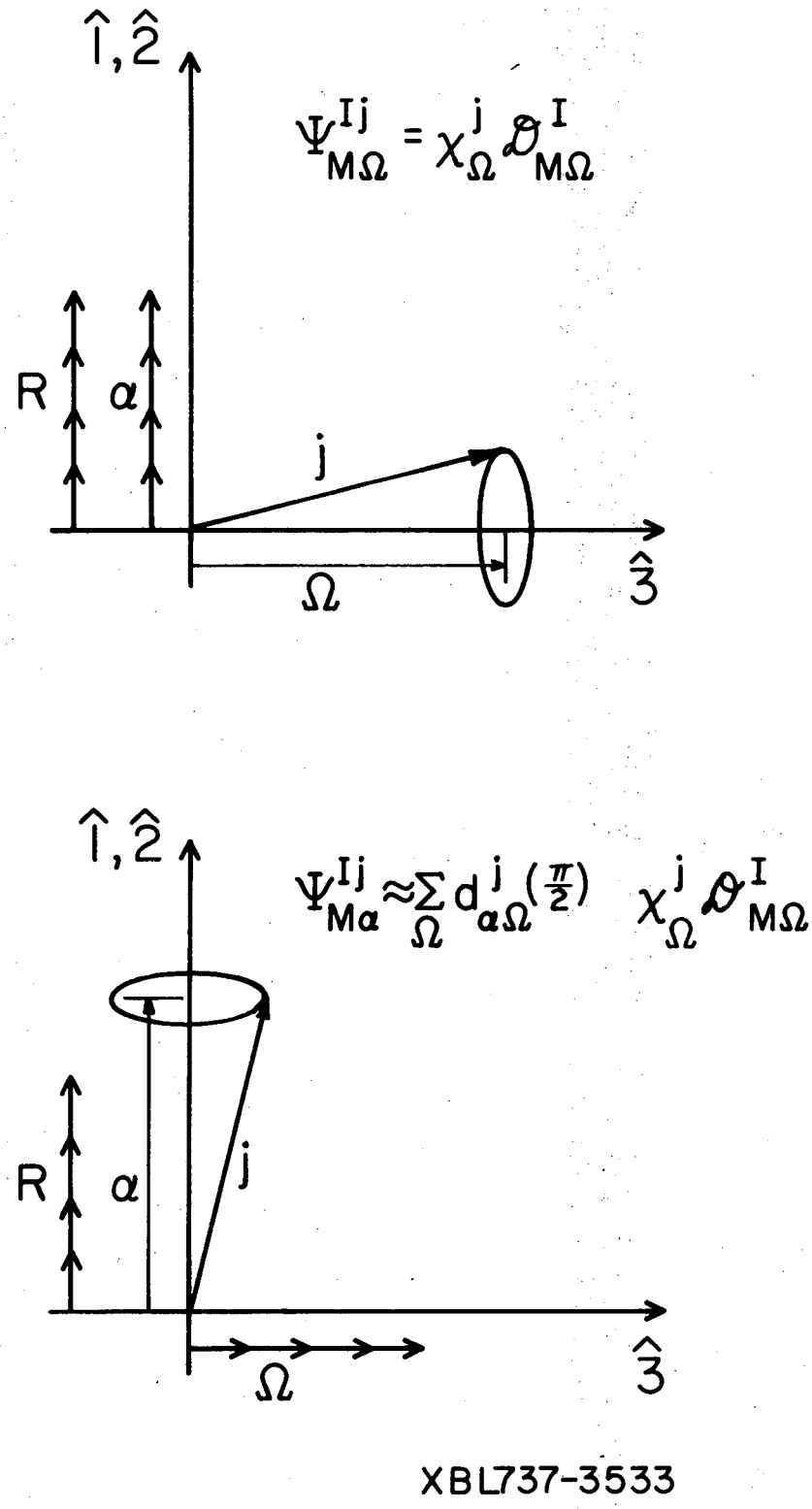
$\hat{1},\hat{2}$
$\Psi^{Ij}_{M\Omega} = \chi^{j}_{\Omega}\mathcal{D}^{I}_{M\Omega}$
R
α
j
Ω
$\hat{3}$
$\hat{1},\hat{2}$
$\Psi^{Ij}_{M\alpha} \approx \sum_{\Omega} d^{j}_{\alpha\Omega}(\frac{\pi}{2})\ \chi^{j}_{\Omega}\mathcal{D}^{I}_{M\Omega}$
R
α
j
Ω
$\hat{3}$
XBL737-3533

Fig. 9

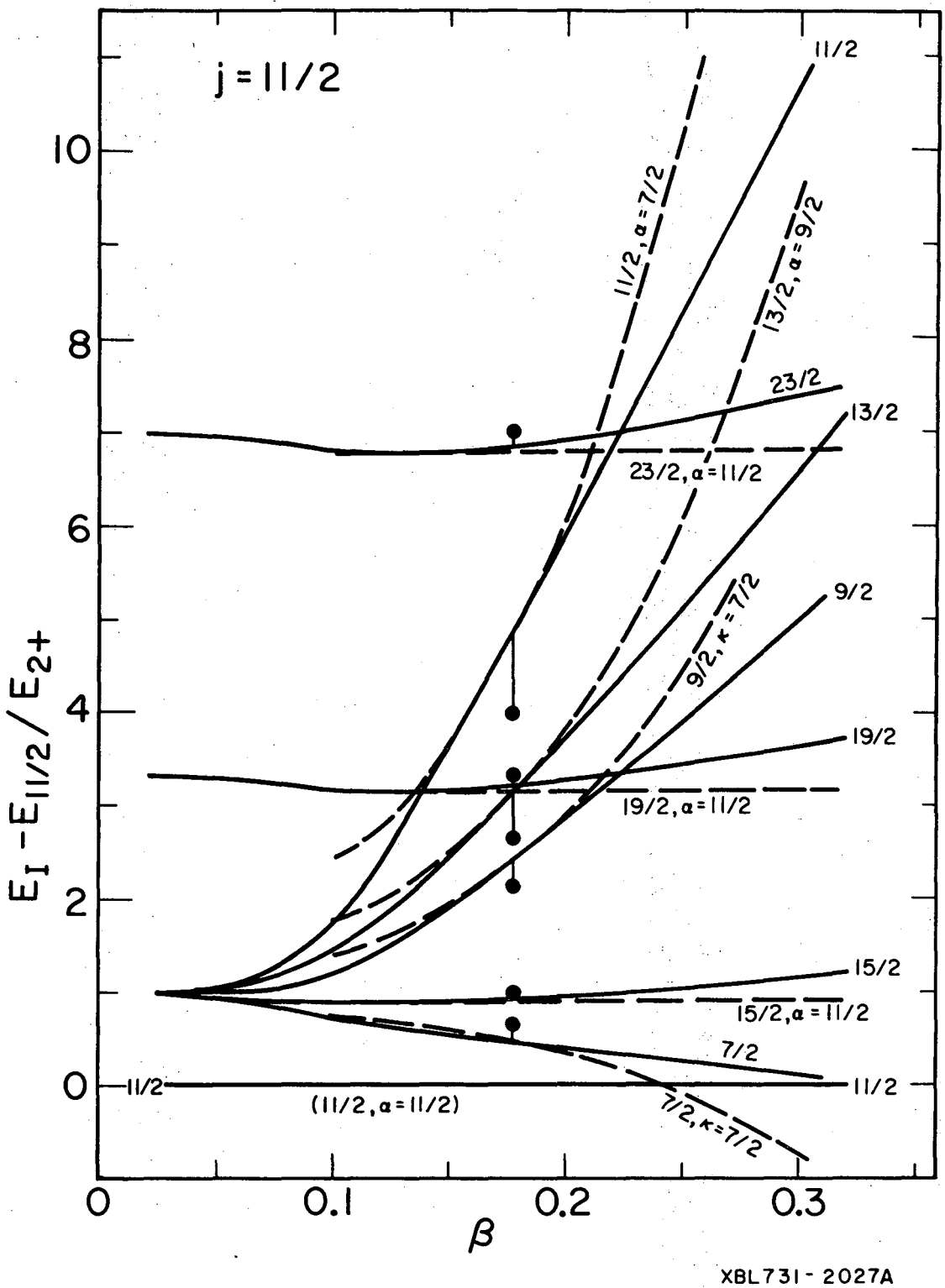
j = 11/2
11/2
11/2, α = 7/2
13/2, α = 9/2
23/2
13/2
23/2, α = 11/2
9/2
9/2, κ = 7/2
19/2
19/2, α = 11/2
15/2
15/2, α = 11/2
7/2
11/2
11/2
(11/2, α = 11/2)
7/2, κ = 7/2
E_I - E_11/2 / E_2+
β
0
2
4
6
8
10
0
0.1
0.2
0.3
XBL731-2027A

Fig. 10

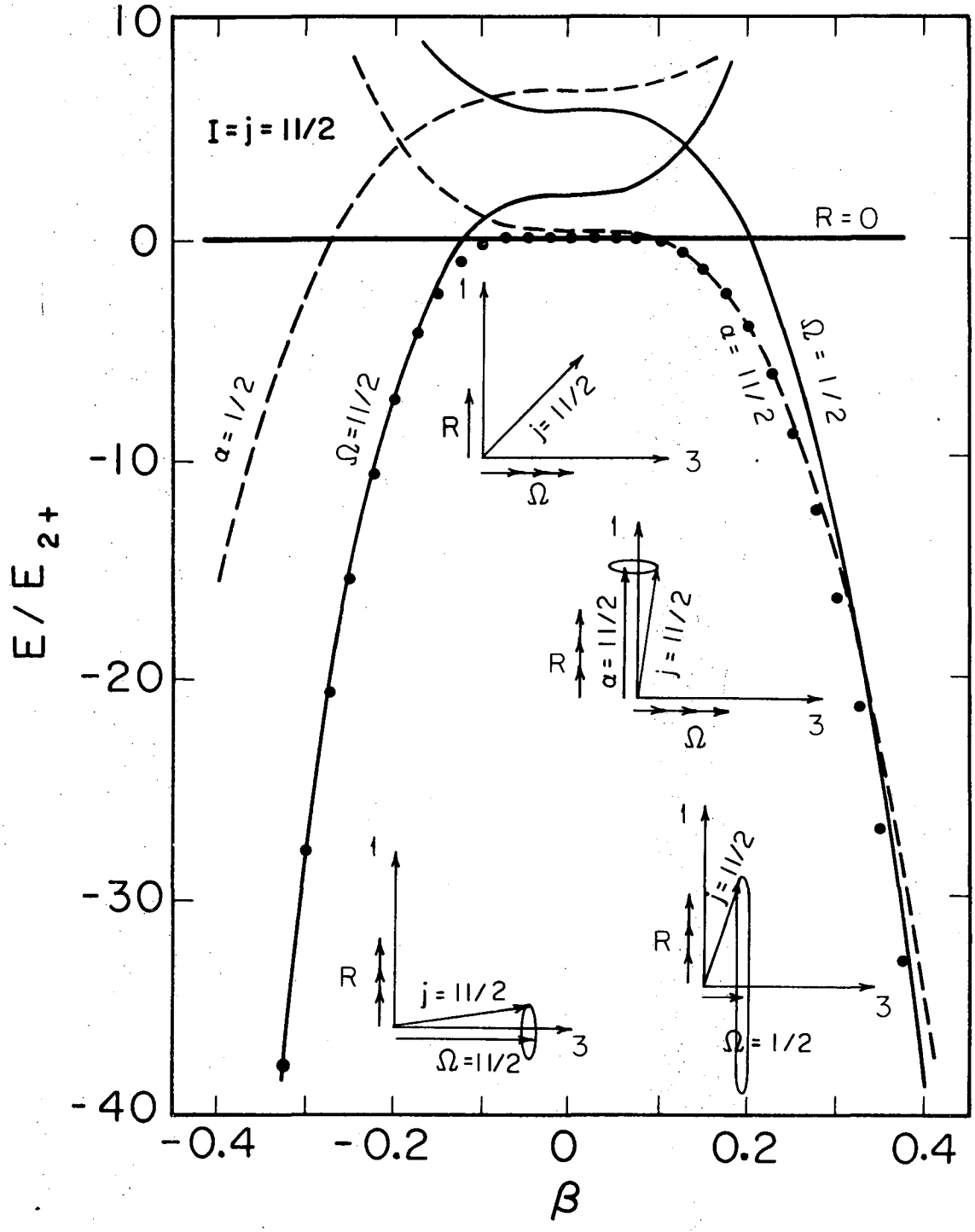

XBL7210-4361a

Fig. 11

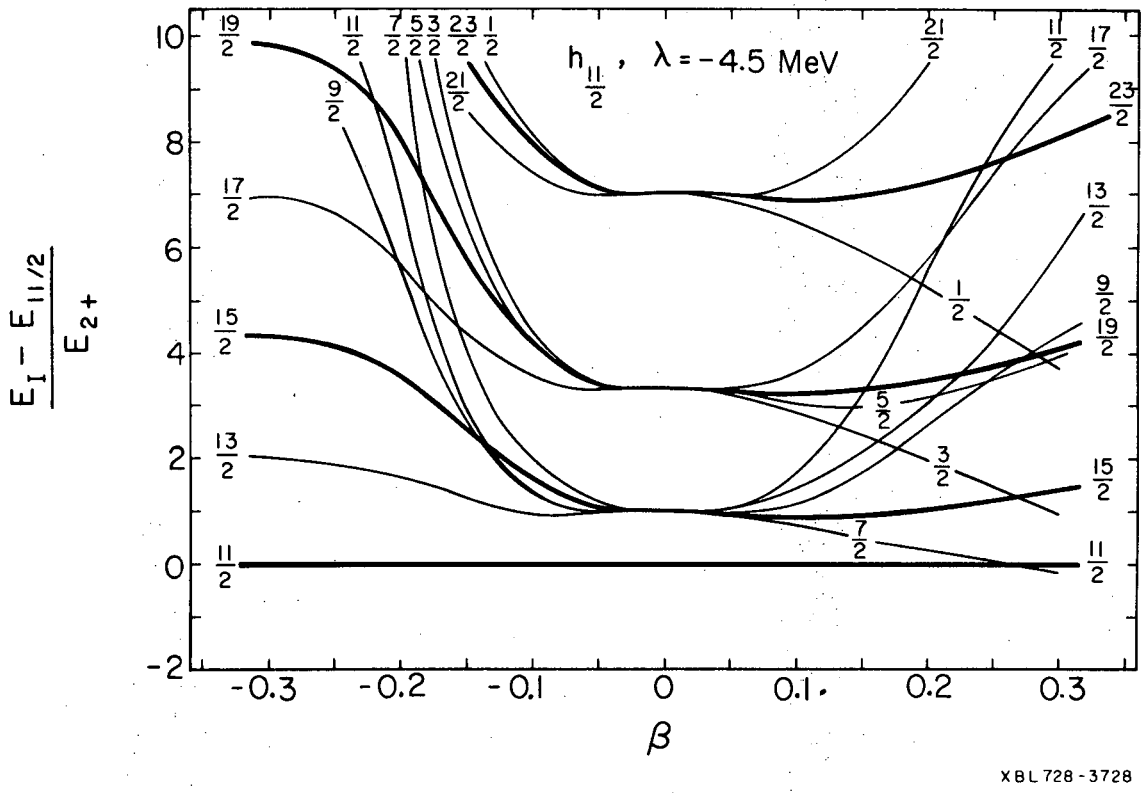
$h_{11/2}$, λ = -4.5 MeV
$\frac{E_I - E_{11/2}}{E_{2+}}$
β
10
8
6
4
2
0
-2
-0.3
-0.2
-0.1
0
0.1
0.2
0.3
19/2
11/2
7/2
5/2
3/2
23/2
1/2
21/2
9/2
17/2
15/2
13/2
11/2
XBL 728-3728

Fig. 12

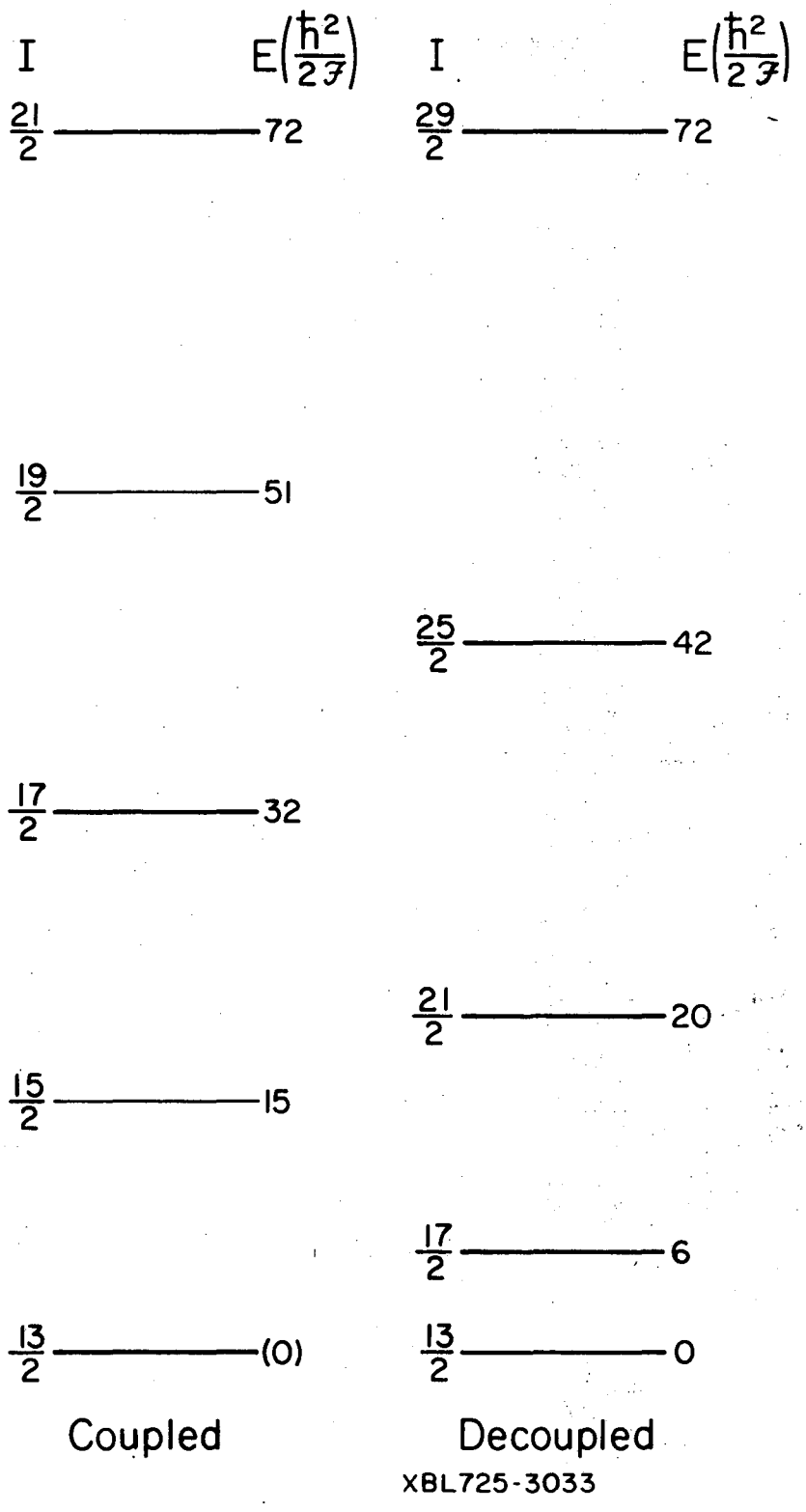
I
E(ħ²/2ℑ)
21/2
72
19/2
51
17/2
32
15/2
15
13/2
(0)
Coupled
I
E(ħ²/2ℑ)
29/2
72
25/2
42
21/2
20
17/2
6
13/2
0
Decoupled
XBL725-3033

Fig. 13

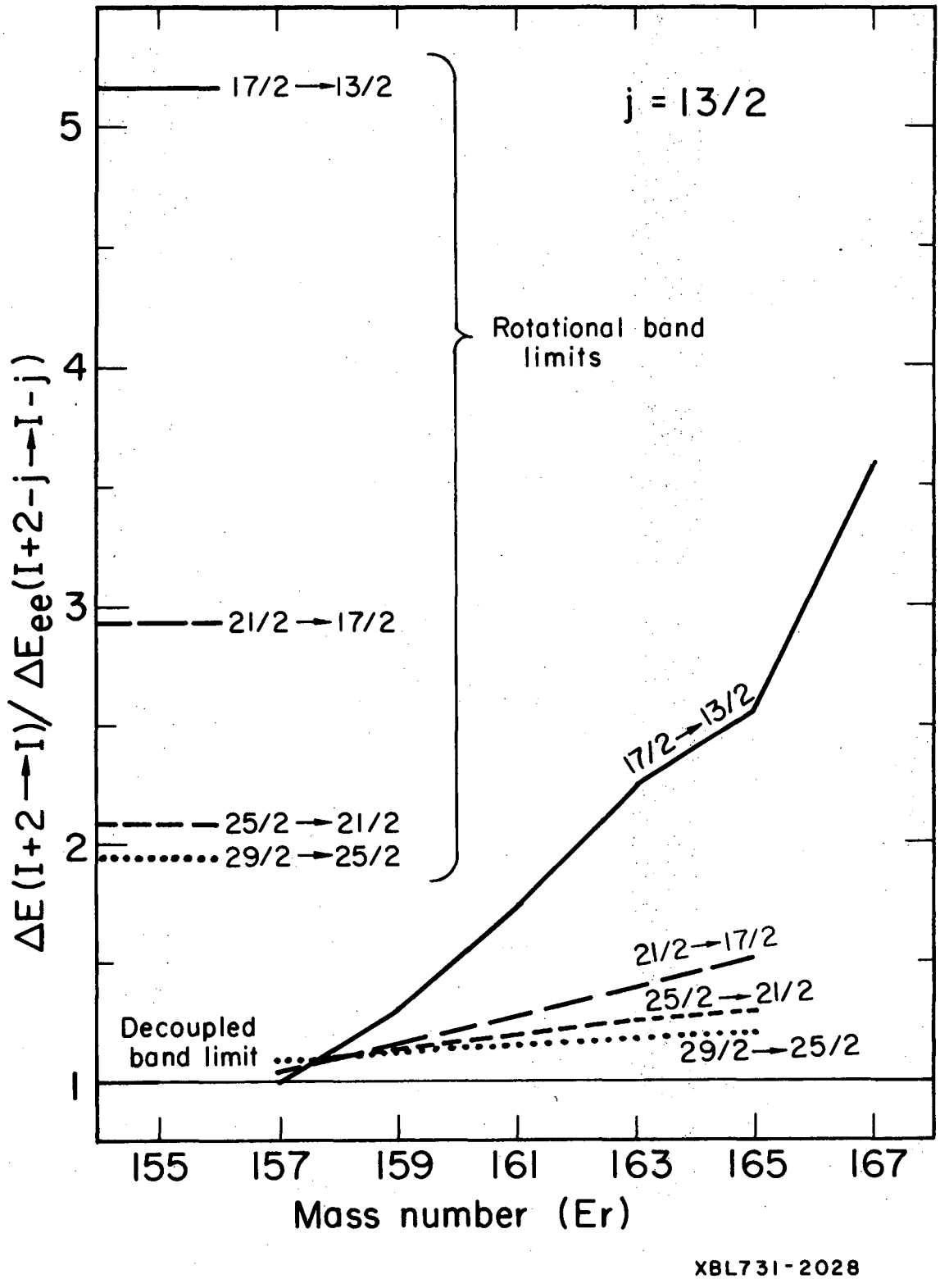
j = 13/2
17/2 → 13/2
21/2 → 17/2
25/2 → 21/2
29/2 → 25/2
Rotational band limits
Decoupled band limit
17/2 → 13/2
21/2 → 17/2
25/2 → 21/2
29/2 → 25/2
ΔE(I+2 → I)/ ΔEee(I+2-j → I-j)
Mass number (Er)
XBL731-2028

Fig. 14

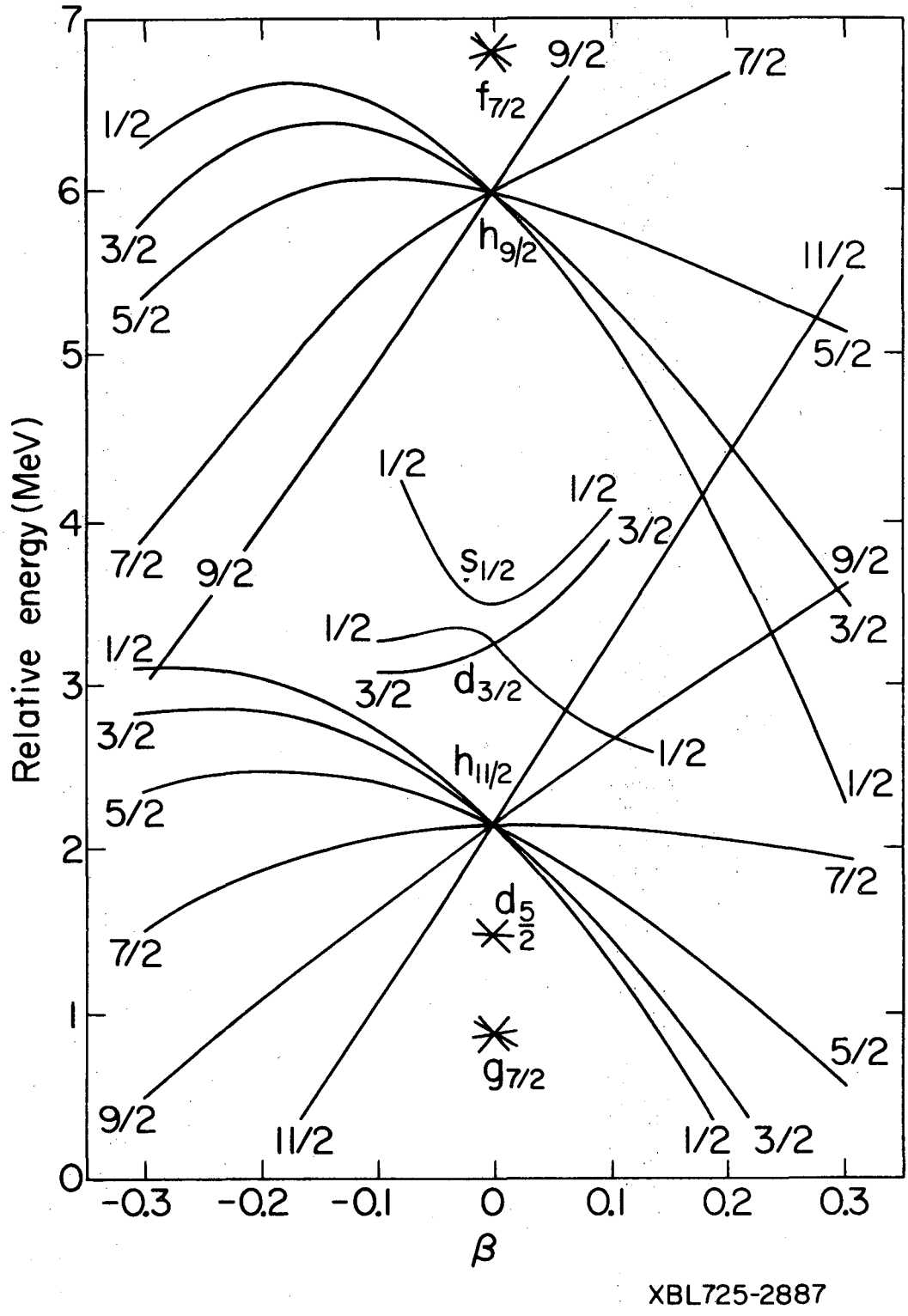
Relative energy (MeV)
β
9/2
7/2
f7/2
1/2
3/2
5/2
h9/2
11/2
5/2
1/2
1/2
3/2
s1/2
7/2
9/2
9/2
3/2
1/2
1/2
3/2
d3/2
1/2
3/2
h11/2
1/2
5/2
7/2
d5/2
7/2
5/2
g7/2
9/2
11/2
1/2
3/2
0
1
2
3
4
5
6
7
-0.3
-0.2
-0.1
0
0.1
0.2
0.3
XBL725-2887

Fig. 15

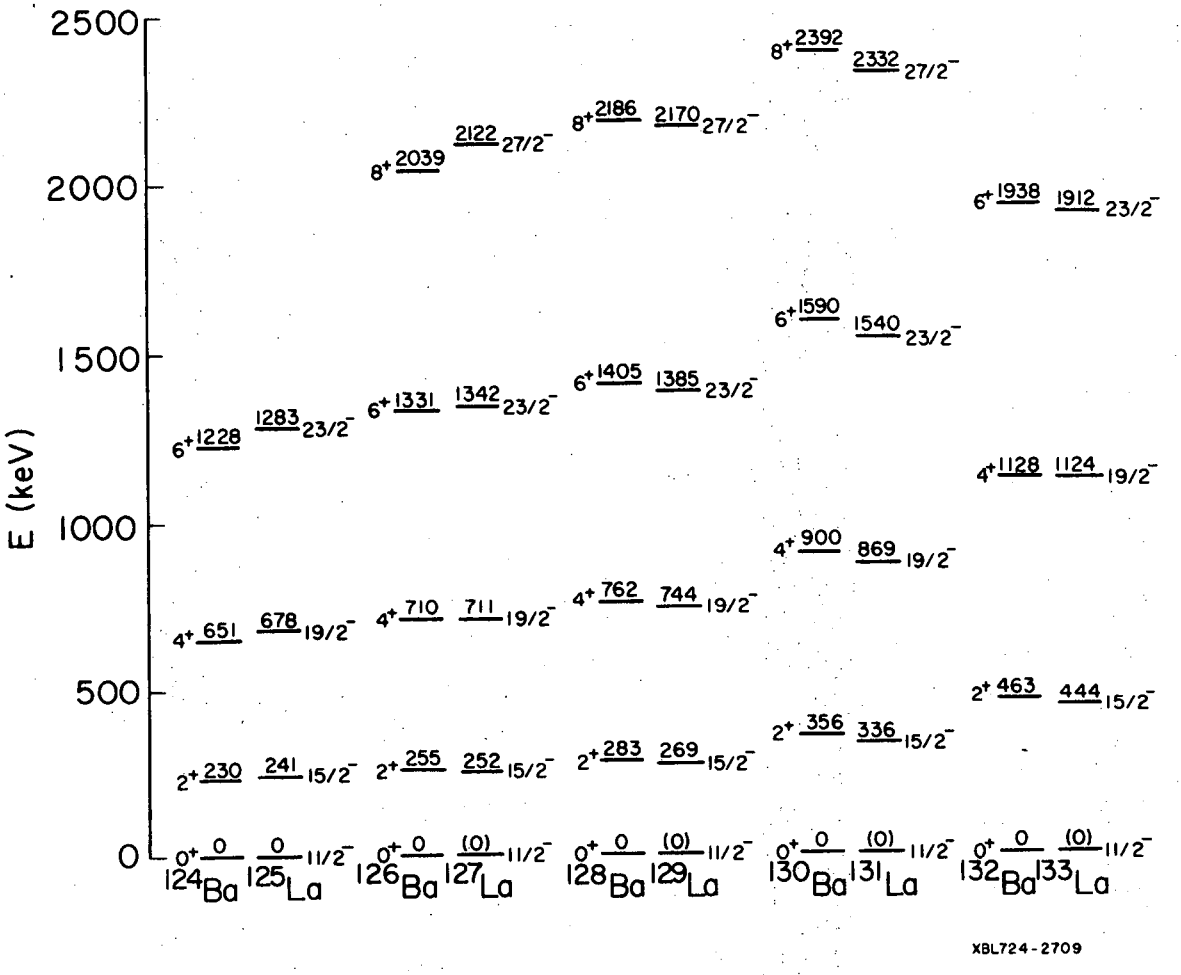
2500
2000
1500
1000
500
0
E (keV)
8+ 2392 2332 27/2−
8+ 2186 2170 27/2−
8+ 2039 2122 27/2−
6+ 1938 1912 23/2−
6+ 1590 1540 23/2−
6+ 1405 1385 23/2−
6+ 1331 1342 23/2−
6+ 1228 1283 23/2−
4+ 1128 1124 19/2−
4+ 900 869 19/2−
4+ 762 744 19/2−
4+ 710 711 19/2−
4+ 651 678 19/2−
2+ 463 444 15/2−
2+ 356 336 15/2−
2+ 283 269 15/2−
2+ 255 252 15/2−
2+ 230 241 15/2−
0+ 0 0 11/2−
0+ 0 (0) 11/2−
124Ba 125La 126Ba 127La 128Ba 129La 130Ba 131La 132Ba 133La
XBL724-2709

Fig. 16

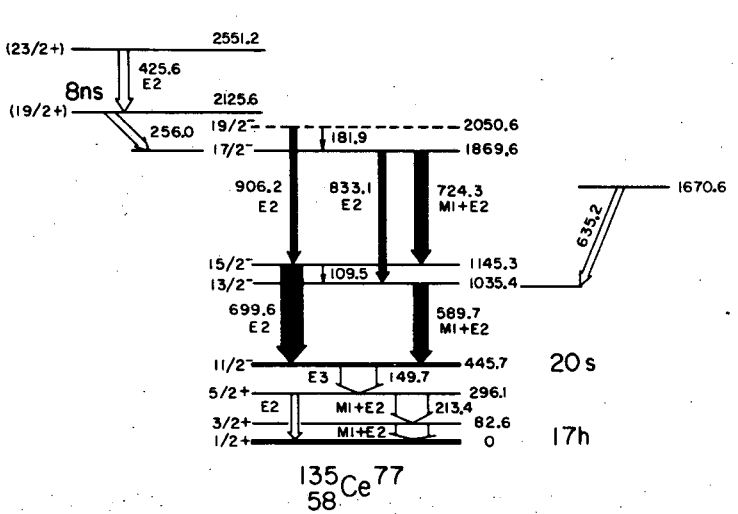
(23/2+)
2551.2
425.6
E2
8ns
(19/2+)
2125.6
256.0
19/2⁻
17/2⁻
181.9
2050.6
1869.6
906.2
E2
833.1
E2
724.3
M1+E2
1670.6
635.2
15/2⁻
13/2⁻
109.5
1145.3
1035.4
699.6
E2
589.7
M1+E2
11/2⁻
445.7
20 s
E3
149.7
5/2+
296.1
E2
M1+E2
213.4
3/2+
82.6
M1+E2
1/2+
0
17h
135 58Ce77

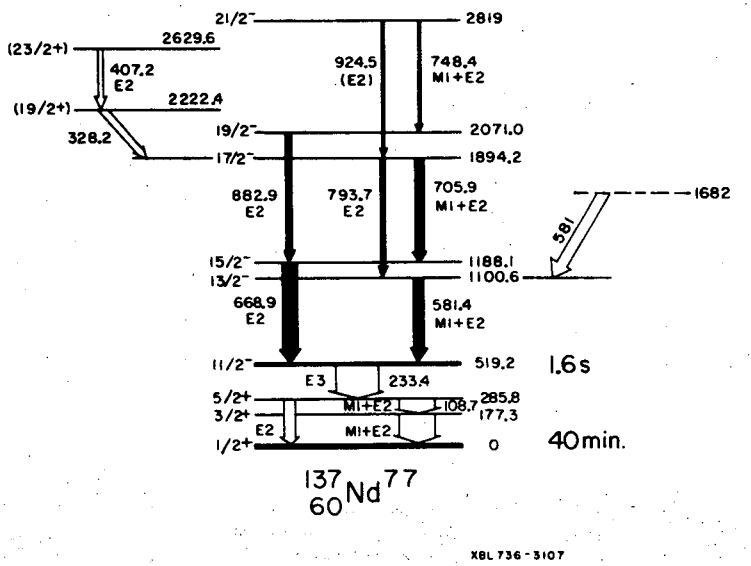
21/2⁻
2819
(23/2+)
2629.6
924.5
(E2)
748.4
M1+E2
407.2
E2
(19/2+)
2222.4
328.2
19/2⁻
2071.0
17/2⁻
1894.2
882.9
E2
793.7
E2
705.9
M1+E2
1682
581
15/2⁻
1188.1
13/2⁻
1100.6
668.9
E2
581.4
M1+E2
11/2⁻
519.2
1.6s
E3
233.4
5/2+
285.8
M1+E2
108.7
3/2+
177.3
E2
M1+E2
1/2+
0
40min.
137 60Nd77
XBL 736-3107

Fig. 17

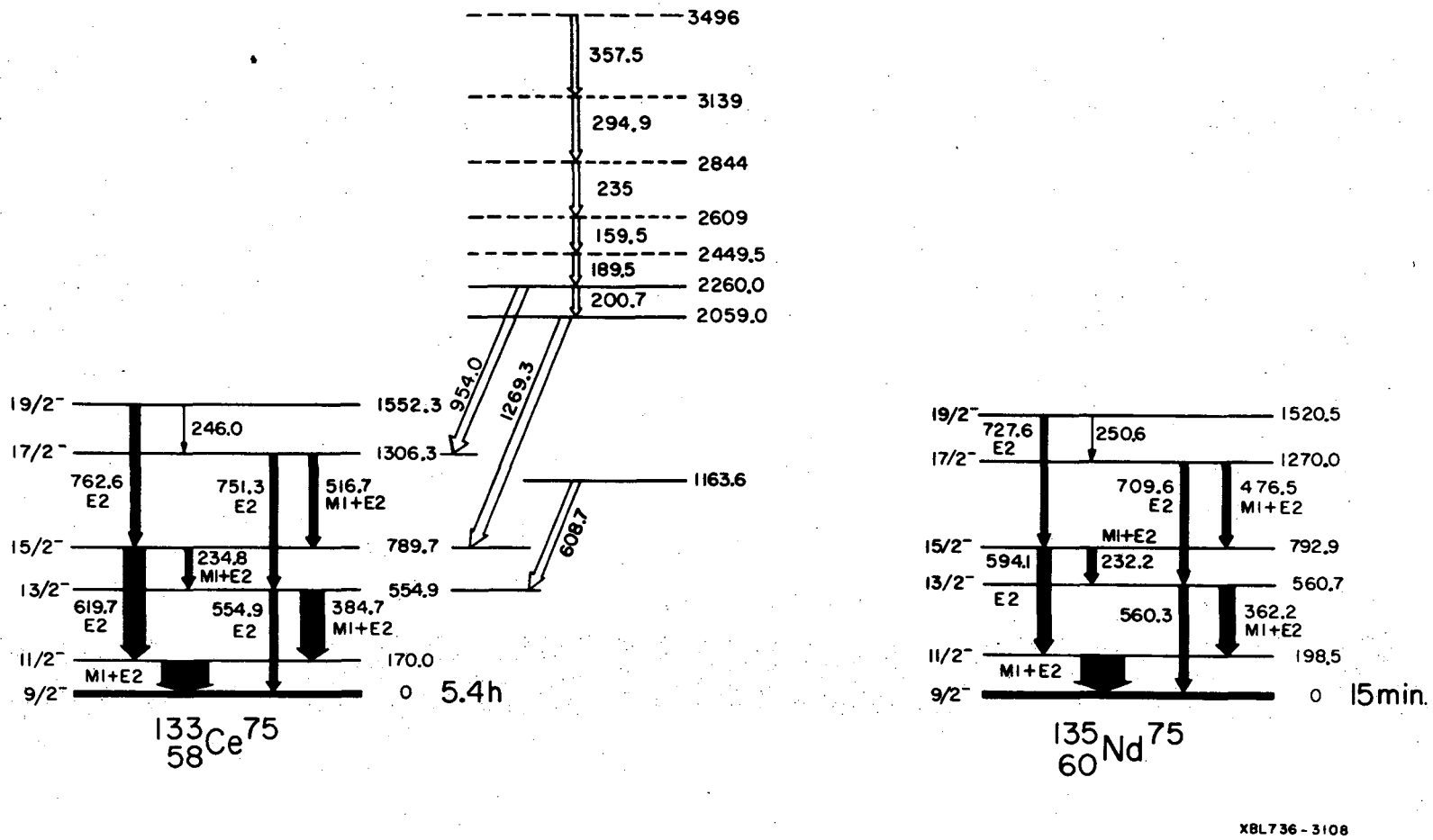
3496
357.5
3139
294.9
2844
235
2609
159.5
2449.5
189.5
2260.0
200.7
2059.0
954.0
1269.3
19/2⁻
1552.3
246.0
17/2⁻
1306.3
762.6
E2
751.3
E2
516.7
M1+E2
1163.6
608.7
15/2⁻
789.7
234.8
M1+E2
13/2⁻
554.9
619.7
E2
554.9
E2
384.7
M1+E2
11/2⁻
170.0
M1+E2
9/2⁻
0
5.4h
133 58 Ce 75
727.6
E2
250.6
1520.5
17/2⁻
1270.0
709.6
E2
476.5
M1+E2
M1+E2
15/2⁻
594.1
232.2
792.9
13/2⁻
E2
560.7
560.3
362.2
M1+E2
11/2⁻
198.5
M1+E2
9/2⁻
0
15min.
135 60 Nd 75
X8L736-3108

Fig. 18

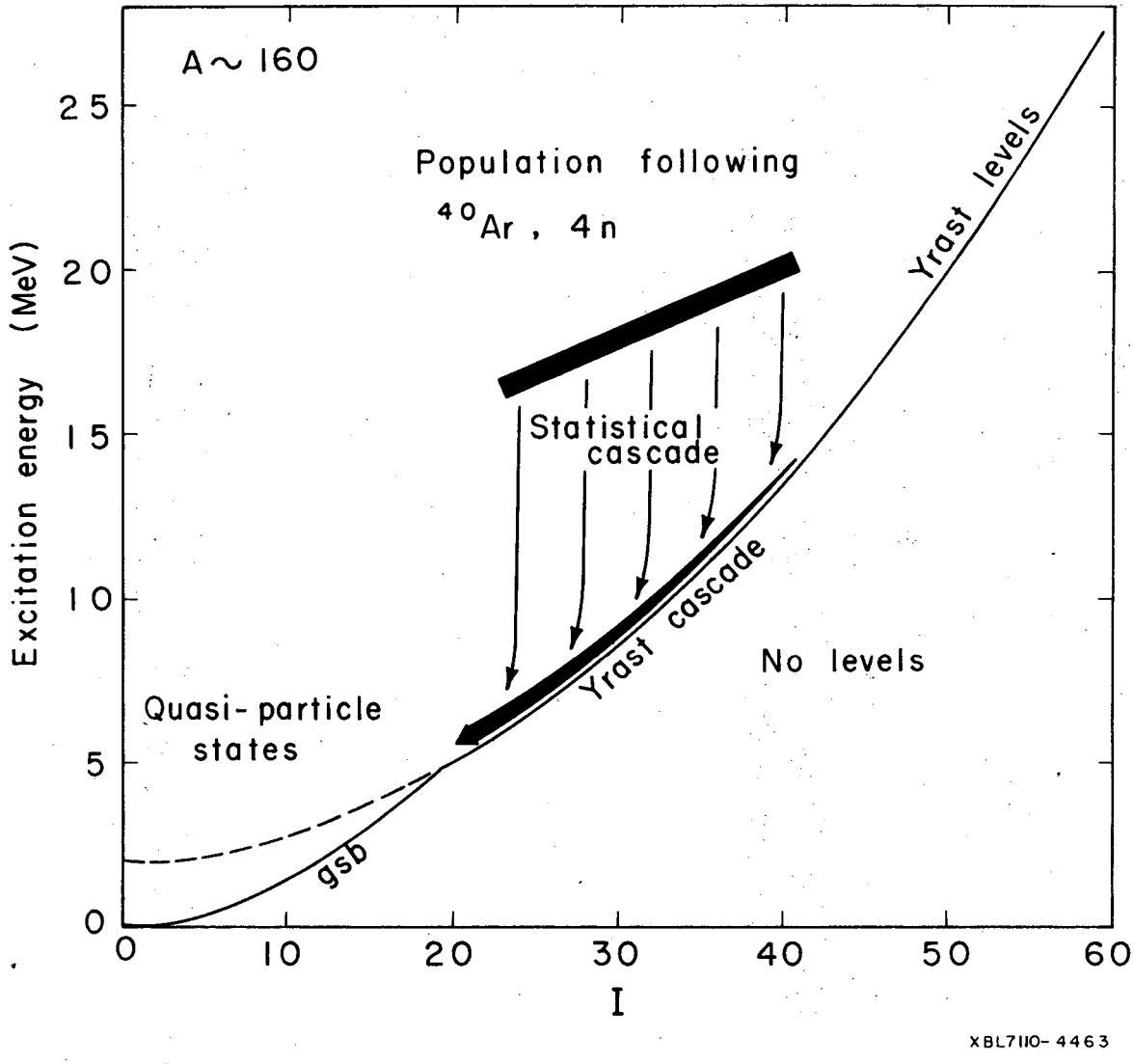
A ~ 160
Population following
40Ar , 4n
Yrast levels
Statistical cascade
Yrast cascade
No levels
Quasi-particle states
gsb
Excitation energy (MeV)
I
0
5
10
15
20
25
0
10
20
30
40
50
60
XBL7110-4463

Fig. 19

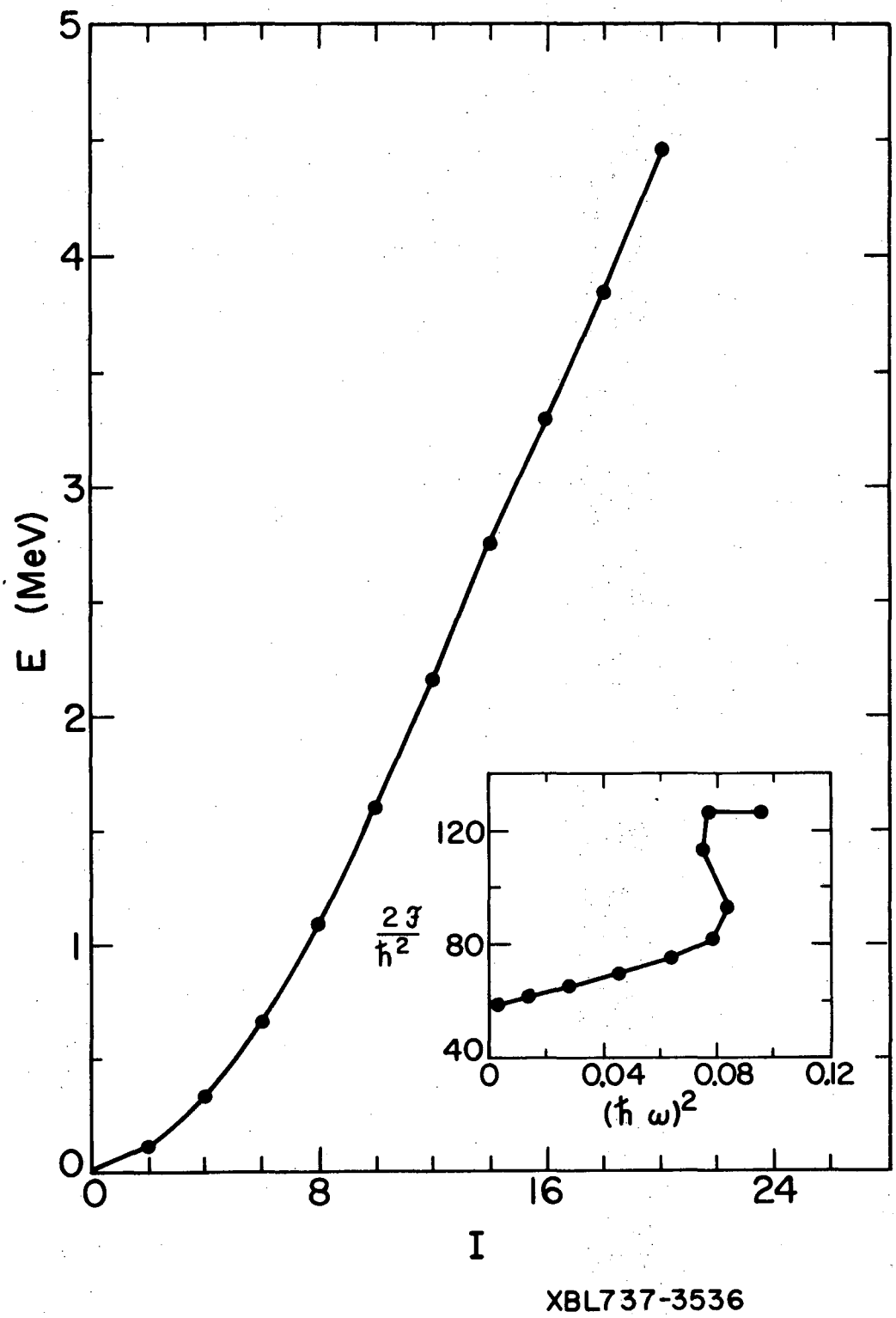
5
4
3
2
1
0
E (MeV)
0
8
16
24
I
120
80
40
$\frac{2\mathcal{I}}{\hbar^2}$
0
0.04
0.08
0.12
$(\hbar\omega)^2$
XBL737-3536

Fig. 20

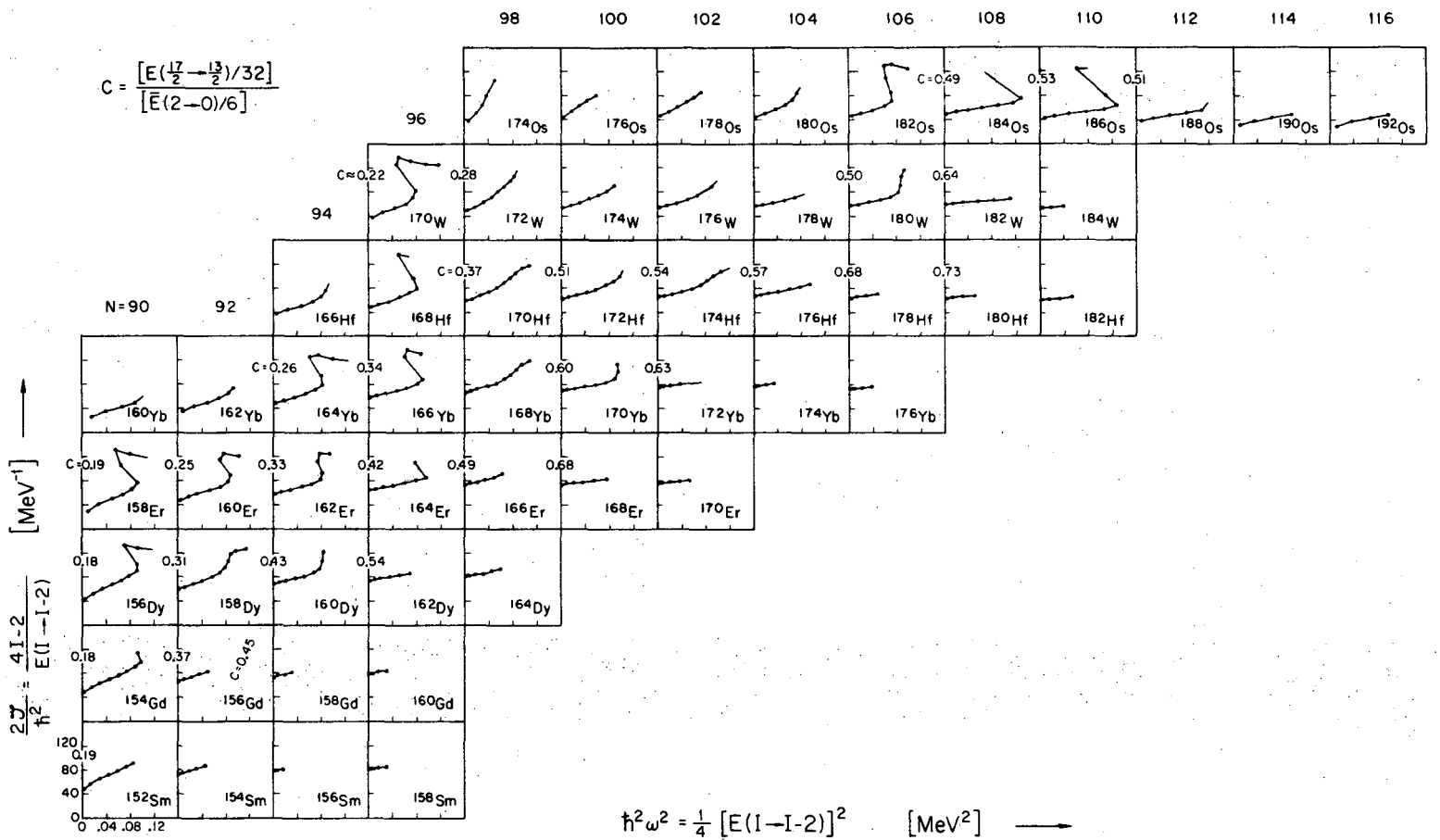
$C = \frac{[E(\frac{17}{2} \rightarrow \frac{13}{2})/32]}{[\bar{E}(2 \rightarrow 0)/6]}$
98
100
102
104
106
108
110
112
114
116
96
94
N=90
92
^{174}Os
^{176}Os
^{178}Os
^{180}Os
^{182}Os
^{184}Os
^{186}Os
^{188}Os
^{190}Os
^{192}Os
C=0.49
0.53
0.51
C≈0.22
0.28
^{170}W
^{172}W
^{174}W
^{176}W
^{178}W
^{180}W
^{182}W
^{184}W
0.50
0.64
C=0.37
0.51
0.54
0.57
0.68
0.73
^{166}Hf
^{168}Hf
^{170}Hf
^{172}Hf
^{174}Hf
^{176}Hf
^{178}Hf
^{180}Hf
^{182}Hf
C=0.26
0.34
0.60
0.63
^{160}Yb
^{162}Yb
^{164}Yb
^{166}Yb
^{168}Yb
^{170}Yb
^{172}Yb
^{174}Yb
^{176}Yb
C=0.19
0.25
0.33
0.42
0.49
0.68
^{158}Er
^{160}Er
^{162}Er
^{164}Er
^{166}Er
^{168}Er
^{170}Er
0.18
0.31
0.43
0.54
^{156}Dy
^{158}Dy
^{160}Dy
^{162}Dy
^{164}Dy
0.18
0.37
C=0.45
^{154}Gd
^{156}Gd
^{158}Gd
^{160}Gd
120
80
40
0
0.19
^{152}Sm
^{154}Sm
^{156}Sm
^{158}Sm
0 .04 .08 .12
$\frac{2\mathcal{J}}{\hbar^2} = \frac{4I-2}{E(I \rightarrow I-2)}$ [MeV^{-1}]
$\hbar^2\omega^2 = \frac{1}{4}[E(I \rightarrow I-2)]^2$ [MeV^2]
XBL7312-6974

Fig. 21

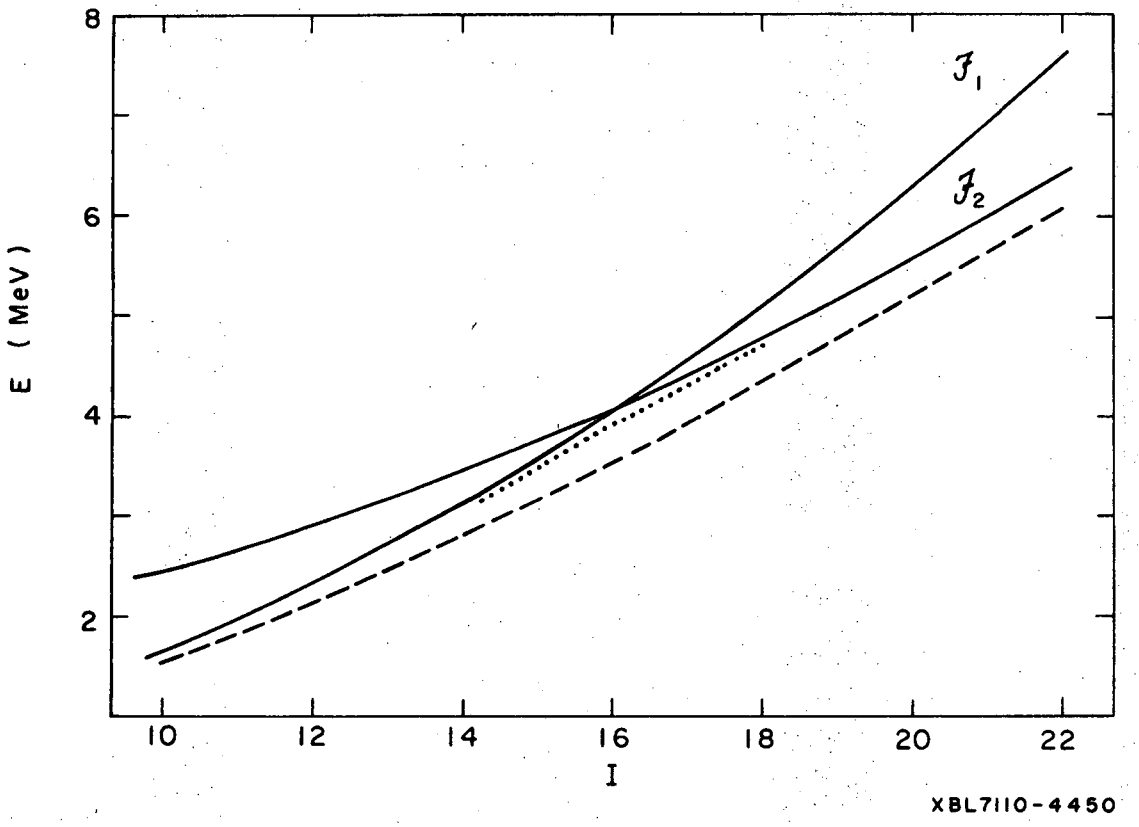
8
6
4
2
E (MeV)
10
12
14
16
18
20
22
I
$\mathcal{J}_1$
$\mathcal{J}_2$
XBL7110-4450

Fig. 22

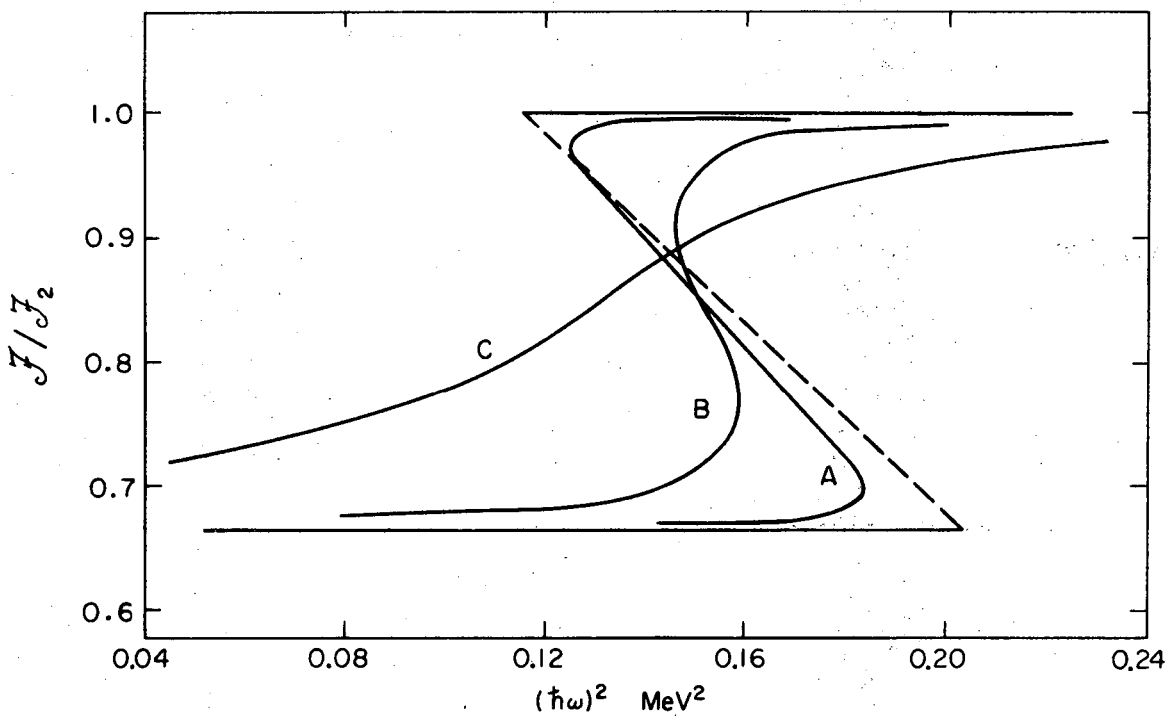
1.0
0.9
0.8
0.7
0.6
$\mathcal{I}/\mathcal{I}_2$
C
B
A
0.04
0.08
0.12
0.16
0.20
0.24
$(\hbar\omega)^2$ MeV^2
XBL7110-4451

Fig. 23

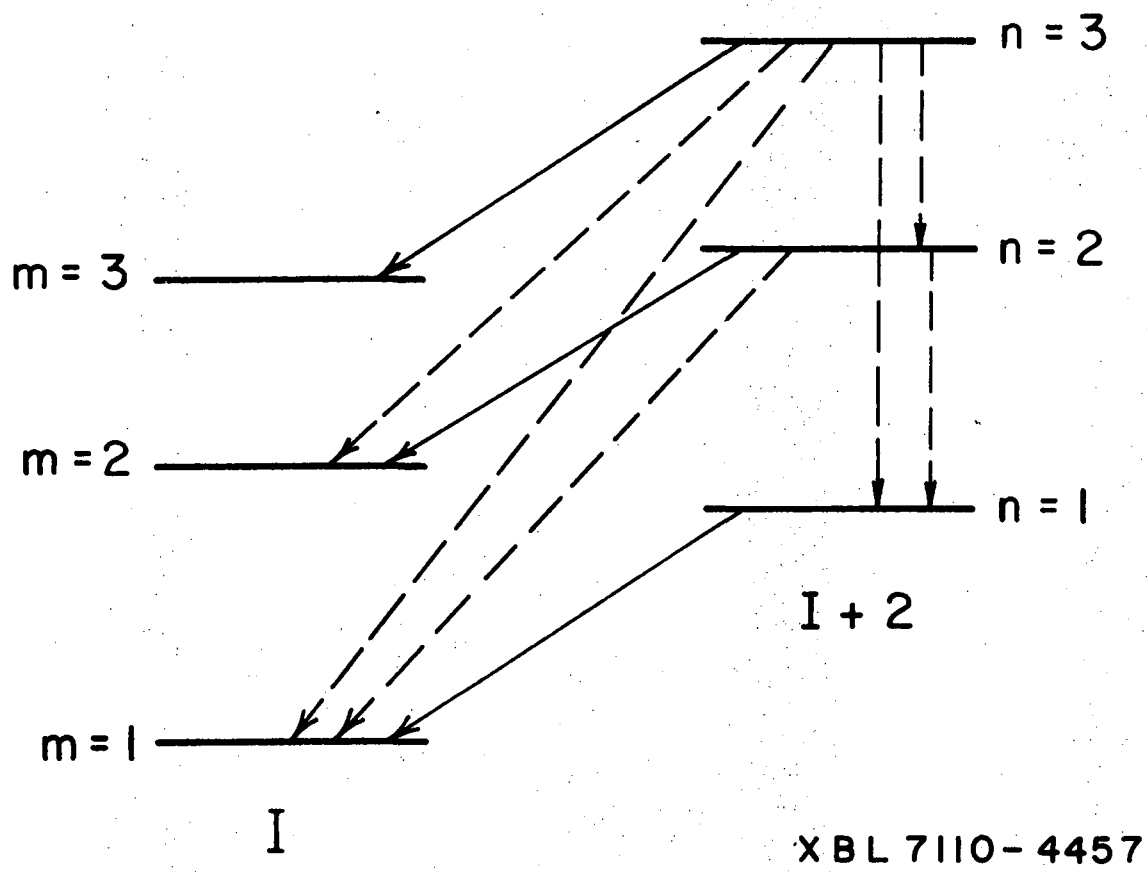

Fig. 24

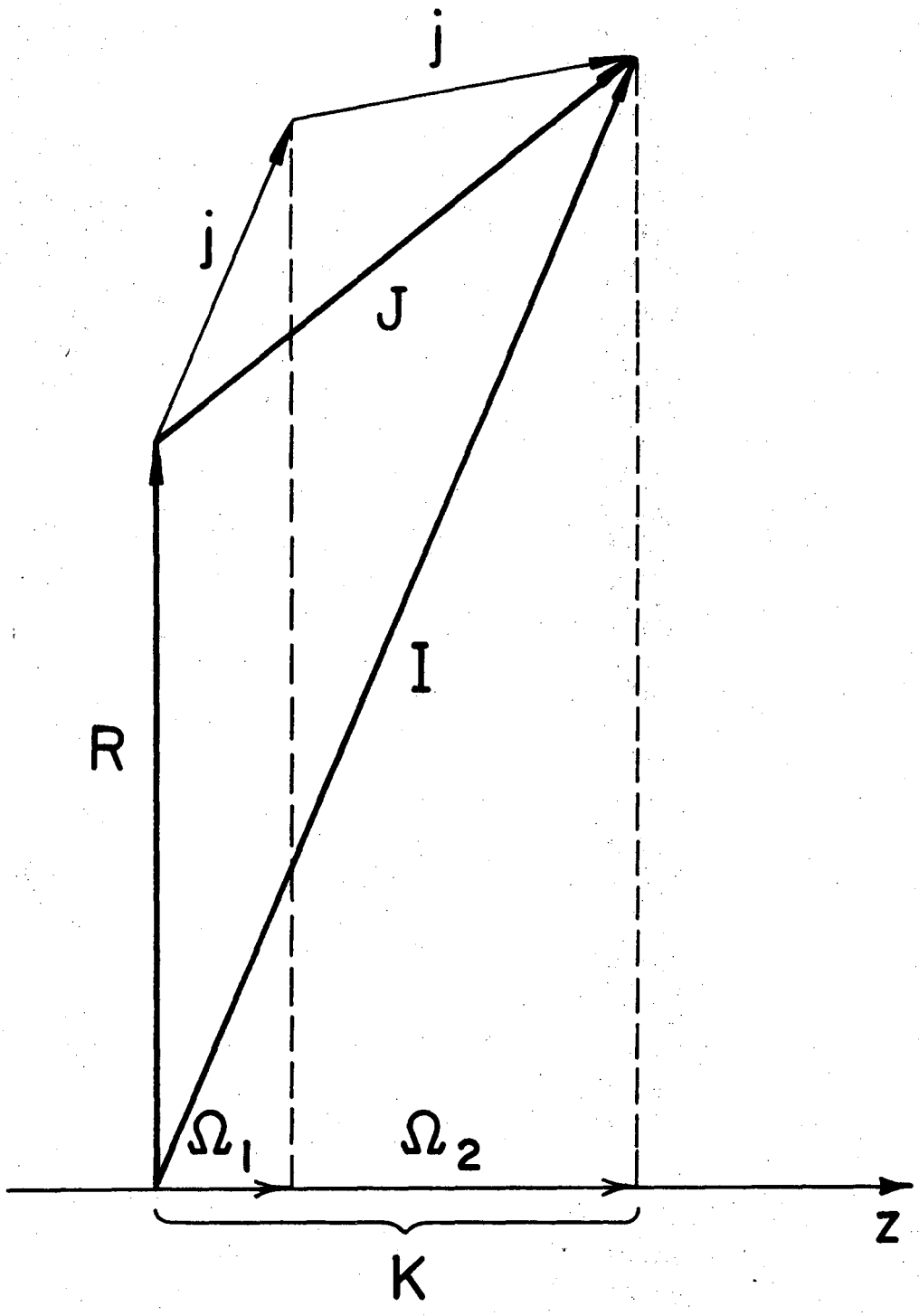

Fig. 25

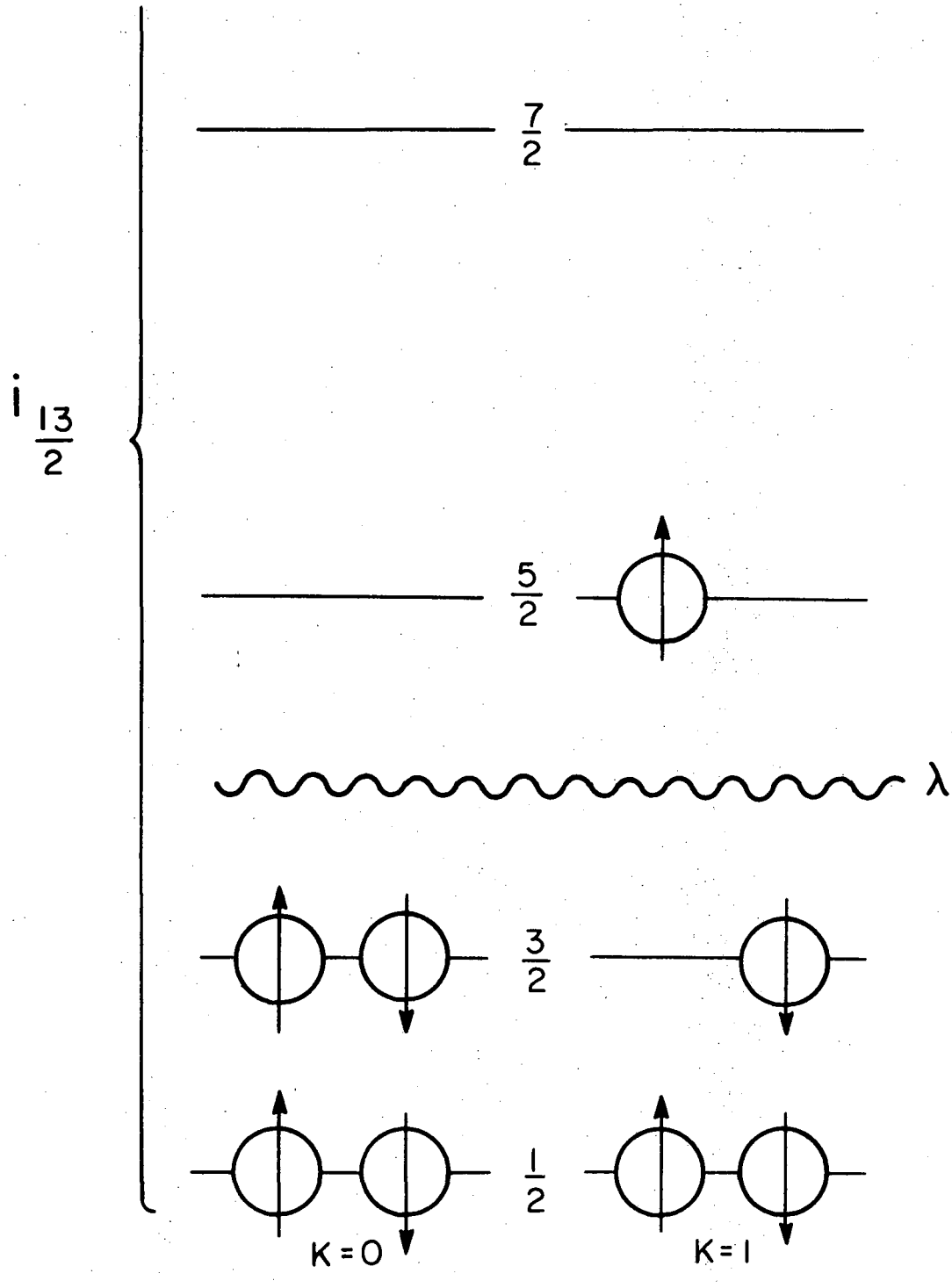

XBL7110-4455

Fig. 26

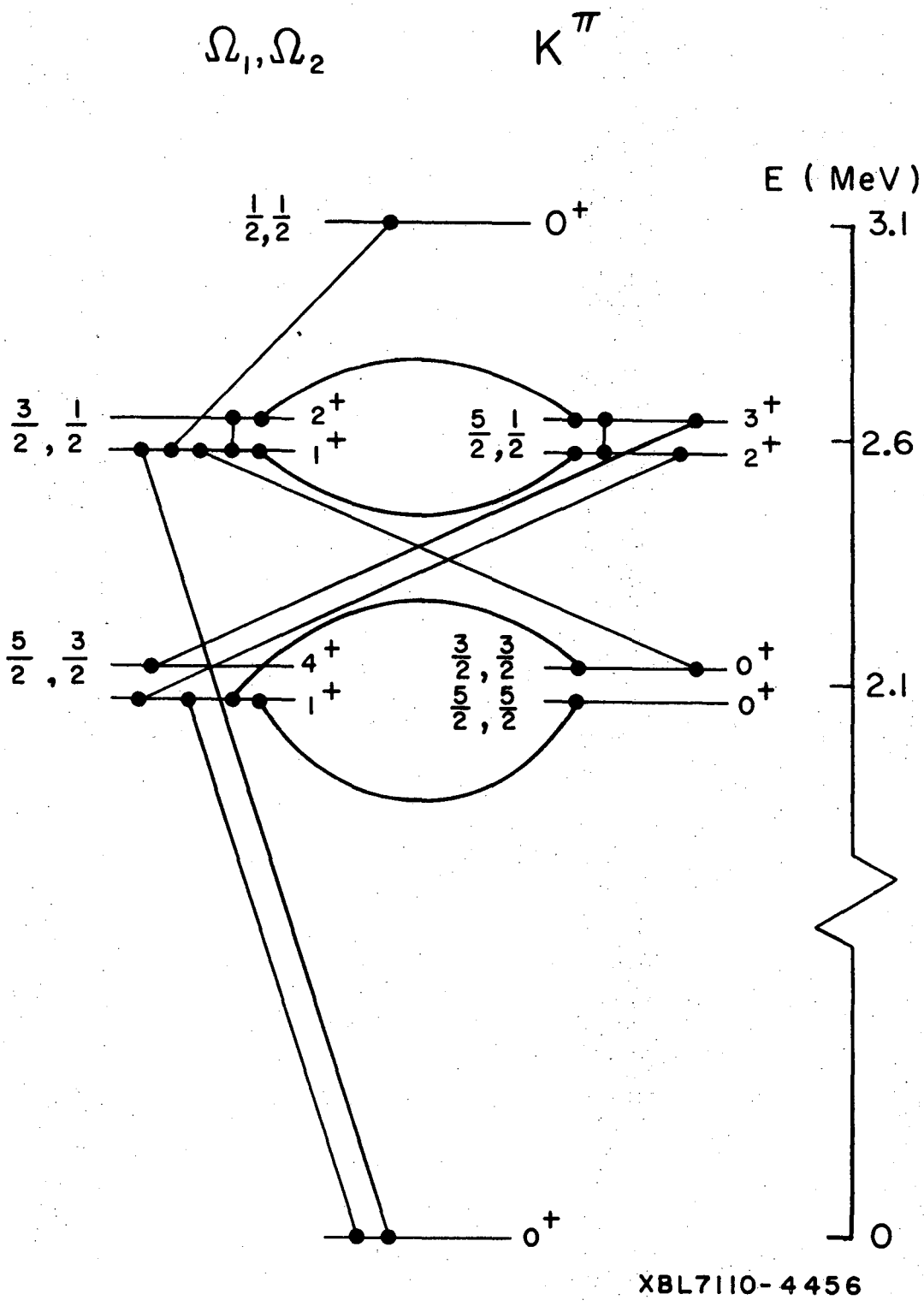
Ω_1, Ω_2
K^π
E (MeV)
3.1
2.6
2.1
0
$\frac{1}{2},\frac{1}{2}$ 0^+
$\frac{3}{2},\frac{1}{2}$ 2^+ 1^+
$\frac{5}{2},\frac{1}{2}$ 3^+ 2^+
$\frac{5}{2},\frac{3}{2}$ 4^+ 1^+
$\frac{3}{2},\frac{3}{2}$ 0^+
$\frac{5}{2},\frac{5}{2}$ 0^+
0^+
XBL7110-4456

Fig. 27

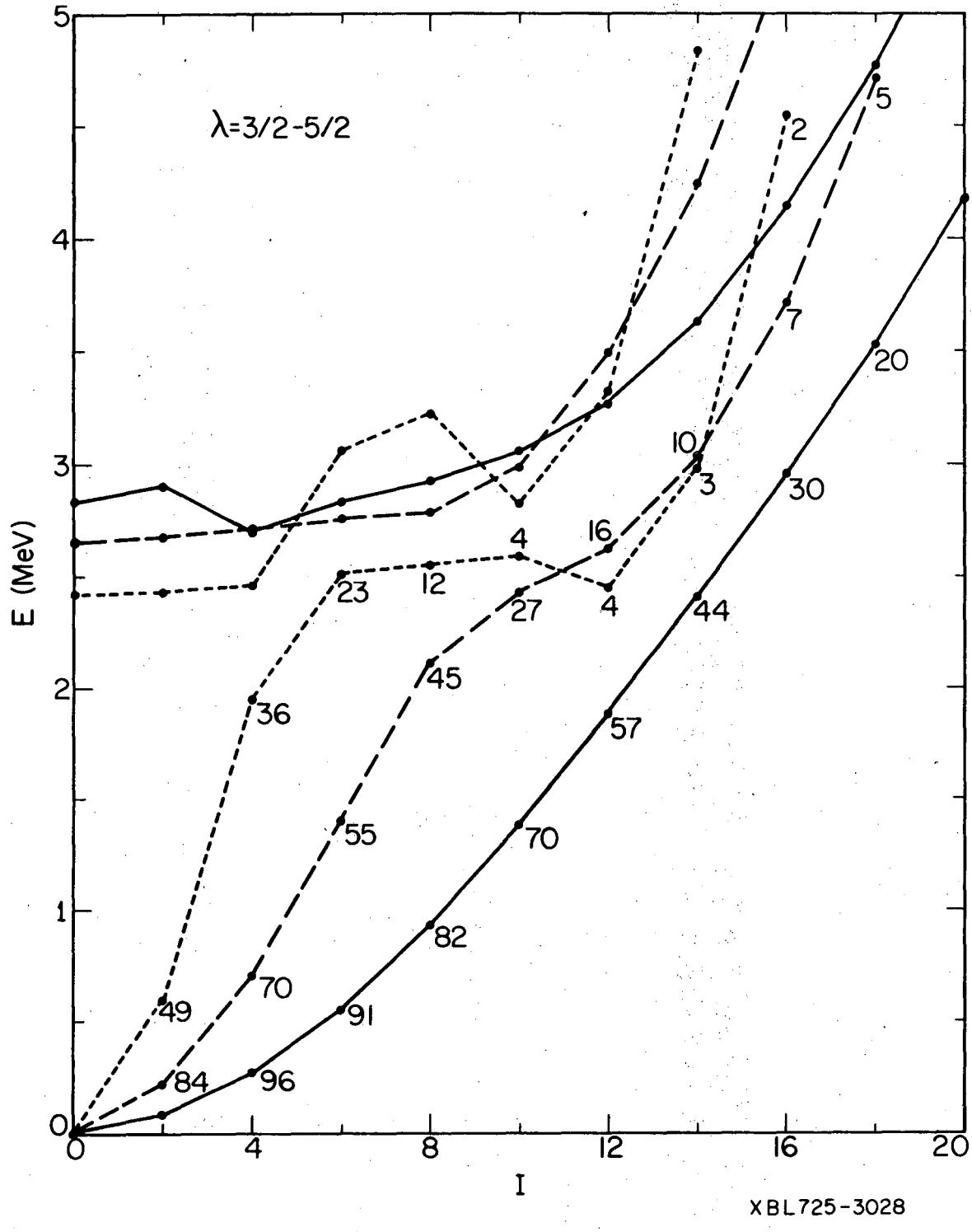
λ=3/2-5/2
E (MeV)
I
0
1
2
3
4
5
0
4
8
12
16
20
49
84
36
70
23
55
12
45
4
27
16
4
10
3
2
5
7
30
20
44
57
70
82
91
96
XBL725-3028

Fig. 28

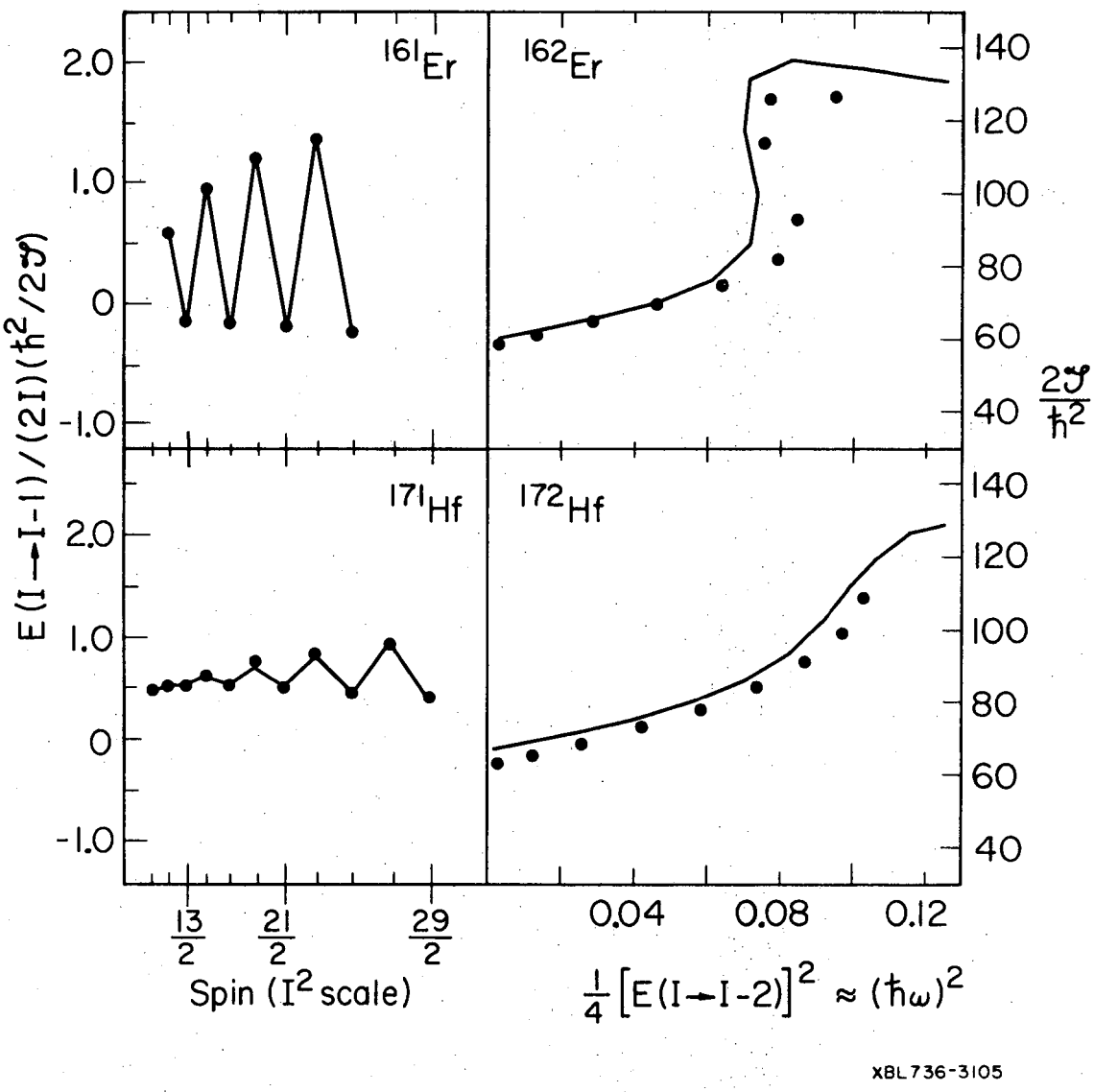
^{161}Er
^{162}Er
^{171}Hf
^{172}Hf
$E(I \rightarrow I-1)/(2I)(\hbar^2/2\mathcal{J})$
$\frac{2\mathcal{J}}{\hbar^2}$
2.0
1.0
0
-1.0
140
120
100
80
60
40
$\frac{13}{2}$
$\frac{21}{2}$
$\frac{29}{2}$
Spin (I^2 scale)
0.04
0.08
0.12
$\frac{1}{4}[E(I \rightarrow I-2)]^2 \approx (\hbar\omega)^2$
XBL736-3105

Fig. 29

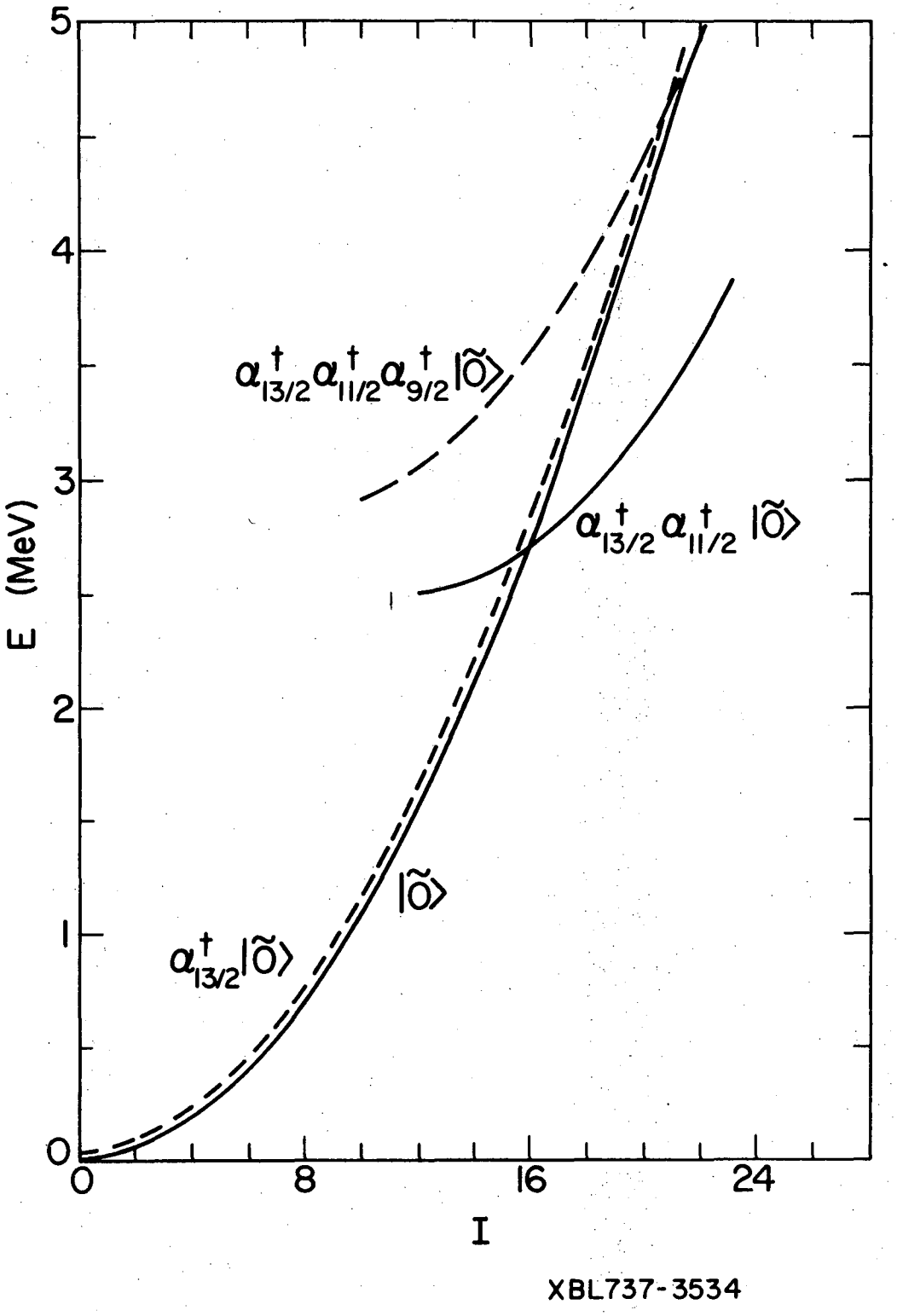

XBL737-3534

Fig. 30

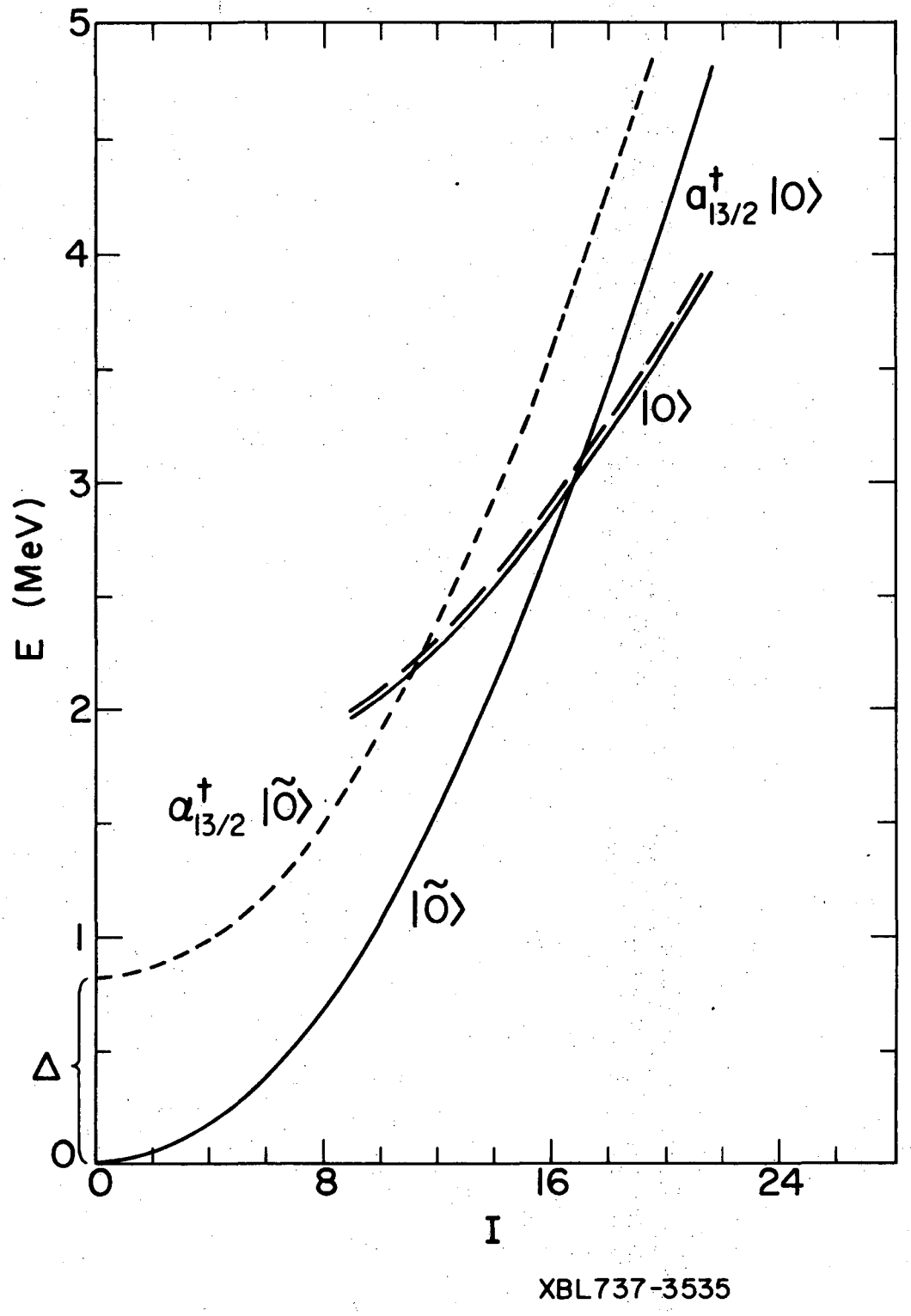
5
4
3
2
1
0
E (MeV)
Δ
0
8
16
24
I
$a^{\dagger}_{13/2}|0\rangle$
$|0\rangle$
$a^{\dagger}_{13/2}|\tilde{0}\rangle$
$|\tilde{0}\rangle$
XBL737-3535

Fig. 31

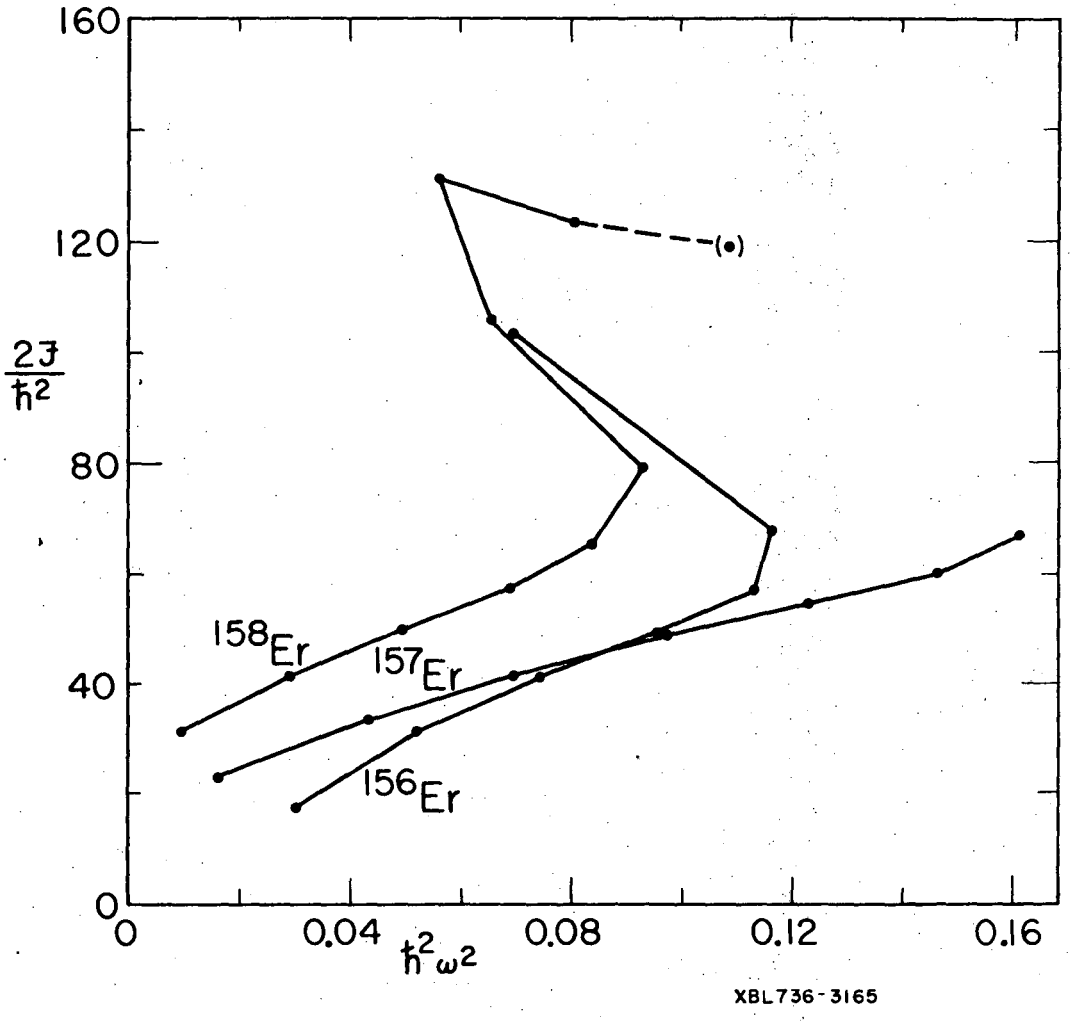
160
120
80
40
0
$\frac{2\mathcal{J}}{\hbar^2}$
(•)
^{158}Er
^{157}Er
^{156}Er
0
0.04
0.08
0.12
0.16
$\hbar^2\omega^2$
XBL736-3165

Fig. 32

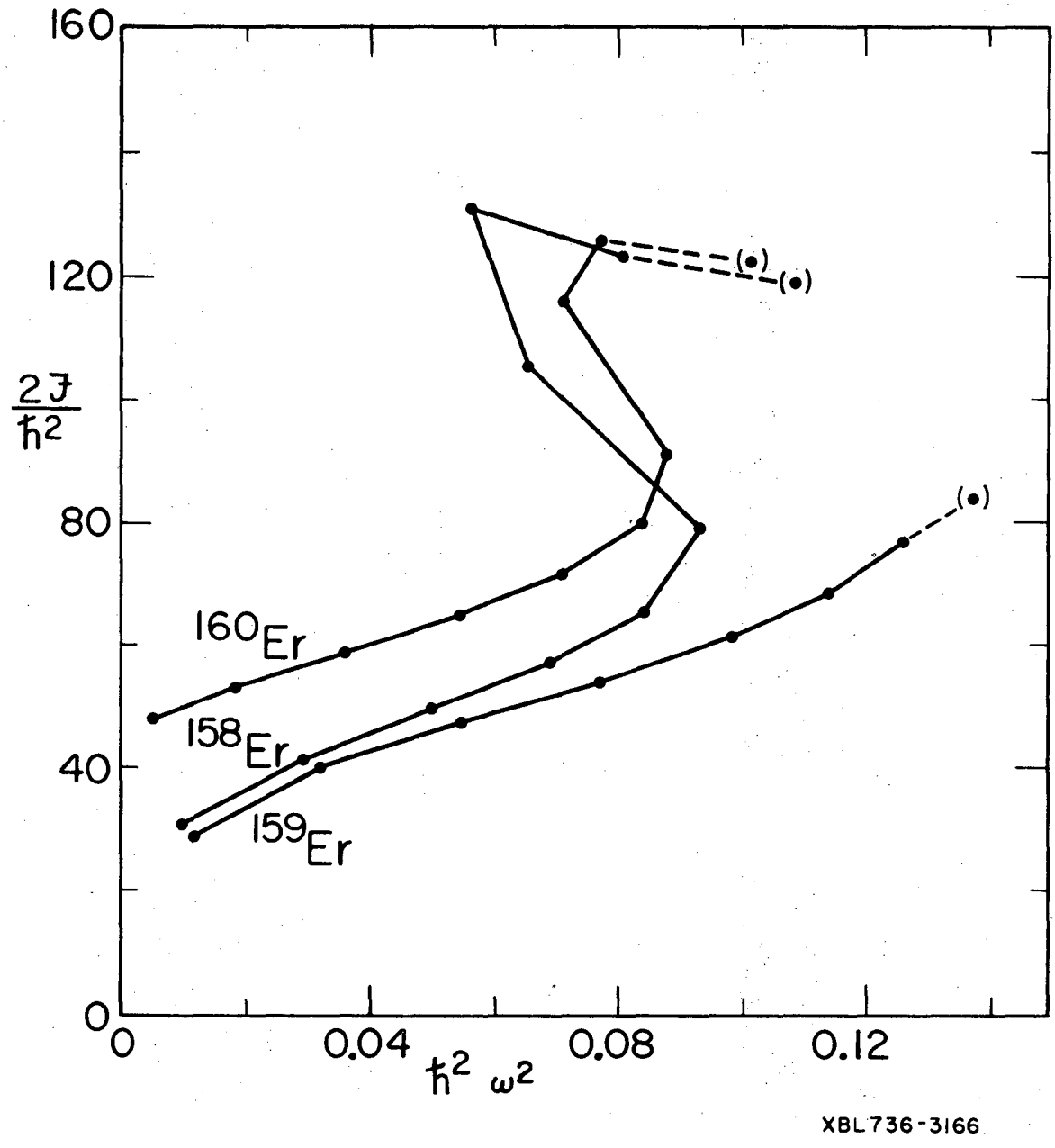
160
120
80
40
0
$\frac{2\mathcal{J}}{\hbar^2}$
0
0.04
0.08
0.12
$\hbar^2\,\omega^2$
^{160}Er
^{158}Er
^{159}Er
(•)
(•)
(•)
XBL736-3166

Fig. 33

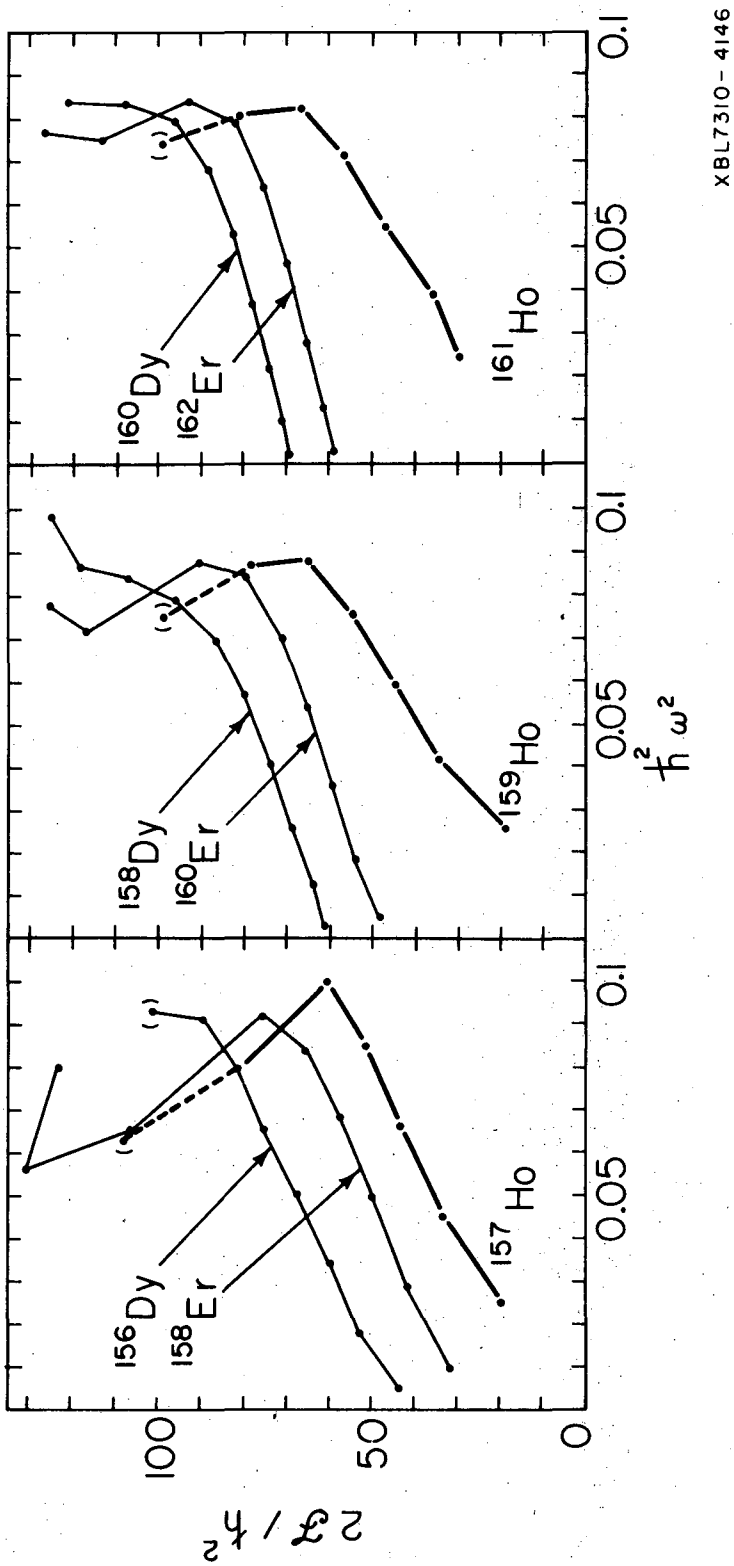

XBL7310-4146

Fig. 34

TECHNICAL INFORMATION DIVISION
LAWRENCE BERKELEY LABORATORY
UNIVERSITY OF CALIFORNIA
BERKELEY, CALIFORNIA 94720